UNIVERSITY OF NAVARRA

SCHOOL OF ENGINEERING

DONOSTIA-SAN SEBASTIÁN

Development of a methodology for the characterisation and modelling of soft tissues for real-time simulation. Application to the modelling of the viscoelastic mechanical response of brain tissue

DISSERTATION
submitted for the
Degree of Doctor of Philosophy
of the University of Navarra by

Ainhitze Mendizabal Dones

under the supervision of

Emilio Sánchez Tapia and
Iker Aguinaga Hoyos

August, 2015

Nire gurasoei,

AGRADECIMIENTOS

Este libro contiene cuatro años maravillosos, con sus frustaciones y alegrías, con su ilusión y desesperanza. Estas páginas no son más que el intento de transmitir todo eso. Este final es el comienzo de nuevos caminos, tanto científicos, como personales. Por ello, me gustaría agradecer a todas esas personas que me han iniciado en estos caminos.

Quisiera agradecer a CEIT y a Tecnun por darme la oportunidad de hacer esta tesis. A Reyes por haber confiado en mí desde el primer día de estos once años y estar segura de que esto era posible. A Emilio por haber planteado esta tesis y haber confiado en mí para ello. Gracias por tus ideas felices y tus ánimos. A Iker por tu apoyo incondicional en estos años. Sin ese apoyo esto no hubiese sido lo que es. Gracias por todas y cada una de las conversaciones. A Diego González, a Nere y a Juanto, por vuestro conocimiento, por desatascarme de vez en cuando en el mundo de elementos finitos y de los materiales hiperelásticos.

Gracias a mis dos angelitos de la guarda, Pablo y Xabi. Si de algo estoy orgullosa es de haber tenido dos compañeros como vosotros durante estos años. Gracias por arroparme durante este tiempo, tanto en lo laboral, como en lo personal. Seguiremos discutiendo sobre si todo fluye, pero puedo decir con total certeza, que esto no hubiese fluido de la misma manera sin vosotros. Asier.. aunque lejos, otro de ellos.

Gracias a los compañeros de robótica, fue una bonita experiencia compartir el laboratorio con vosotros. Javik, en mis comienzos, por todas esas conversaciones, momentos y música. Martín, por tu conocimiento, apoyo y buen humor. Gracias también a Iñigo y Guille.

Gracias a todos y cada uno de los compañeros del departamento de mécanica. Iñaki Díaz, Jorge Juan, Imanol Puy, Manolo, Sergio, Aiert, Hugo, Aitor, Herrera, Fran, Goretti, Alba y al resto de compañeros que he conocido en el CEIT. Eskerrik asko Ibai, izan zaren guztiagatik. Mila esker lau urte hauetan hor egoteagatik, lanean, musikan, zein arlo pertsonalean. Gracias también a los compañeros de multiusos y a la gente de Miramón. A los compañeros de cafés, comidas, y demás, Jon, Juan, Sergio, Amaia, Asier, Borja, Cristina.

Gracias a las nexkas, Itziar, Esther, Ainara, Alaine. ¡Un placer! No me olvido de mis otras nexkas, Lorena, Ane, Ruth, Ana, Larra, con las que aprendí a disfrutar de la vida universitaria.

Gracias a Josune y a Diego, por darme la oportunidad de estar cerca de los alumnos.

Gracias a los trabajadores de Abere, por haberme dado la posibilidad de hacer los experimentos y contribuir en este trabajo.

Eskerrik asko Iñaki. Nondik hasi.. Ezinezkoa da lerro gutxitan zer zaren azaltzea. Eta hare gutxiago, lerro batzutan eskerrak ematea. Ezin azaldu. Sentitzen det, ez dago hitzik zuretzat.

Gracias a mi kuadrila, por interesarse en este trabajo y aguantarme durante este tiempo, Aintzane, Ikuxka, Arzak, Itsaso, Peru, Punki, Maider, Tam, Marin, Naiki. En especial a mis dos angelitos de fuera de la universidad, Txusta eta Miren, mila esker bizi izan ditugun momentu guztiengatik! Eta datozen guztiengatik..

Gracias también a todas esas personas que directa o indirectamente se han interesado por este trabajo y han confiado en él incondicionalmente. A todas esas personas que he conocido en este tiempo, aquellas que me han aportado luz y que han despertado en mí el camino. Y gracias a todos esos amigos que han estado junto a mí durante todos estos años y muchos más.

Mil gracias a mi familia, por su cariño, por animarme y apoyarme durante este tiempo y durante toda mi existencia.

Luz y amor para todos vosotros, y para todos los demás.

Donostia-San Sebastián, Agosto de 2015
Ainhitze Mendizabal Dones

RESUMEN

La caracterización y modelado de las propiedades mecánicas de tejidos biológicos blandos resulta de gran interés para diversas aplicaciones en el ámbito de la bioingeniería, como por ejemplo, para la detección de tumores y enfermedades, así como para tecnologías de asistencia médica y quirúrgica. Entre estas tecnologías está la simulación quirúrgica, que basándose en métodos computacionales, reproduce procedimientos quirúrgicos con el fin de desarrollar las habilidades del cirujano, planificar operaciones o proporcionar técnicas de apoyo al cirujano durante la operación.

Sin embargo, la modelización del comportamiento físico de los órganos y tejidos humanos sigue siendo un desafío. Por una parte, esto es debido a la dificultad para caracterizar las propiedades físicas de los tejidos blandos. Por otro lado, el reto reside en los requerimientos de tiempo de cálculo que se necesita en la simulación, cuando ésta se quiere realizar en tiempo real, siendo el mayor interés el minimizar estos tiempos.

Con el fin de hacer frente a estas dificultades, en esta tesis se ha desarrollado una metodología para la caracterización y el modelado de las propiedades mecánicas de tejidos blandos para su integración en simuladores quirúrgicos. La caracterización se ha llevado a cabo en el laboratorio mediante un reómetro de platos paralelos. La metodología se ha aplicado a materiales sintéticos, como el gel de agar, así como a tejidos biológicos, como

el tejido cerebral porcino. Mediante la realización de esta caracterización, se han analizado y desarrollado diferentes modelos matemáticos para los tejidos elegidos. Se han estudiado estos modelos, con el fin de seleccionar el más adecuado en función de los requerimientos del simulador.

ABSTRACT

The characterisation of the mechanical properties of biological soft tissues is of great interest for many applications in the bioengineering field: such as for the detection of tumours and diseases, for the development of medical assistive and surgical technologies. These technologies include surgery simulation, which based on computational methods, reproduces surgical procedures in order to develop the skills of the surgeon, to plan operations or to provide technical support to surgeon during the operation.

However, modelling the physical behaviour of human organs and tissues remains a challenge. This is due to the difficulty in characterising the physical properties of biological soft tissues. Besides, the challenge lies on the computation time requirements for real-time simulations. Surgical real-time simulation should employ a sufficiently precise and simple model in order to provide a realistic tactile and visual feedback.

To address these difficulties, this thesis presents a methodology for the characterisation and modelling of the mechanical properties of soft tissues, for its integration into real-time surgical simulators. The characterisation is performed in the laboratory using a parallel plate rheometer. The methodology has been applied to synthetic materials such as agar gel, as well as to biological tissues such as porcine brain tissue. By performing this characterisation, different mathematical models have been analysed and

developed for the modelling of the selected tissues. These models have been studied in order to select the most appropriate one, depending on the specific requirements of the simulator.

TABLE OF CONTENTS

LIST OF FIGURES

LIST OF TABLES

LIST OF NOMENCLATURE

Acronyms and Definitions

AS	Amplitude Sweep
CSR	Controlled Shear Rate
FEM	Finite Element Method
FS	Frequency Sweep
LVE	Linear ViscoElastic
MIS	Minimal Invasive Surgery
MRE	Magnetic Resonance Elastography
MRI	Magnetic Resonance Imaging
QLV	Quasi Linear Viscoelasticity
VR	Virtual Reality

List of Symbols

E	Young's modulus
G	Shear modulus
G'	Storage modulus
G''	Loss modulus
J	Volume ratio
ν	Poisson's ratio
$\mathbf{F}$	Deformation gradient tensor
$\mathbf{E}$	Green-Lagrange finite strain tensor
$\mathbf{C}$	Right Cauchy-Green deformation tensor
$\mathbf{B}$	Left Cauchy-Green deformation tensor
$\boldsymbol{\epsilon}$	Infinitesimal strain tensor or Cauchy strain tensor
$\boldsymbol{\sigma}$	Cauchy stress tensor
$\mathbf{P}$	First Piola-Kirchhoff stress tensor
$\mathbf{S}$	Second Piola-Kirchhoff stress tensor

CHAPTER 1

INTRODUCTION

Nowadays, many applications in bioengineering require the characterisation of the mechanical behaviour of biological soft tissues. These applications can be divided into two main groups: applications for the early detection of tumours and diagnosis of diseases; and applications for the modelling of human body, used for example, in automotive industry or in medical and surgical simulation environments.

The characterisation of the mechanical properties of human soft tissues remains important in applications for the detection of tumours and diseases, since these properties vary widely among different physiological and pathological states. Hence, techniques based on the calculation of the mechanical properties of soft tissues have a significant diagnostic potential and they are emerging as a safe, reliable, and non-invasive alternative to other diagnostic procedures, such as biopsy.

Characterisation of biological soft tissues is also essential in the creation of physical and computational human tissue models. Models that represent injuries such as bone fractures or damage in the internal organs are used in automotive industry with the aim of decreasing injury risk in real-life accident situations. Other computational and experimental models of the human torso are developed for ballistic impact testing, where the mechanical behaviour of the internal organs is modelled (Roberts, Merkle, et al., 2007). Soft tissue models can also provide tools for forensics where different head injury mechanisms need to be evaluated (Raul, Deck, et al., 2008).

Human tissue models are especially important in the area of medical simulation, more specifically in the field of surgery simulation. Due to developments in medical systems and robotic technology, surgery has been strongly advanced and improved in the last years. Today, surgery is performed with higher precision, smaller incisions, less pain and reduced healing time. The future is still open for this revolution in surgery and it can be further improved with the introduction of new computer technology. In this context, human tissue models for surgical simulation are a key issue in biomedical research, since it is a powerful technology for the training of surgeons, for surgery planification or even for a general assistance during surgical procedures.

With the aim of improving the actual human tissue models for surgery simulation, this thesis is focused on the characterisation and modelling of the mechanical properties of soft tissues. More specifically, it is focused on the characterisation and modelling of the mechanical behaviour of brain tissue.

1.1 Advanced surgical techniques: minimally invasive surgery

In minimally invasive surgery (MIS), surgeons use a variety of techniques to operate with less injury to the body than in the case of open surgery. These procedures are performed through tiny incisions instead of one large openings (Figure 1.1).

MIS can be carried out by two different approaches: endoscopic (non-robotic) procedure or robotic surgery.

Endoscopic surgery uses scopes going through small incisions or natural body openings in order to diagnose and treat disease. This allows surgeons to view problems within the body without having to make large incisions. Images from the endoscope are projected onto monitors in the operating

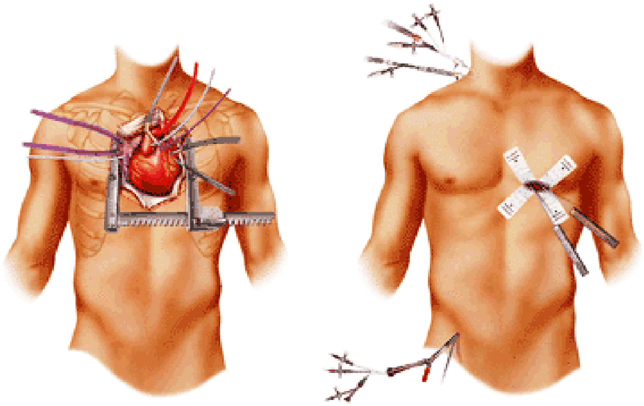

Figure 1.1: Open surgery (left), minimally invasive surgery (right). Picture from Electrical and Computer Engineering Department of the University of Alberta (The Telerobotic and Biorobotic Systems Lab).

room so surgeons can get a clear (and magnified) view of the surgical area (see Figure 1.2). Special instruments are passed through the other openings. These instruments allow the surgeon to perform the surgery by exploring, removing, or repairing the disease.

Figure 1.2: Endoscopic surgery from Weill Cornell Brain and Spine Center.

Accelerated recovery, reduced pain, discomfort and scarring and significantly reduced hospital stays are some of the main advantages of MIS over traditional open surgery. However, the price for these advantages is paid by the surgeon, who has to face several difficulties.

During MIS procedures, surgeons lose direct contact with the operation site, they have to face a significantly degraded haptic feedback about instrument/tissue interactions, degraded visual feedback, and reduced dexterity and fine manipulation capability.

During endoscopic surgical interventions, surgeons have to deal with the trocar effect. They have to work with long instruments through fixed entry points. Due to the presence of these entry points, the so-called trocars, the instruments can be pivoted around the point of trocar insertion. Due to the trocar effect, the motion of the instruments inside the body cavity is just the opposite to the motion performed by the surgeon outside the body. This fact makes the hand-eye coordination unnatural. Moreover, working through trocars introduces a momentum to the surgeon's movements. In addition, in these procedures, surgeons also have to operate in less ergonomic postures.

Robotic surgery or robot-assisted surgery are terms for technological developments that use robotic systems to aid in surgical procedures. This technology was developed to overcome the limitations of MIS and to enhance the capabilities of surgeons performing open surgery. These systems provide surgeons with greater control and vision during surgery, allowing them to perform safe, less invasive, and precise surgical procedures. For example, in the case of robotically-assisted MIS, instead of directly moving the instruments, the surgeon uses one of two methods to control the instruments; either a direct telemanipulator or through computer control.

The best known robotic-assisted surgery system is the *da Vinci* system, in which surgeons operate from a remote console equipped with a master controller that maneuvers four robotic arms. The surgeon is able to watch what the robot is doing inside the patient on a 3D display. This system can also be equipped with two master controllers, as shown in Figure 1.3. In this case, one controller is used by an expert surgeon, while the other is operated by a trainee.

Robotic surgery solves the trocar effect and the non-ergonomic position of the surgeon during endoscopic procedures. Besides, these robotic

Figure 1.3: Da Vinci surgical system with dual console, from Intuitive Surgical.

technologies scale and translate the surgeon's hand movements into precise micro-movements of the robot instruments, improving the precision of MIS. In addition, robotic systems eliminate natural hand tremors of the surgeon, improving dexterity.

However the other drawbacks of MIS, i.e., the loss of direct contact with the operation site, degraded haptic feedback about instrument/tissue interactions and degraded visual feedback remain still a challenge.

In order to address this kind of difficulties presented to the surgeon, surgery simulation is a powerful tool that may assist the surgeon for training on surgical procedures, for the planning of an operation and as a guidance during surgical procedures.

1.2 Surgery simulation

Surgeons need to train using the surgical techniques required in MIS. Due to complex eye hand coordination, restricted field of view and poor tactile sensation of MIS surgery, surgeons have a longer learning curve and require repetitive practice to reach a proficient skill level. Therefore, much time and effort are required for surgeons to become competent in performing MIS. In this way, medical simulators enable novice surgeons to acquire competency in complicated surgical skills that are otherwise risky and difficult to learn through direct surgery on patients.

In addition, medical simulation is also an appropriate technology for the planning of surgical procedures. It can assist surgeons in the planning and rehearsal of a specific surgery procedure before the operation. Hence, the surgeon can perform the surgical procedure in the best possible way, avoiding interfering with critical organs, and thus, reducing risks.

Finally, during this kind of surgical procedures, surgery simulation can provide the surgeon with the deformations of the tissues, adding an extra information to the visual feedback used nowadays.

This work is principally focused on two applications of surgery simulation: training and intraoperative simulation. Next, the three main applications of surgery simulation are explained in more detail.

1.2.1 Surgery simulation for training

Training simulation is a strategy used to teach technical skills, procedures, and operations, by presenting learners with situations that resemble reality. Such tools help improving the clinical skills of surgeons and help reducing deaths, injuries and costs resulting from medical errors and inefficiencies. Currently and during the history of surgery, several training approaches have been used to train surgeons. Next, the different methods are presented:

- **Live animal models**
  Anaesthetised, live animals provide a high fidelity, non-patient environment that allows trainees to develop the psychomotor and cognitive skills required for the operative setting. Animal models have been used extensively in both open and laparoscopic surgical training. Animal models provide realistic haptic feedback, however, the number of animals needed, as well as cultural, financial and ethical issues limit their use.

- **Cadaveric models**
  The use of human cadavers allows surgical trainees to develop a detailed understanding of human anatomy and is a valuable tool for the teaching of whole body anatomy and the interaction between different body parts when affected by disease. In addition to anatomical dissection courses, surgical trainees have used human cadavers to practise many procedures. Preserved human cadavers do not bear the same tissue characteristics as live or recently deceased cadavers, thereby losing some fidelity as a surgical instructional model. In addition to this, considerable expense is involved in the provision of cadaveric specimens, which are single use and not portable. Concerns regarding disease transmission from human tissues and fluids, and ethical and cultural issues limit again this mode of training.

- **Ex-vivo animal tissue models**
  Using anatomic sections or tissues from ex-vivo animals is another form of simulation in surgical skills training. This form of training allows for organs to be prepared and frozen ready for use at a later time. Costs associated with this type of training are relatively low in comparison to live animal training, but still require staff to prepare the organs for simulation, and to supervise and assess trainees.

Since surgeons have traditionally acquired medical skills through the practice on living animals, cadavers, and even patients, such processes inevitably involve animal sacrifices and ethical controversies. Alternatively, medical simulation provides a realistic environment, as in surgical operations, and they allow surgeons to acquire medical skills in safe and ethical conditions. Surgery simulation involves the use of objects, devices, electronic and/or mechanical surgical simulators, to reproduce or represent, under test conditions, situations that are likely to occur in actual performance. These simulators can be classified into three main groups: physical simulator, virtual reality models and hybrid simulator (a combination of both of them).

- **Physical simulator: synthetic models and box trainers**

  Synthetic models and box trainers are simulators in which the learner interacts with solid, real-life materials and uses surgical instruments expected to be used in the operating room. Simulation using physical objects usually involves models of plastic, rubber and latex. These objects are used to render different organs and pathologies and allow a trainee to perform specific tasks and procedures. A box trainer uses the actual instruments and optical system used clinically to manipulate synthetic tissues. Some physical simulators may also reproduce the haptics (tactile sensations) of the actual surgical environment.

  Examples of these simulators are Fundamentals of Laparoscopy (FLS) Box Trainer, Simulab LapTrainer with SimuVision or Simulab Electronic Data Generation for Evaluation (EDGE), see Figure 1.4.

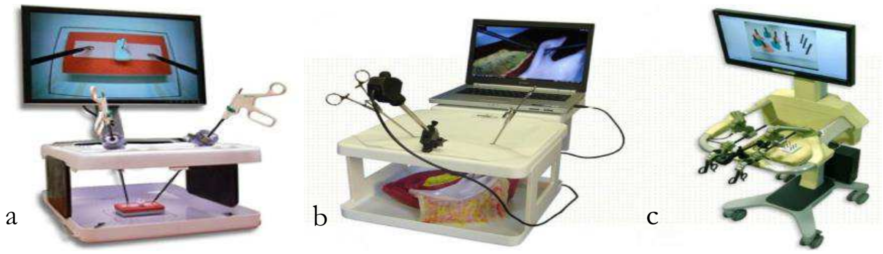

Figure 1.4: (a) FLS Box Trainer by FLS and VTI Medical, (b) Simulab LapTrainer with Simuvision, (c) EDGE by Simulab.

These models have a number of limitations, including limited realism and haptics, and no inherent metrics (performance measurements taken by simulator) for assessment. As a result, some trainees using these types of simulators have found the training unrealistic and boring due to their low fidelity (the extent to which the model imitates reality) (Sturm, 2012). In addition, these physical simulator models do not directly measure movements or skills, and require a trained observer to determine performance. Nonetheless studies show that they are valid and reliable instruments for training specific surgical skills (Sturm, 2012). Their relatively low acquisition cost, high availability and easy portability, make this type of simulator the most widely available and most validated surgical training system.

- **Virtual Reality (computer-based) models**

  Virtual Reality (VR) based surgical simulators are the most technologically sophisticated class of simulator currently available, and they are receiving widespread attention (Sturm, 2012). VR systems use computer generated instruments through specially designed interfaces to manipulate computer generated objects. An attractive feature of these surgical simulators is that they can provide objective and repeated measurements, such as the time taken to complete a task, the errors made in the process and also the efficiency with which the movements were made in order to accomplish the task. These metrics present the opportunity for the assessment of competency without the need for an observer to be present.

  As robotic VR-based simulators, some examples are Mimic dV-Trainer, Da Vinci Skill Simulator and RoSS Robotic Surgery Simulator, see Figure 1.5.

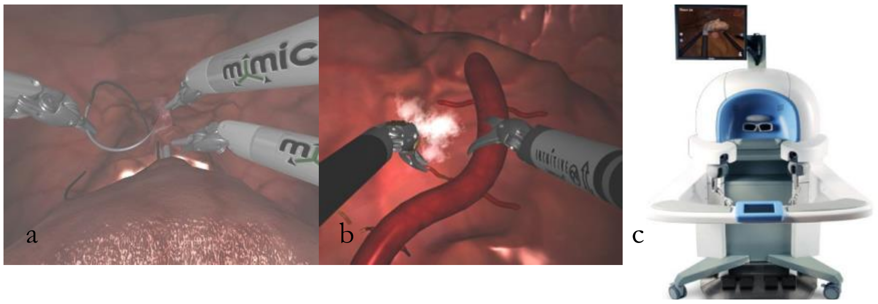

Figure 1.5: (a) MIMIC dV-Trainer (b) da Vinci Skills Simulator and (c) RoSS robotic surgery simulator.

Endoscopic VR-based simulation are widely developed: VirtaMed

HystSim/TURPSim and GI Mentor II as examples, see Figure 1.6. Laparoscopic VR-based simulators are also very common, some examples are SEP-SimSurgery Education Platform, Surgsim-METI, LapSim, LapMentor and CAE Laparoscopy VR Surgery Simulator, see Figure 1.7.

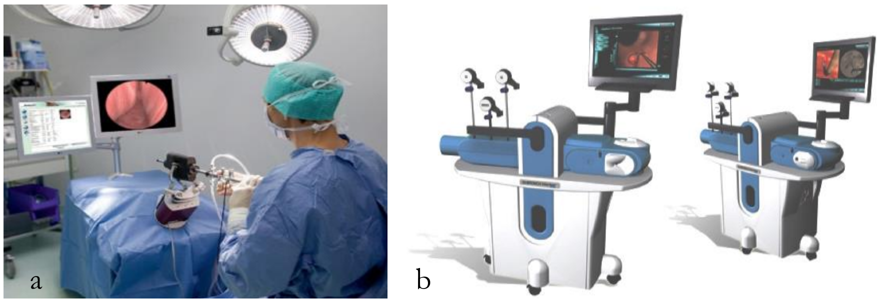

Figure 1.6: (a) TURPSim by Simbionix and (b) GI Mentor by Simbionix.

Figure 1.7: (a) Simbionix LapMentor and (b) CAE LaparoscopyVR surgery simulator.

However, realistic tactile sensations in the use of surgical instruments is still imperfect in some VR simulators.

- **Hybrid simulators**
  Hybrid simulators are a combination of physical and VR simulators. They consist of a physical object (frequently a mannequin) being linked to a sophisticated computer program that provides visual images and/or feedback. The computer program can simulate patient responses, both physically on the mannequin and physiologically in

response to a procedure. These simulators go beyond basic skills training and are designed to recreate specific anatomy and physiology. They allow trainees to practise all the skills necessary to perform a particular operation. Hybrid simulators are expensive and are limited in use due to the high demands of time and effort required to prepare and run them.

1.2.2 Surgery simulation for planning

Surgery simulation can also be used for treatment planning, with the aim of better accomplishing the operation. Surgical planning gives the ability to rehearse the various steps of the operation, helping the surgeon to avoid interfering with critical organs, and thus reducing operating time and risks. While training is focused on non-expert surgeon, the planning sesion is related to a specific and real surgery for an expert surgeon. The main difference between virtual models designed for planning and training purposes is that the objective of the first one is to be as accurate and realistic as possible while the second one has to be appropriate to transfer certain skills. Using a simulator for planning a real case of surgery requires specific data pertaining to the patient (San Vicente, 2011).

1.2.3 Surgery simulation for surgery assistance

Intraoperative surgery simulation aims reproducing the visual and haptic senses experienced by a surgeon during a surgical procedure, through the use of computer systems. Surgery simulation is included as a means of guidance, diagnosis, verification and general assistance during the performance of a MIS intervention. Up to this day, it is based on image-guided surgery.

Image-guided surgery or intraoperative navigation is the general term used for any surgical procedure where the surgeon employs tracked surgical instruments in conjunction with preoperative or intraoperative images in order to indirectly guide the procedure. This images are obtained by devices such as computed tomography (CT) scanners or magnetic resonance imaging (MRI) scanners.

The intraoperative navigation systems show virtual images by superimposing models of target tissues on real endoscopic images. These systems then allow the surgeon to see the location of the animated surgical tool on the monitor with respect to the visually displayed anatomical images during the operation. In that way, the surgeon gets better orientation, leading to higher precision and safety.

However, conventional navigation systems do not consider the tissue deformation during surgery. Since soft tissues within the body are deformed during the surgery, these systems need to provide surgeons reliable information by deforming the models according to their biomechanical behaviour. Thus, computational models of the human body could be used in conjunction with medical imaging and computer based techniques to assist in the preparation, simulation and control of medical interventions.

Thus, surgery simulation during surgical procedures can provide surgeons with information about the deformation which is suffering the soft tissue. In that way, the surgeon can establish a deformation range and have some warning if this deformation range is exceeded, in order to avoid mechanical or functional damage in soft tissues.

Surgery simulation can also serves as surgical planning during surgical procedures. If real-time information of the patient is available during the operation, the surgeon can stop the operation and turn to the planning tool, in order to plan the next steps of the surgery in the best way possible.

1.3 Main components of VR surgery simulator

This thesis is focused on the improvement of VR simulators. In order to build a VR surgery simulator, several components have to be integrated. A surgery simulator can be ilustrated by four key modules, as it is shown in Figure 1.8. These modules may be found especially in training simulators. Currently, planning and intraoperative simulators do not integrate all of these features, but they share many of these components.

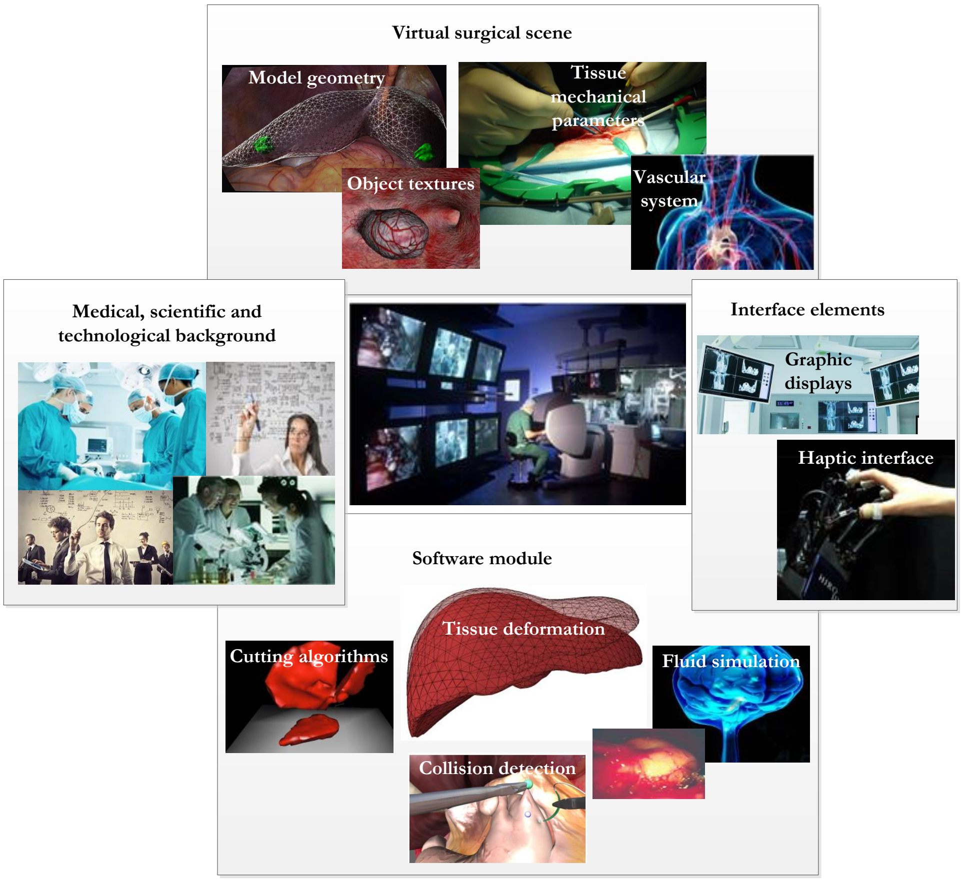

Figure 1.8: Key modules of a surgery simulator.

- **Medical, scientific and technological background**
  The medical background defines the problem area, identifies the simulation needs, and influences the system development at all stages. The medical requirements should be carried out with other scientific and technological disciplines, in order to define the problem and the requirements not only from a medical point of view, but also from an engineering point of view.

- **Virtual surgical scene**

  This module focuses on the generation of virtual surgical scenes. This includes models of healthy and pathological anatomy, tissue deformation models and parameters as well as organ textures or vessel structures.

  Model geometry. The first step in a virtual surgical scenario definition process is the generation of the geometrical representation of the scene objects. It mainly denotes the human organs and possibly their pathological changes.

  Tissue mechanical parameters. In order to model the biomechanical behaviour of soft tissues in a virtual surgical scene, appropriate parameters have to be determined for the deformation algorithms. Modelling a tissue does not always involve a previous material characterisation. Therefore, the tissue models are not always realistic enough. The most realistic models are physically-based, and this implies a mechanical characterisation of the tissue. For determining the mechanical parameters of a tissue, many considerations have to be taken into account. In-vivo or in-vitro characterisation or testing device are some of them, since they influence the tissue mechanical characteristics.

  Object textures. Another component in the scenario definition is the object surface appearance. Providing correct visual information can improve the surgery simulation.

  Vascular system. A further key element in a scene definition scheme is the generation and integration of vascular structures. Blood vessels affect surgery simulation on several levels. Firstly, they are the carriers of blood circulation and thus an integral part of a patient physiological model. Moreover, they affect the visual appearance of organ surfaces and thus have to be included into the texturing process. In addition, they have to be part of the geometrical model since they deform with the tissue and are the source of bleeding after cutting.

Other phenomenons such as metabolism or tractography can also be modelled in this module.

- **Interface elements**
  This module denotes the interface elements that are the media to exchange information through different sensori-motor human channels.

  Graphic displays. This refers to screen where the virtual scene is rendered. This is the main interface used in all VR simulators.

  Haptic interface. The haptic device is the human-machine interface between the user and the simulator. It renders tactile feedback to the user based on the interaction with the virtual world. Moreover, it provides a natural means for controlling the simulation. In the optimal case, real surgical tools are adapted and equipped with sensors to serve as input devices, while interaction via mouse or keyboard should be avoided.

  Other interface elements, such as, speakers can also be used in order to exchange auditory information with the user.

- **Software module**
  The software modules are combined into the virtual representation of the surgery.

  Tissue deformation. Deformable tissue modelling is a key component in any surgical simulator. Efficient and robust methods are required in order to provide the mechanical behaviour of soft tissue at interactive speed. Besides, a tissue deformation model requires the generation of meshes for all deformable objects and an appropriate mechanical tissue parameterisation and modelling as described above.

  Fluid simulation. Several surgical procedures require the modelling of fluids. For instance, in hysteroscopy the uterus is distended with liquid media to access and visualize the uterine cavity. Another example is the cerebrospinal fluid founded in the brain and spine. It acts as a cushion or buffer for the brain's cortex, providing basic mechanical and immunological protection to the brain inside the skull. Therefore, the modelling of fluid motion is required in some surgical procedures. In addition, due to several diseases, or during cutting or strong collisions with organs, vessels can be damaged, which causes bleeding depending on the size of the vessel. Thus, a bleeding model is required to simulate different effects, e.g. oozing or fast spurts.

Collision detection. In order to process the interaction between soft and rigid objects in a simulator, efficient collision detection algorithms are required. In addition, an appropriate response to the collisions needs to be determined. A geometrical representation of all scene objects has to be provided to this end, which is usually done during the scene generation step.

Interactive tissue cutting. Simulation of soft tissue cutting is an integral part of surgery simulation. Smooth cuts into the organ models have to be created, while preserving the numerical stability of the underlying deformation computation.

1.4 Requirements of surgery simulation

Models used in surgery simulation have to be as realistic as possible in order to provide an accurate result to users. Therefore, these simulations require an accurate organ geometry and realistic mechanical properties of soft tissues. However, they also require fast computation algorithms in order to provide a correct visual and tactile feedback. That is why all the modules and features included in surgical training or intraoperative simulators must meet the requirements described below. The compliance of these requirements is what makes difficult the implementation of some of these modules in surgery simulation.

Accuracy

Accuracy is one of the most important requirements to take into account in these kind of simulations. Ideally, surgery simulation requires an accurate representation of the behaviour of the whole region of interest of a surgery, under different loading conditions. Geometric and physical models of anatomical structures must be defined. In contrast to deformable models used in video games and animation, the purpose of such models in medical simulation is to model the realistic behaviour of biological tissues. Therefore, the geometry can be obtained from various medical image modalities, while the deformation should be controlled by real material parameters taken from biomechanics experiments instead of intuitively adjusted parameters. However, one of the largest drawbacks in the advance of this technology is the lack of understanding of the mechanical response of soft tissues to surgical manipulations (Kerdok, 2006).

In addition to the accuracy, believability remains important. With this aim, not always is necessary to reach extremely high levels of accuracy. Sometimes, simulation may not be accurate, but it must be credible, ie, the user experience must be good enough, to extrapolate the conclusions of usage of the simulator to the reality.

Execution time

Execution time of the simulations is another important requirement. Although it is not critical in all surgery simulators, in most of them a fast execution time is indispensable, in order to obtain a real-time simulation.

For planning simulators, the execution time can be longer than in other kind of simulations, and real-time is not necessary. However, for training simulators and intraoperative simulations, computation must be fast enough to sustain real-time interactions, in order to give an adequate feedback to the surgeon.

In the framework of surgery simulation, real-time means that visual and haptic feedback can be reproduced at a correct frequency. To support the user with visual feedback, a deformable model has to be updated at about 20 Hz, and to provide a proper haptic feedback at 1 kHz. The fact that the model needs to be fast enough to provide these visual and haptic results, eliminates most of the standard methods developed in computational physics, which are too slow to be used in real-time applications (Zhu and Gu, 2012).

Robustness

The model needs to be robust to provide results under large deformations and with large time-steps. Besides, the model should be easy to integrate into a complex surgery simulator. In a typical virtual surgical environment, objects with different material properties, phases, geometry shapes and data representations are often combined together, and different types of interactions and responses between them need to be handled together (Zhu and Gu, 2012).

Summarizing, a good balance between surgical realism and interactive rates of simulation is one of the most challenging problems in surgery simulation (Delingette, Cotin, et al., 2004). To develop a model for real-time deformation, it is important to make a series of decisions, such as a geometric description of the object, a mathematical model of the tissue deformation and a solution algorithm which together allow the solution to be determined quickly and reasonably accurate.

1.5 Motivation

The main objective of this dissertation is the research in the characterisation and modelling of the mechanical behaviour of soft tissues for surgery simulation, more specifically for training and intraoperative simulators.

Although there are several commercial medical training simulators, there is still much room for improvement in this technology. Some VR surgery training simulators do not produce a realistic tactile feedback. Furthermore, intraoperative surgery simulation provides surgeons with image-guided navigation, but biomechanical model of soft tissues is not considered, and therefore surgeons do not have a feedback about the deformation to which the tissue is subjected.

As it has been mentioned before, tissue parameters and tissue modelling play an important role in the development of more realistic surgical simulators. Although high fidelity organ geometry and fast computation algorithms to simulate tissue deformation have been studied, the characterisation of mechanical properties has not yet been sufficiently studied due to the difficulties in testing and modelling the complexities of time dependency and non-linearity of soft tissues.

For that reason, this thesis aims to develop a methodology to characterise and model the mechanical behaviour of soft tissues, giving the appropriate steps from the experiments in the laboratory until the development of a suitable deformation model.

1.6 Objectives of the thesis

The main objective of this thesis is the development of a methodology for the characterisation and modelling of soft tissues for real-time simulation.

- **Objective 1:** Development of a methodology for the characterisation of the mechanical properties of biological soft tissues for the application of surgery simulation.
    - **Hypothesis 1.1:** The characterisation of the tissue will be carried out with a parallel-plate rheometer, that implies that the tissue will be characterised under simple shear loads. Even though the characterisation of the tissue under other loads, such as compression, tension or indentation, can be of interest for surgery simulation, it is not considered in this work.

  - **Hypothesis 1.2:** The characterisation in a rheometer implied a characterisation of ex-vivo samples. Despite the fact that differences may exist between in-vivo and ex-vivo characterisation, they are not considered in this thesis.
  - **Hypothesis 1.3:** To establish this methodology using sinthetic materials. Since, they are more homogeneous, they have less variability and they are more accessible. Agar gel is selected since it seems to have similar mechanical behaviour to that of biological soft tissues.
  - **Hypothesis 1.4:** To apply the methodology to biological soft tissue. Although the methodology for characterisation is valid for soft tissues in general, it is applied to brain tissue. Due to availability difficulties of human brain tissue, porcine brain tissue is chosen as a surrogate for it. Although porcine brain tissue seem to be an adequate substitute for this purpose, the differences that may exist between porcine and human soft tissues are not considered in this thesis.

- **Objective 2:** Once the soft tissue is experimentally characterised, the second main objective of this thesis is the modelling of the tissue by mathematical models. The choice of a biomechanical model must take, as we have seen, two contradictory elements into account: simulation realism and computation cost for implementing the model. In many previous works, the living tissues have been modelled using models that do not provide accurate results, in order to achieve a suitable computational cost. In this research work, a more realistic and complex behaviour is sought. That is, the proposed model has to be able to describe non-linear and viscoelastic behaviour of soft tissues.

  - **Hypothesis 2.1:** This thesis is focused on two of surgery simulator modules: tissue mechanical parameters and tissue deformation. Other modules that may be of interest for surgery simulation, such as tissue cutting algorithms or fluid simulations are not studied in this thesis.

  - **Hypothesis 2.2:** The mathematical models developed are simulated in a commercial software, in order to validate these models compared to the obtained experimental data. To this end, Abaqus software is chosen, which is considered an accurate and widely recognized finite element analysis software.

  The objectives related to the modelling of biological soft tissues for surgery simulation are the following:

  - **Objective 2.1:** To study different mathematical models for the modelling of soft tissues. These models have to take into account the non-linear and viscoelastic behaviour of soft tissues and they have to be simple enough for their implementation in real-time surgical simulators.
  - **Objective 2.2:** To model the agar gel with the results obtained experimentally.
  - **Objective 2.3:** To model the porcine brain tissue with different mathematical models, taking into account the characteristics of soft tissues such as non-linearity and viscoelasticity.
  - **Objective 2.4:** To establish a set of criteria in order to select the most suitable mathematical model.

- **Objective 3:** The characterisation and the modelling of soft tissues aims to be a part of surgical simulation system. With this purpose, the last main objective of this thesis is to integrate the developed soft tissue models in a real-time platform.

  - **Hypothesis 3.1:** The developed mathematical models are implemented with non-linear Total Lagrangian finite element formulation using a tetrahedral mesh. This method is considered an adequate solution for the modelling of deformable objects in real-time applications.

- **Objective 3.1:** The presented models need to be introduced in real-time platform in order to study their execution times and their applicability for real-time simulators.

1.7 Contents and structure of the thesis

This thesis is divided into six chapters.

Chapter 1 has presented the importance of the characterisation of biological soft tissues for the field of medicine and the fields where it is necessary to continue characterising them. Since this thesis is particularly focused on surgical simulation, requirements of surgical simulation have been described in this chapter. In addition, the factors that have motivated this work and the main objectives to be achieved have also been presented.

Chapter 2 presents the basic concepts to understand the characterisation of deformable materials and the mathematical modelling necessary to develop a surgical simulator.

Chapter 3 is focused on the characterisation of soft tissues. In this chapter different tests to characterise soft tissues are presented. Characterisation of agar gels and porcine brain tissue is studied.

Chapter 4 presents the modelling of soft tissues. The agar gel and porcine brain tissue previously characterised are modelled with different mathematical models. A study of these models is presented.

Chapter 5 presents the basis for the development of a robot-assisted surgical system. The basis to integrate the developed tissue models in intraoperative surgical system are presented in this chapter.

Finally, conclusions and future works are enumerated in Chapter 6.

Chapter 2

INTRODUCTION TO MODELLING OF SOFT TISSUES

Several steps have to be carried out to simulate a real deformable tissue, as it is illustrated in Figure 2.1. Firstly, it is essential to know the physical behaviour of the tissue. The mechanical behaviour of the material is obtained by experimental tests that give as a result curves of its deformation. These results must be transformed into a mathematical model that includes the constitutive equations of the material. The mathematical model must be introduced into a computational method. This method assembles the geometry and the physical behaviour of the material and it is vital for the simulation of different virtual conditions. This computational method will be the basis for the surgery simulation system.

This chapter aims to introduce the basis of these three steps: characterisation of mechanical properties, mathematical modelling and computational method. In order to get into the physical behaviour of the material, Section 2.1 shows a material classification according to their mechanical properties. There, the physical properties of soft tissues such as elasticity, viscosity and viscoelasticity are presented. It is essential to transform the mechanical behaviour into constitutive equations, in other words, into mathematical models that describe the physical behaviour. The mathematical model will be a part of a computational model. Section 2.2

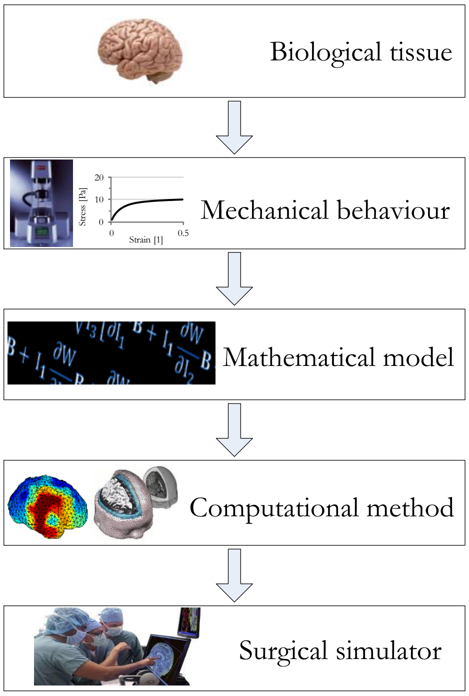

Figure 2.1: Steps for modelling of mechanical behaviour of materials: physical characterisation of mechanical behaviour, mathematical model and computational simulation.

presents the basis of continuum mechanics in order to establish the mathematical nomenclature necessary to develop the constitutive equations of the materials. Section 2.3 introduces the most commonly used simulation methods for simulation of soft tissues. With the aim of selecting a simulation method with physical meaning, Finite Element Method (FEM) is chosen in this thesis. Finally, section 2.3.3 presents the FEM formulation that makes possible a simulation in a real-time: the Total Lagrangian Method.

2.1 Mechanical behaviour of biological soft tissue

This chapter provides some background of the modelling of biological soft tissues. For this purpose, it is necessary to know the mechanical behaviour of soft tissues and the existing methods to model it. This section introduces the mechanical properties of biological materials. Elasticity, viscosity and viscoelasticity concepts are presented. The reader who is familiar with these concepts should feel free to skip this section.

Soft tissues and materials in general can be classified in many different ways depending on their physical properties. This thesis is focused on the study of the mechanical properties of the materials, leaving aside other kind of physical properties. As stated by Fung (1981), a wide variety of materials exist. Thus, we are not surprised that there is a vast number of constitutive equations describing an almost infinite variety of materials. What should be surprising is the fact that three simple, idealized stress-strain relationships (the nonviscous fluid, the Newtonian viscous fluid and the Hookean elastic solid) give good description of the mechanical properties of many materials around us. Within certain limits of strain and strain rate, air, water, and many engineering structural materials can be described by these idealized equations.

Other materials, however, cannot be described so simply, since they share characteristics of fluids and solids. They are actually viscoelastic materials. This is the case of biological soft tissues, since they present both viscous and elastic characteristics when undergoing deformation. Viscous materials resist shear flow and strain linearly with time when stress is applied. Elastic materials strain instantaneously when stretched and just as quickly return to their original state once the stress is removed. However, viscoelastic materials have elements of both of these properties and, as such, they exhibit time dependent strain. In other words, the particular response of a sample in a given experiment depends on the time-scale of the experiment in relation to a natural time of material. Due to the viscosity induced strain-rate effect, the response at the equilibrium state differs from that at the instantaneous state. Thus, if the experiment is relatively slow, the sample will appear to be viscous rather than elastic, whereas, if the experiment is relatively fast, it will appear to be elastic rather than viscous (Barnes, Hutton, et al., 1989). Materials can be classified as presented in Figure 2.2. Regarding the viscosity, fluids can be Newtonian or Non-Newtonian. Non-Newtonian fluids can be classified regarding the load, as pseudoplastic or dilatant, or regarding the application time as thixotropic o rheopectic. Similarly, regarding the elasticity, materials can be classified as Hookean, when they are linear elastic or Non-Hokeean when the elasticity is non-linear. Viscoelastic materials meanwhile, share characteristics of elasticity and viscosity. Below, this classification is explained more deeply.

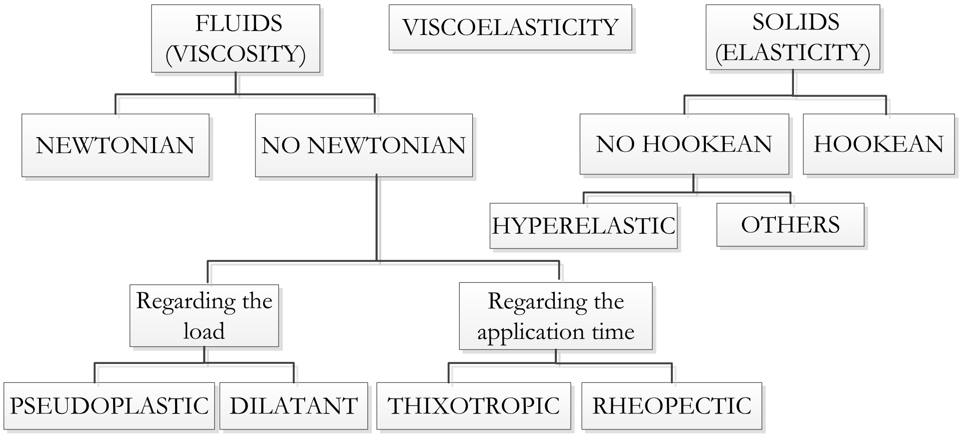

Figure 2.2: Classification of materials.

2.1.1 Elasticity

The main mechanical property for solids is elasticity. When an elastic material is deformed due to an external force, it experiences internal forces that oppose the deformation and restore it to its original state if the external force is no longer applied. This effect is called elasticity.

Elastic modulus is a measure of the resistance of an object or substance to being deformed elastically (i.e., non-permanently) when a force is applied to it. Generally, the elastic modulus of an object is defined as the slope of its stress-strain curve in the elastic deformation region. Depending on the type of loading (shown in Figure 2.3), different elastic modulus are defined.

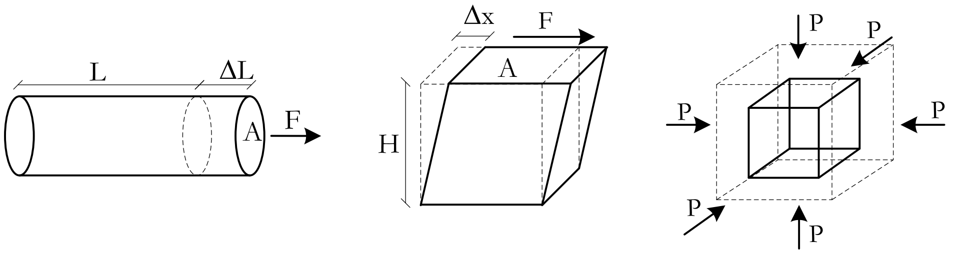

Figure 2.3: Longitudinal deformation (left), simple shear deformation (middle) and uniform compression (right).

- Young's modulus, E, describes the elastic properties of a solid undergoing uniaxial tension or compression (Figure 2.3 (Left)). It is defined as stress, σ, divided by strain, ε, as Equation (2.1).

$$E = \frac{\sigma}{\varepsilon} \tag{2.1}$$

  where tensile stress is the normal force per area $\sigma = F/A$ and tensile strain is the fractional increase in length, $\varepsilon = \Delta L/L$.

- Shear modulus, G, is a measure of the ability of a material to resist tangential or transverse deformations (Figure 2.3 (Middle)). It is associated with the change in shape of the material under the action of shear forces. It does not involve volume changes. Elasticity in shear is defined as the ratio of shear stress, τ and the corresponding shear strain, γ (Equation (2.2)).

$$G = \frac{\tau}{\gamma} \tag{2.2}$$

  being shear stress the tangential force per area $\tau = F/A$ and shear strain $\gamma = \Delta x/H$.

- Bulk modulus, K, measures the substance's resistance to uniform compression (Figure 2.3 (Right)). It is associated with volume changes experienced by a material under the action of forces acting perpendicularly to its surfaces. It does not involve change in the shape, just in the volume. The bulk modulus is defined by Equation (2.3).

$$K = -V \frac{\Delta p}{\Delta V} \tag{2.3}$$

where p is the pressure, V is the volume and Δp and ΔV are pressure and volume changes respectively.

Homogeneous isotropic linear elastic materials have their elastic properties uniquely determined by any two moduli among these; thus, given any two of them, any other of the elastic moduli can be calculated through Poisson's ratio, ν, by Equations (2.4) and (2.5). Poisson's ratio can be defined as the fraction of expansion divided by the fraction of compression, for small values of these changes. When a material is compressed in one direction, it usually tends to expand in the other two directions perpendicular to the direction of compression. This is called the Poisson's effect.

$$E = 2G(1 + \nu) \tag{2.4}$$

$$K = \frac{2G(1 + \nu)}{3(1 - 2\nu)} \tag{2.5}$$

The stress-strain relationship of materials can be differentiated into linear elastic materials (Hookean elastic solids) or non-linear elastic solids. A Hookean elastic solid is an ideal solid that obeys Hooke's law, which states that the stress tensor is linearly proportional to the strain tensor. For most materials and for small deformations, the stress-strain relationship can be adequately described by Hooke's law. However, for larger stresses beyond the elastic limit, the relation is no longer linear. In non-linear elastic solids, stress-strain relationship is not linear. For non-linear elastic solids, the most common model is hyperelasticity. A hyperelastic material is a special case of a Cauchy elastic material: it is a type of constitutive model for ideally elastic material for which the stress-strain relationship derives from a strain energy density function. Figure 2.4 shows stress-strain curve for linear and non-linear elastic materials.

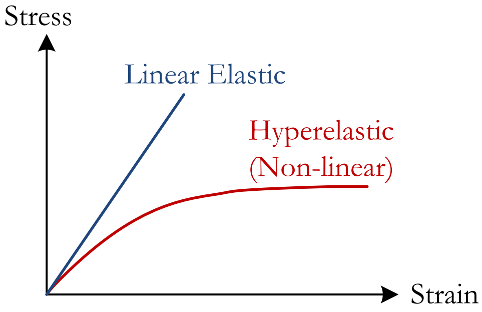

Figure 2.4: Elasticity curves of linear and non-linear elastic materials.

2.1.2 Viscosity

As elasticity for solids, the main property for fluids is viscosity. Viscosity is a measure of the resistance of a fluid which is being deformed. Viscosity describes a fluid's internal resistance to flow and may be thought of as a measure of fluid friction.

Viscosity of materials can be affected by variables such as the nature of substance, temperature, pressure, strain rate, shear time or even the presence of electric or magnetic fields. The most important variable, from a rheological point of view is the shear rate. Curves of elasticity (Figure 2.4) and viscosity (Figures 2.5 and 2.6) establish the viscoelastic behaviour of the material.

Shear viscosity is defined as the ratio of the shear stress and the corresponding shear rate (Equation (2.6)).

$$\eta = \tau / \dot{\gamma} \tag{2.6}$$

where η is the shear viscosity, τ is the shear stress and $\dot{\gamma}$ is the shear rate.

If viscosity remains constant, the fluid is called a newtonian viscous fluid (or ideal viscous fluid). In that case, the shear stress is linearly proportional to the strain rate and independent of strain. Viscosity remains constant during shear, and stress falls to cero instantaneously when shear stops. Viscosities measured on different strain conditions are proportional (for example, viscosity measured in extensional fluid is always three times the viscosity measured in shear). Newton's law of viscosity is a constitutive equation. It is not a fundamental law of nature but an approximation that holds in some materials and fails in others. Most materials are non-newtonian. These fluids exhibit a more complicated relationship between shear stress and velocity gradient than simple linearity. Viscosity is not a factor, but a function of shear strain.

Non-newtonian fluids can be classified with regards to the shape of their viscosity curve. Viscosity over the applied load can be classified as pseudoplastic (or shear thinning) when viscosity decreases and dilatant (or shear thickening) when the shear viscosity increases with applied shear stress. While, if viscosity is analyzed regarding to the time of the application, it should be classified as thixotropic when material becomes less viscous and rheopectic when the fluid becomes more viscous over time when shaken, agitated, or otherwise stressed. Figures 2.5 and 2.6 show the behaviour of these materials.

At the same time, fluids can show different viscosity functions. Figure 2.7 shows the viscosity function of a material with yield point (1) and viscosity of the material without yield point (2).

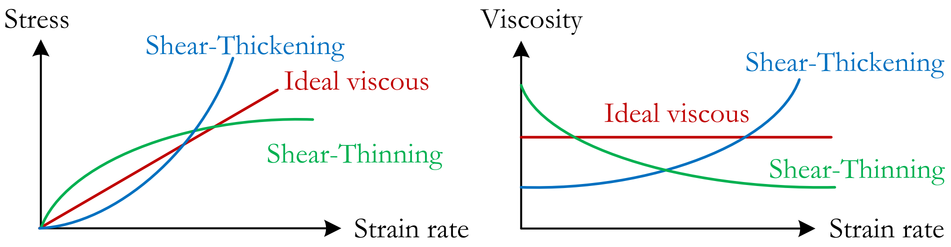

Figure 2.5: Viscous materials representation regarding time independence.

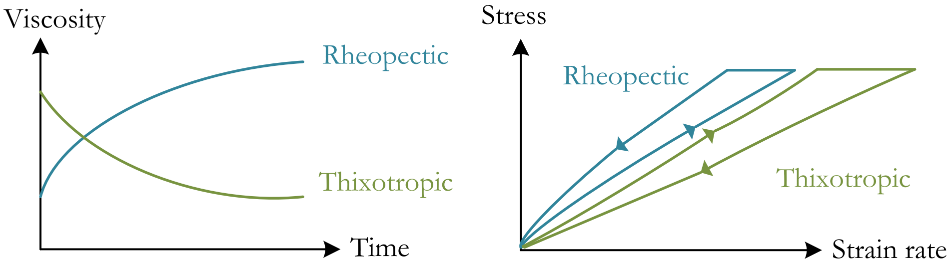

Figure 2.6: Viscous materials representation regarding time dependence.

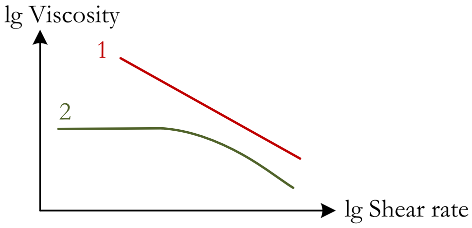

Figure 2.7: Comparison of two viscosity functions: (1) without showing a zero-shear viscosity (and therefore, showing a yield point) (2) showing a zero-shear viscosity plateau value (and therefore, no yield point).

2.1.3 Viscoelasticity

As mentioned above, viscoelastic materials not only have elastic properties, but also have viscous characteristics. It can be illustrated with the dynamic modulus of the viscoelastic materials. Dynamic modulus is the ratio of stress to strain under vibratory conditions (calculated from data obtained from either free or forced vibration tests, in shear, compression, or elongation).

As an example, instead of defining the shear modulus, G, as it would be for a purely elastic material, it is defined as the complex viscoelastic modulus, G^*. This is defined as the ratio between shear stress and shear strain amplitudes, as $G^* = \tau(t)/\gamma(t)$. It is a complex modulus composed by the storage and loss modulus. The storage modulus, G', is a measure of the deformation energy stored by the sample during the shear process and represents the elastic behaviour of the material. The loss modulus, G'', is a measure of the deformation energy used up by the sample during the shear process and represents the viscous behaviour of the material. Figure 2.8 shows both complex shear modulus and complex viscosity representations. The elastic portion can be specified as both G' or η”, and the viscous portion as both G'' or η’.

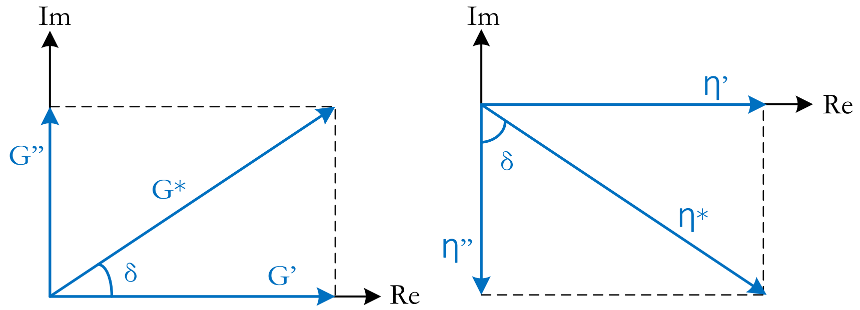

Figure 2.8: Vector diagram showing the resulting complex shear modulus (left) and the resulting complex viscosity (right).

Loss factor or damping factor, tanδ, reveals the ratio of the viscous and the elastic portion of the viscoelastic deformation behaviour, as $tan\delta = G''/G'$. Therefore, material behaviour is classified as:

Viscoelastic behaviour:	$0 < tan\delta < \infty$	or	$0° < \delta < 90°$
Ideal elastic behaviour:	$tan\delta = 0$	or	$\delta = 0°$ $(G'' = 0)$
Ideal viscous behaviour:	$tan\delta = \infty$	or	$\delta = 90°$ $(G' = 0)$

Also, it can be established that:

Liquid state:	$tan\delta > 1$	since	$G'' > G'$
Gel, solid state:	$tan\delta < 1$	since	$G' > G''$
Gel point:	$tan\delta = 1$	since	$G'' = G'$

As it is shown in Figure 2.9, the values of the mechanical properties of a material, such as G' and G'', can change when it is subjected to external forces. The range where G' and G'' remain steady is called Linear Viscoelastic

(LVE) range. In that circunstances, the material shows reversible-viscoelastic behaviour, it will deform elastically and will return to its original shape when the applied stress is removed. The structure of the sample shows stability, and no significant change of the internal structure occurs. The limiting value of the LVE range is the yield point, τ_y.

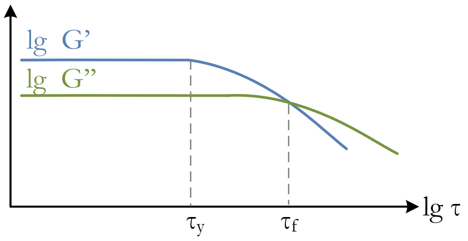

Figure 2.9: Representation of storage and loss modulus, showing yield point and flow point.

The yield point of a material is defined in engineering and materials science as the stress at which a material begins to deform plastically. Yield point is read at the limiting value of the shear stress where the behaviour changes from elastic to viscous. When the yield point is exceeded, some fraction of the deformation will be permanent and non-reversible, and the material starts to flow, showing a viscous behaviour. The material still shows gel character ($G' > G''$), but the reversible-elastic deformation range is already exceeded, and now, irreversible elastic behaviour is presented. If the shear process was stopped in this range, only partial reformation would occur, resulting in lower values of G' and G'' if compared to the initial values of the LVE range. The flow point, τ_f, is the stress corresponding at the crossover point ($G' = G''$), where the gel character ($G' > G''$) changes to a liquid character ($G'' > G'$).

Hysteresis, relaxation and creep are the main features of viscoelasticity (Fung, 1981). When a body is suddenly strained and the strain is maintained constant afterwards, the corresponding stress induced in the body decreases with time. This phenomena is called *stress relaxation.* If the body is suddenly stressed and the stress is maintained constant afterwards, the body continues to deform, this phenomenon is called *creep*. If the body is subjected to a cyclic loading, the stress-strain relationship in the loading process is usually somewhat different from that in the unloading process, this phenomenon is called *hysteresis*.

Stress relaxation

Stress relaxation describes how materials relieve stress under constant strain. Figure 2.10 shows the stress relaxation behaviour for different materials.

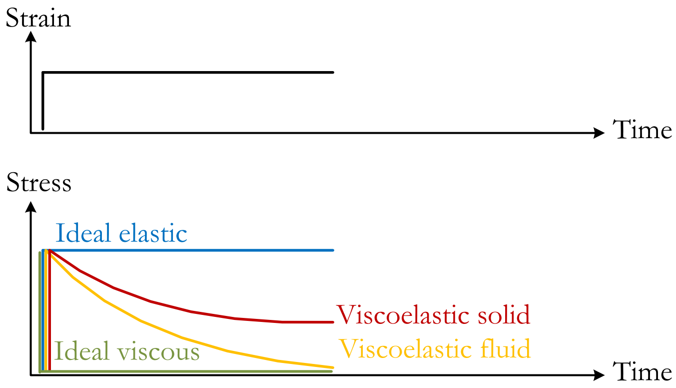

Figure 2.10: Relaxation function for different materials.

For ideal elastic solids after a strain step, no stress relaxation occurs at all, since these kind of materials do not show any viscous portion. However, for ideal viscous liquids after a strain step, immediate and complete stress relaxation occurs. For viscoelastic fluids, delayed but complete stress relaxation takes place if the period of testing is sufficiently long. Moreover, for viscoelastic solids, even after a very long relaxation phase, the stress is relaxing to a certain extent only. The stress curve asymptotically approximates the final value which is the equilibrium stress.

Creep

Creep is the tendency of a solid material to deform permanently under the influence of mechanical stress. It occurs as a result of long term exposure to high levels of stress that are below the yield strength of the material. Figure 2.11 shows creep behaviour for ideal elastic, ideal viscous and viscoelastic materials.

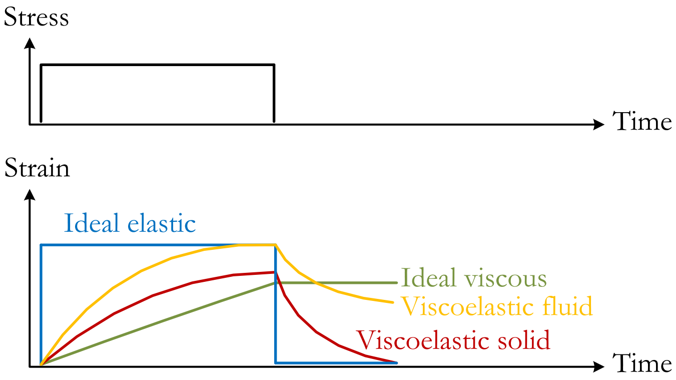

Figure 2.11: Creep function for different materials.

Ideal elastic materials show an immediate deformation after applying a jump-like stress. In the recovery phase, after removing the load, reformation takes place immediately and completely. The total deformation energy which was previously stored by the deformed material during the creep phase will be recovered completely to be used for the reformation precess. In the ideal viscous material, contrarily, after removing the load, there is no reformation at all since these kind of materials do not have any elastic portion. Ideal viscous materials are not able to store any deformation energy during the load interval, and therefore after releasing the load, they finally remain deformed to the same extent like in the end of the load phase. For viscoelastic liquids after releasing the load and even after a longer rest phase, a certain extent of deformation still remains permanently. However, for viscoelastic solids, delayed but complete reformation takes place if the period of testing is sufficiently long (Mezger, 2006).

Hysteresis

When viscoelastic materials have a force applied to them and then removed, it takes more energy to displace the material than it does to return the material to its original configuration. In other words, it consumes more energy during the loading phase (applying a load and stretching the material) compared to the unloading phase (taking the load away and allowing the material to return to its original state). This energy difference is caused by the material losing energy during the loading phase, due to heat dissipation or molecular rearrangement within the material. Figure 2.12 shows this effect, leading to the fact that the stress-strain curve is not the same for loading and unloading.

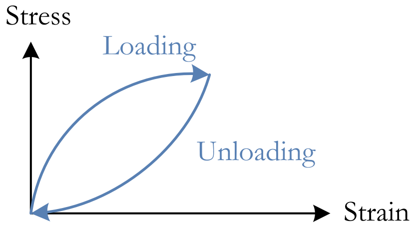

Figure 2.12: Hysteresis effect in viscoelastic materials.

2.1.4 Soft tissues

Once the main properties of materials have been reviewed, the major characteristics of soft tissues are listed (Basdogan, Ho, et al., 2001):

- Non-linear response: displacement versus force profile is non-linear.
- Hysteresis: displacement versus force profiles are different for continuously increasing and decreasing forces.
- Non-homogeneity: displacement versus force curve changes across the tissue.

- Anisotropy: displacement versus force profile depends on the direction of the applied force.

- Large deformations: typical forces result in large and complex deformation fields.

- Viscoelasticity: stress-strain relationship depends on the rate of deformation.

- Viscoplastic behaviour in some cases (Fung, 1981).

2.2 Introduction to continuum mechanics

Once the tissue is characterised and its mechanical properties are known, the physical properties must be expressed using a suitable mathematical model. The constitutive equation of the mathematical model provides the physical meaning to the model. For an adequate understanding of mathematical models, this section, based on (Athanasiou and Natoli, 2008; Holzapfel, 2000) introduces the basis of continuum mechanics. This approach establishes the constitutive equations necessary to model the mechanical behaviour of the tissues. The reader familiar with continuum mechanics should feel free to skip this section.

Being a solid in a reference configuration presented in Figure 2.13, the position of a particle in the body is defined by the vector $\mathbf{X} = (X_1, X_2, X_3)^T$ in the reference configuration and vector $\mathbf{x} = (x_1, x_2, x_3)^T$ in the current configuration. The coordinates X_i and x_i are also called the material and spatial coordinates, respectively. Accordingly, the description in terms of the material variables is called the material (or Lagrangian) description, and the one in terms of the spatial variables is called the spatial (or Eulerian) description.

Let's suppose two points initially close, A and B, separated by d$\mathbf{X}$. The final position of these points can be written as:

- Point A: $\mathbf{x} = \mathbf{X} + \mathbf{u}(\mathbf{X}, \mathrm{t})$
- Point B: $\mathbf{x} + \mathrm{d}\mathbf{x} = \mathbf{X} + \mathrm{d}\mathbf{X} + \mathbf{u}(\mathbf{X} + \mathrm{d}\mathbf{X}, \mathrm{t})$

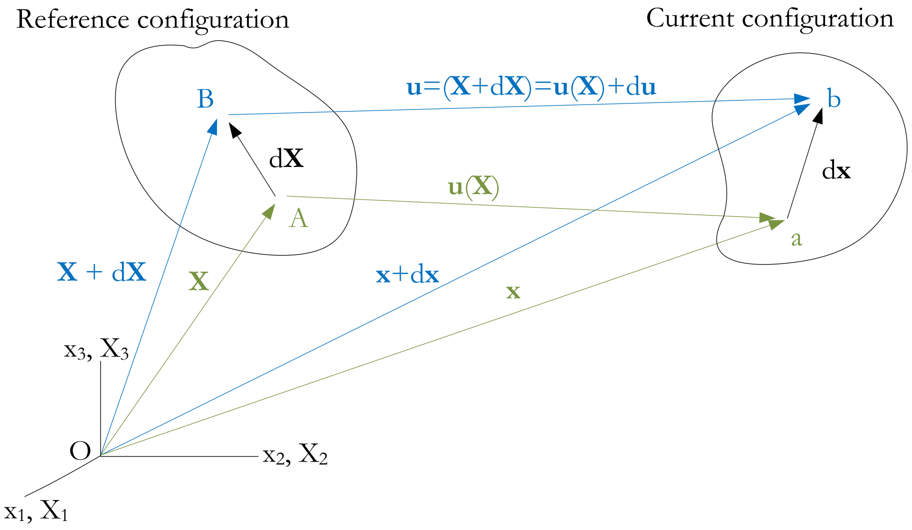

Figure 2.13: Reference and current configuration of a solid.

The primary measure of deformation in non-linear continuum mechanics is the deformation gradient. It is introduced as:

$$\mathbf{F} = \frac{\partial \mathbf{x}}{\partial \mathbf{X}}; \qquad \mathbf{x} = \mathbf{x}(\mathbf{X}, t) \tag{2.7}$$

The deformation gradient is a second-order tensor. Its determinant is conventionally denoted $J = det(\mathbf{F})$ and it is known as the elastic volume ratio.

Strain tensors

In continuum mechanics two different tensors are used for deformation representation, finite and infinitesimal strain tensors. Finite strain tensors measure the real deformation, and they can be used for both small and large deformations, since they can take into account geometrical non-linearities. The infinitesimal deformation tensor is obtained when some non-linear terms of finite tensor are negligible (that is the case of linear elasticity). Different finite deformation tensors are defined in continuum mechanics:

- Green-Lagrange finite strain tensor:

$$\mathbf{E} = \frac{1}{2}(\nabla \mathbf{u} + \nabla \mathbf{u}^T + \nabla \mathbf{u}^T \nabla \mathbf{u}) = \frac{1}{2}(\mathbf{F}^T \mathbf{F} - \mathbf{I}) \tag{2.8}$$

- Right Cauchy-Green deformation tensor:

$$\mathbf{C} = \mathbf{F}^T \mathbf{F} \tag{2.9}$$

- Left Cauchy-Green deformation tensor:

$$\mathbf{B} = \mathbf{F} \mathbf{F}^T \tag{2.10}$$

Linear elasticity is a simplification of the more general non-linear theory of elasticity explained above. Elasticity has two non-linear components: a geometrical one (infinitesimal vs. finite deformations) and a physical one (non-linear constitutive equations). The fundamental *linearizing* assumptions of linear elasticity are: Infinitesimal strains (or *small* deformations) and linear relationships between the components of stress and strain.

In the case of small deformations, the term $\nabla \mathbf{u}^T \nabla \mathbf{u}$ in Equation (2.8) can be ignored, and therefore we get the infinitesimal strain tensor, or Cauchy strain tensor, ϵ:

$$\boldsymbol{\epsilon} = \frac{1}{2}(\nabla \mathbf{u} + \nabla \mathbf{u}^T) = \frac{1}{2}(\mathbf{F}^T + \mathbf{F}) - \mathbf{I} \tag{2.11}$$

Cauchy strain tensor, ϵ, is not rotationally invariant, which means that its value is not $\mathbf{0}$ for pure rigid solid rotations. This fact has important consequences when applied to the FEM, since it is the cause of artifacts when linear FEM models are applied and large rotations are present. Additionally, in this case, the approximation $X_i \approx x_i$ can also be applied.

Thus, linear elasticity theory is valid only for small strains. One of the fundamental drawbacks of using a linear elasticity formulation to describe soft tissues is that surgically relevant strains often significantly exceed the small strain limit, invalidating the assumption of linearity. However, it is used in many simulation applications due to its mathematical simplicity and computational efficiency (Misra, Ramesh, et al., 2008).

Strain energy function

A hyperelastic material supposes the existence of a function which is denoted by the Helmholtz free-energy function, Ψ. This function describes how the material stores the deformation energy. The free-energy function is independent of translations and rotations of the body and it is only dependent on the deformation gradient, $\mathbf{F}$ (Chaves, 2013). The Helmholtz free-energy function is required to satisfy several conditions:

- $\Psi(\mathbf{I}) = 0$, i.e. strain energy function vanishes when the material has been completely unloaded, in the undeformed state, where $\mathbf{F} = \mathbf{I}$.
- $\Psi(\mathbf{F}) \geq 0$, i.e. strain energy must increase monotonically with deformation.
  $$\Psi(\mathbf{F}) > 0 \qquad for \qquad \mathbf{F} \neq \mathbf{I} \tag{2.12}$$
- It must be convex in its arguments and must attain its global minimum at $\mathbf{F} = \mathbf{I}$, and it must increase without bound for large extensions and compressions of the material. These conditions can be written as (Zhurov, Limbert, et al., 2007):

$$\Psi(\mathbf{F}) \rightarrow +\infty \qquad as \qquad J = det(\mathbf{F}) \rightarrow +\infty \tag{2.13}$$
$$\Psi(\mathbf{F}) \rightarrow +\infty \qquad as \qquad J = det(\mathbf{F}) \rightarrow +0 \tag{2.14}$$

In practice, most constitutive laws specify the strain energy density per unit reference volume, W, rather than the Helmholtz free energy, Ψ, just to avoid introducing the mass density, ρ_0, in the stress-strain relations. For isothermal elastic processes, the strain energy, W, is related to the Helmholtz free energy, Ψ by Equation (2.15).

$$W = \rho_0 \Psi \tag{2.15}$$

The constitutive law for a hyperelastic material is defined by an equation relating the strain energy function of the material to the deformation gradient. There are many strain energy functions presented in the literature. Some of them are used in Section 4.2.1.

For isotropic materials, the behaviour of the material is the same in all directions. Therefore, the elastic potential is independent of the coordinate system and it can be expressed as a function of the three invariants (I_1, I_2, I_3) of Right Cauchy-Green deformation tensor, $\mathbf{C}$. These three strain invariants of $\mathbf{C}$ are:

$$\begin{aligned} I_1 &= tr(\mathbf{C}) \\ I_2 &= \frac{1}{2}\big((tr(\mathbf{C}))^2 - tr(\mathbf{C}^2)\big) \\ I_3 &= det(\mathbf{C}) = det(\mathbf{C})^2 = J^2 \end{aligned} \tag{2.16}$$

Stress tensors

Different stress tensors are defined in continuum mechanics. Below, the most notable ones are described.

The Cauchy (true) stress tensor, $\boldsymbol{\sigma}$

Cauchy stress tensor relates forces in the present (deformed/spatial) configuration to areas in the present configuration. The Cauchy stress tensor is symmetric, which is implied from the fact that the equilibrium of an element requires that the resultant moment vanishes.

It can be shown that the Cauchy stress tensor is defined by (Athanasiou and Natoli, 2008):

$$\boldsymbol{\sigma} = 2J^{-1}\mathbf{F}\frac{\partial W}{\partial \mathbf{C}}\mathbf{F}^T \tag{2.17}$$

Using the chain rule,

$$\frac{\partial W}{\partial \mathbf{C}} = \frac{\partial W}{\partial I_1}\frac{\partial I_1}{\partial \mathbf{C}} + \frac{\partial W}{\partial I_2}\frac{\partial I_2}{\partial \mathbf{C}} + \frac{\partial W}{\partial I_3}\frac{\partial I_3}{\partial \mathbf{C}} \tag{2.18}$$

being,

$$\begin{aligned} &\frac{\partial I_1}{\partial \mathbf{C}} = \mathbf{I} \\ &\frac{\partial I_2}{\partial \mathbf{C}} = I_1\mathbf{I} - \mathbf{C}^T = I_1\mathbf{I} - \mathbf{C} \\ &\frac{\partial I_3}{\partial \mathbf{C}} = (\mathbf{C}^2)^T - I_1\mathbf{C}^T + I_2\mathbf{I} = I_3(\mathbf{C}^{-1})^T = I_3\mathbf{C}^{-1} \end{aligned} \tag{2.19}$$

so that,

$$\frac{\partial W}{\partial \mathbf{C}} = \frac{\partial W}{\partial I_1}\mathbf{I} + \frac{\partial W}{\partial I_2}(I_1\mathbf{I} - \mathbf{C}) + \frac{\partial W}{\partial I_3}I_3\mathbf{C}^{-1} \tag{2.20}$$

Therefore, Equation (2.17) becomes

$$\boldsymbol{\sigma} = 2J^{-1}\mathbf{F}\left(\frac{\partial W}{\partial I_1}\mathbf{I} + \frac{\partial W}{\partial I_2}(I_1\mathbf{I} - \mathbf{C}) + \frac{\partial W}{\partial I_3}I_3\mathbf{C}^{-1}\right)\mathbf{F}^T \tag{2.21}$$

In terms of **B**, Equation (2.21) takes the form

$$\boldsymbol{\sigma} = 2J^{-1}\left(I_3\frac{\partial W}{\partial I_3}\mathbf{I} + \left(\frac{\partial W}{\partial I_1} + I_1\frac{\partial W}{\partial I_2}\right)\mathbf{B} - \frac{\partial W}{\partial I_2}\mathbf{B}^2\right) \tag{2.22}$$

The invariants of **B** are the same as the invariants of **C**. It is demonstrated in Equation (2.23).

$$\begin{aligned} I_{1B} &= tr(\mathbf{B}) = tr(\mathbf{F}\mathbf{F}^T) = tr(\mathbf{F}^T\mathbf{F}) = tr(\mathbf{C}) = I_1 \\ I_{2B} &= \frac{1}{2}((tr\mathbf{B})^2 - tr(\mathbf{B}^2)) = \frac{1}{2}({I_1}^2 - tr(\mathbf{F}\mathbf{F}^T\mathbf{F}\mathbf{F}^T)) \\ &= \frac{1}{2}({I_1}^2 - tr(\mathbf{F}^T\mathbf{F}\mathbf{F}^T\mathbf{F})) = \frac{1}{2}({I_1}^2 - tr(\mathbf{C}^2)) = I_2 \\ I_{3B} &= det(\mathbf{B}) = det(\mathbf{F}\mathbf{F}^T) = det(\mathbf{F}^T\mathbf{F}) = det(\mathbf{C}) = I_3 \end{aligned} \tag{2.23}$$

First Piola-Kirchhoff stress tensor, P

First Piola-Kirchhoff stress tensor, also called the Lagrangian stress tensor, relates forces in the present configuration with areas in the initial configuration. The first Piola-Kirchhoff stress tensor is not symmetric.

The first Piola-Kirchhoff stress tensor as a result of deformation can be obtained from

$$\mathbf{P} = \frac{\partial W(\mathbf{F})}{\partial \mathbf{F}} \tag{2.24}$$

The Cauchy stress tensor and First Piola-Kirchhoff stress tensor are related as follows (Athanasiou and Natoli, 2008):

$$\mathbf{P} = J\boldsymbol{\sigma}\mathbf{F}^{-T}, \qquad \boldsymbol{\sigma} = J^{-1}\mathbf{P}\mathbf{F}^{T} = \boldsymbol{\sigma}^{T} \tag{2.25}$$

Second Piola-Kirchhoff stress tensor, S

This symmetric stress tensor relates forces in the initial configuration to areas in the initial configuration.

The second Piola-Kirchhoff strain tensor is defined by Equation (2.26):

$$\mathbf{S} = 2\frac{\partial W(\mathbf{C})}{\partial \mathbf{C}} = 2\left(\frac{\partial W}{\partial I_1}\frac{\partial I_1}{\partial \mathbf{C}} + \frac{\partial W}{\partial I_2}\frac{\partial I_2}{\partial \mathbf{C}} + \frac{\partial W}{\partial I_3}\frac{\partial I_3}{\partial \mathbf{C}}\right) \tag{2.26}$$

Substituting the derivatives of strain invariants defined in Equation (2.19) in Equation (2.26), the Second Piola Kirchhoff stress tensor can be written as:

$$\mathbf{S} = 2\left[\left(\frac{\partial W}{\partial I_1} + I_1\frac{\partial W}{\partial I_2}\right)\mathbf{I} - \frac{\partial W}{\partial I_2}\mathbf{C} + I_3\frac{\partial W}{\partial I_3}\mathbf{C}^{-1}\right] \tag{2.27}$$

The Second Piola Kirchhoff stress tensor is related with the First Piola-Kirchhoff and the Cauchy stress tensors as follows (Athanasiou and Natoli, 2008):

$$\mathbf{P} = \mathbf{F}\mathbf{S}, \qquad \mathbf{S} = \mathbf{F}^{-1}\mathbf{P} \tag{2.28}$$

$$\boldsymbol{\sigma} = J^{-1}\mathbf{F}\mathbf{S}\mathbf{F}^{T}, \qquad \mathbf{S} = J\mathbf{F}^{-1}\boldsymbol{\sigma}\mathbf{F}^{-T} = \mathbf{S}^{T} \tag{2.29}$$

2.2.1 Compressibility

A material which can undergo changes of volume is said to be compressible. The only restriction on this class of materials is that the volume ratio J

must be positive. Since these materials behave quite differently in bulk and shear it is most beneficial to split the deformation locally into a so-called *volumetric component* and an *isochoric component* (Holzapfel, 2000). The volumetric or dilational component of the deformation is related with the change in volume. While, the isochoric or deviatoric component is related to shape change and it takes place without change in volume (as if the material was incompressible). In that way, strain energy is decoupled in both parts as,

$$W(\mathbf{C}) = W_{vol}(J) + W_{iso}(\bar{\mathbf{C}}) \tag{2.30}$$

In the same way, the corresponding stress tensors are also obtained in additive form:

$$\mathbf{S} = \mathbf{S}_{vol} + \mathbf{S}_{iso}, \qquad \boldsymbol{\sigma} = \boldsymbol{\sigma}_{vol} + \boldsymbol{\sigma}_{iso} \tag{2.31}$$

The multiplicative decomposition of the deformation gradient and the right Cauchy-Green tensor into a dilational and a volume-reserving part is defined as:

$$\begin{aligned} \bar{\mathbf{F}} &= J^{-1/3}\mathbf{F} \\ \bar{\mathbf{C}} &= \bar{\mathbf{F}}^T\bar{\mathbf{F}} = J^{-2/3}\mathbf{C} \\ det\bar{\mathbf{C}} &= (det\bar{\mathbf{F}})^2 = 1 \end{aligned} \tag{2.32}$$

where $\bar{\mathbf{F}}$ and $\bar{\mathbf{C}}$ are the isochoric (volume-preserving) part of the corresponding tensors. Isochoric strain invariants are defined as:

$$\begin{aligned} \bar{I}_1 &= J^{-2/3}I_1 \\ \bar{I}_2 &= J^{-4/3}I_2 \\ \bar{I}_3 &= 1 \end{aligned} \tag{2.33}$$

The Cauchy stress tensor for compressible material is defined by:

$$\begin{aligned} \boldsymbol{\sigma} = \frac{2}{J}\left[\frac{1}{J^{2/3}}\left(\frac{\partial W}{\partial \bar{I}_1} + \bar{I}_1\frac{\partial W}{\partial \bar{I}_2}\right)\mathbf{B} - \frac{1}{J^{4/3}}\frac{\partial W}{\partial \bar{I}_2}\mathbf{BB}\right] \\ + \left[\frac{\partial W}{\partial J} - \frac{2}{3J}\left(\bar{I}_1\frac{\partial W}{\partial \bar{I}_1} + 2\bar{I}_2\frac{\partial W}{\partial \bar{I}_2}\right)\right]\mathbf{I} \end{aligned} \tag{2.34}$$

Some strain energy functions for compressible materials are presented as examples. For detailed background of continuum mechanics for compressible materials, the reader is referred to (Holzapfel, 2000).

The Mooney-Rivlin strain energy function in the decoupled form is (Holzapfel, 2000):

$$W(J, \bar{I}_1, \bar{I}_2) = W_{vol}(J) + c_1(\bar{I}_1 - 3) + c_2(\bar{I}_2 - 3) \tag{2.35}$$

being c_1, c_2 material constants.

The Mooney-Rivlin model in a coupled form is:

$$W(J, I_1, I_2) = c(J-1)^2 - dlnJ + c_1(I_1 - 3) + c_2(I_2 - 3) \tag{2.36}$$

being c, d, c_1, c_2 material constants.

The strain energy density function for Neo-Hookean compressible model in the coupled form is:

$$W(I_1, J) = \frac{C_1}{\beta}(J^{-2\beta} - 1) + c_1(I_1 - 3) \tag{2.37}$$

being c_1, β Lamé constants.

2.2.2 Incompressibility

Numerous materials can sustain finite strains without noticeable volume changes. Such types of material may be regarded as incompressible so that only isochoric (volume preserving) motions are possible. For many cases, this is a common idealization and acepted assumption often invoked in continum and computational mechanics (Holzapfel, 2000). The term incompressible means these materials cannot be triaxially compressed i.e. there is no change in volume due to deformation. Soft tissues and rubber are good examples of incompressible or nearly incompressible materials. Materials which keep the volume constant throughout a motion are characterised by the incompressibility constraint, $J = det(\mathbf{F}) = 1$.

It can be demonstrated that the Cauchy stress tensor for an incompressible material becomes (Holzapfel, 2000):

$$\boldsymbol{\sigma} = -p\mathbf{I} + 2\left(\frac{\partial W}{\partial I_1} + I_1\frac{\partial W}{\partial I_2}\right)\mathbf{B} - 2\frac{\partial W}{\partial I_2}\mathbf{B}^2 \tag{2.38}$$

The scalar p can be identified as a hydrostatic pressure. It may only be determined from the equilibrium equations and the boundary conditions.

2.3 Introduction to modelling methods

In order to solve the deformation of solids based on continuum mechanics, computational methods are used. Several computational methods have been proposed in the literature for representing deformable objects and its biomechanical behaviour.

The choice of a deformable model must take two main factors into account: the simulation realism and the computational cost for implementing the model in real-time. Simulation in medicine needs to be realistic enough in order to achieve a correct visual feedback. Realism can be defined as the capacity of a simulation to recreate or reproduce the main physical behaviours of a tissue relevant for a surgery. However, in order to define it from an engineering point of view, the behaviour of the model needs to be similar to the behaviour of the tissue. Due to the variability that biological tissues present, the behaviour of a model is considered accurate when it is able to reproduce the response to a mechanical input whithin the range of the responses of natural tissues.

Moreover, for surgery training and robotic assisted surgery applications, it is important that the model can be run in real-time. For real-time performance, a screen refresh rate of approximately 20 Hz (Dogan and Serdar Celebi, 2010) or 24 - 25 Hz (Lapeer, Gasson, et al., 2011) is needed, which corresponds to the critical fusion frequency of the human eye. However, the human tactile sensory system is much more sensitive, hence, the haptic device requires an update rate between 300 Hz and 1 kHz (depending on the stiffness of the material) (Lapeer, Gasson, et al., 2011).

These two requirements are present in the simulation methods developed in the literature. Depending on the application, authors tend to pay more attention to one or other simulation requirement.

Physics-based simulation methods are based on continuum mechanics and they get accurate simulation results by directly solving the partial differential equations (PDEs) using numerical methods, unlike non-physical models, that use intuitive methods instead of solving PDE. In other words, physically based methods use the laws of physics to model objects, calculating internal and external forces in order to determine an object's deformation. It should be kept in mind that physically based methods uses some assumptions and approximations to model real life object. This is the case of the well-known finite element method (FEM).

Other models such as mass-spring models have been also used for surgical simulations. Some of them are explained below. For an in-depth review of deformable models, there is an extensive literature (Meier, López, et al., 2005; Nealen, Müller, et al., 2005).

2.3.1 Finite Element Method (FEM)

One of the most important advances in the field of numerical methods was the development of the finite element method (FEM) in the 1950s. In the FEM, a continuum with a complex shape is divided into simple finite elements. The individual elements are connected together by a topological map called the mesh. The FEM is a robust and thoroughly developed method, and hence it is widely used in engineering fields due to its versatility for complex geometry and flexibility for many types of linear and non-linear problems (Liu and Gu, 2005).

FEM is a physically accurate approach, which solves the partial differential equations which govern the dynamics of an elastic material. FE models achieve a discrete approximation by dividing the region of interest into volumetric elements. Each volumetric element connects only to neighboring elements via shared nodes. The deformation (and thus energy) for points within an element is interpolated from the element's nodes (Liu, Tendick, et al., 2003). In surgical simulation, for example, the geometric model of an organ is divided into surface or volumetric elements, properties of each element are formulated, and the elements are assembled together to compute the deformation states of the organ for the forces applied by the surgical instruments (Kim, Muniyandi, et al., 2004).

Finite element models have become the focus of current surgical simulation applications due to their increased accuracy and continuous representation of volumetric tissue deformation. The improvement in realistic deformation however, comes at the cost of computational complexity, particularly when there are non-linearities. Researchers have used both linear and non-linear finite element methods to develop real-time models. Some of the FEM models used in surgical simulations are listed in Section 4.1.

Linear finite element models are probably the most widely used approaches to model tissue deformation in surgical simulators. Motivating factors are simplicity of implementation and computational efficiency, which enables for example, real-time haptic rendering (Misra, Ramesh, et al., 2008). In this case, the mechanical behaviour of soft tissue is modelled with linear elastic constitutive equations where tissue undergoes infinitesimal deformations. Linear elasticity is only valid for small displacements and rotations. In many simulations the first hypothesis (small displacements) is valid but not the second (small rotations). For that reason, artifacts can appear when elements suffer large rotations, i.e., elements that rotate increase their volume. To avoid this effect the co-rotational approach has also been applied. The application domain of the co-rotational approach is limited by a priori kinematic assumptions: displacements and rotations may be arbitrarily large, but deformations must be small (Felippa and Haugen, 2005).

However, in the vast majority of surgical applications, strain can reach high values, therefore, large deformations and non-linearity should be considered (Sokhanvar, Dargahi, et al., 2008). Whereas non-linear FEM models display more realistic deformations than linear FEM models, they have a greater computational complexity because of the system's non constant stiffness matrix (Sedef, Samur, et al., 2006).

The two main sources of non-linear behaviour are geometric and material non-linearities. The geometric non-linearity is caused by a finite change in the geometry of the model due to the presence of non infinitesimal strains.

So that, the hypothesis that the final deformed position corresponds to the starting position cannot be accepted (Celigüeta, 2009). Furthermore, material non-linearities occur when the stress-strain or force-displacement law is not linear, or when material properties change with the applied loads.

The most usual approach to address the non-linear FEM is Lagrangian formulation. Lagrangian kinematics follow the body (or element) as it moves. In other words, the movement is characterised according to the material coordinates, i.e., the final coordinates of the particle are expressed in terms of its initial coordinates. Within this Lagrangian approach there are two different formulations, differing only in the configuration that is used as a reference for deformation measurements: Total Lagrangian (TL) and Updated Lagrangian (UL).

In Total Lagrangian (TL) formulation, calculations are done in the undeformed state, i.e. all variables are referred to the original configuration of the system. The decisive advantage is that all derivatives with respect to spatial coordinates are calculated with respect to the original configuration and, therefore, can be pre-computed (Miller, Joldes, et al., 2007). TL formulation is explained in Section 2.3.3.

In Updated Lagrangian (UL) formulation, calculations are done in the deformed state. All variables are referred to the current (i.e. from the end of the previous time step) configuration of the system. The great majority (if not all) of commercial finite element programs use the updated Lagrangian formulation (Ansys, Abaqus, Adina, LS Dyna). The disadvantage is that all derivatives with respect to spatial coordinates must be recomputed in each time step, because the reference configuration is changing (Miller, Joldes, et al., 2007).

Using the FEM hypothesis, a problem defined in the continuum as a partial differential equation is transformed into a system of ordinary differential equations that can be integrated in time using numerical methods. Computing the deformation field and internal forces (stresses) within a soft organ during surgical procedure requires the application of an efficient numerical scheme when integrating equations of equilibrium (or dynamics) in time domain. These numerical methods to solve a dynamic equilibrium equation at every time step can be explicit or implicit.

Explicit methods predict the solution at time $t+\Delta t$ by using the solution at time t. Therefore, the explicit time integration can be performed without iteration and without solving a system of linear algebraic equations. However, explicit methods are conditionally stable. Normally, a severe restriction on the time step size has to be included in order to receive satisfactory simulation results (Miller, Joldes, et al., 2007). These short time steps increase the computational effort but it can help in some cases to obtain a very stable contact formulation. However, the disadvantage of this method (that many steps have to be taken) is not so significant since each step is much less time consuming than in an implicit algorithm (Székely, Brechbühler, et al., 2000).

Implicit methods solve the equation at time $t+\Delta t$ based on itself, and also using the solution which has been found for time t. The equations of dynamics are combined with the time integration operator and the displacements are found directly. The most commonly used implicit integration methods are unconditionally stable. This implies that their time step is limited only by the convergence and accuracy considerations. However, implicit methods require the solution of a set of non-linear algebraic equations at each time step. Furthermore, iterations need to be performed for each time step of implicit integration to control the error and prevent divergence. Therefore, the number of numerical operations per each time step can be three orders of magnitude larger than for explicit integration (Miller, Joldes, et al., 2007).

2.3.2 Other methods

Next, some methods apart from FEM are listed, in order to have a wider idea of the available computational methods.

The Boundary Element Method (BEM) is an alternative computational mechanics technique for modelling the deformation of complex objects. This technique has also been used for surgical simulation (Monserrat, Meier, et al., 2001; Wang, Becker, et al., 2006).

In contrast to FE methods, BE technique only requires the modelling of the surface of an elastic object without having to discretize the interior of the body, thus reducing the size of the equation system to be solved. It offers potential advantages in saving computational cost and improving mesh generation efficiency. These factors suggest that the BE method might potentially be a more suitable technique than the FE method for modelling real-time deformable objects, because it may prove an effective method for computing deformations more rapidly (Wang, Becker, et al., 2005). However, the BEM is not very suitable for dealing with material heterogeneity and non-linear fundamental equations, which is unfortunately always the case in biomedical problems (Wang, Becker, et al., 2005). Besides, its performance is still limited (Zhong, Wachowiak, et al., 2005).

The mass-spring model (MSM) uses point masses connected by a network of springs to represent continuous material. Due to their intrinsic simplicity and computational efficiency, they can be rapidly updated and the method is well suited for surgical simulations where visually plausible deformations must be presented in real time. For this reason, the mass-spring models have been widely implemented for surgical simulators in the literature (Brown, Sorkin, et al., 2002; Keeve, Girod, et al., 1998; Skrinjar, Nabavi, et al., 2002).

However, there are several significant drawbacks of these models in the context of medical applications. They do not incorporate real physical material parameters and hence they are only weakly related to the physical behaviour of biological soft tissues. The mass-spring models cannot meet the requirements for accurately describing the desired measurements such as displacement, stress or pressure distribution. This kind of models is inadequate for applications where accuracy is a critical concern, such as brain shift compensation and the simulation of brain structural disease development. Besides, the model parameters are mesh-dependent, meaning that they have to be recalculated at any change to the mesh density (Chunping, 2007).

The meshfree (or meshless) methods, in contrast to the mesh-based methods listed above, discretize the object by merely using a set of nodes without a mesh structure. These methods possess several advantages such as the re-meshing efficiency, which permits to deal with the large distortions of soft materials (muscles, internal organs, skin, etc.) or to explicitly simulate the fluid flow (the hemodynamics, the swallow, the respiration, etc.). The accuracy and smoothness of the stress fields obtained with meshless methods are also very useful to predict the remodelling process of biological tissues and the rupture or damage of such biomaterials (Belinha, 2014).

One example of the meshfree methods is Smoothed-Particle Hydrodynamics (SPH) that study inter-particle interactions. This makes them especially suitable for the simulation of solids at atomic-scale and fluids. The basic idea of SPH is that the state of a system can be represented by arbitrarily distributed particles (Liu and Gu, 2005). Each node (or particle) is represented by its own position, velocity, and acceleration and moves under the influence of forces applied by the surgical instrument (Zhu, Gu, et al., 2010).

However, several problems remain in pure particle-based methods. One of them is the simulation resolution. Since the objects in the scene are all represented by discrete points with the same support field, it is difficult to describe some deformation details on the organ surface, which is visually important in surgical simulation (Zhu, Gu, et al., 2010). Besides, the integration of realistic tissue properties into particle models is not a trivial task. The construction of an optimal network of springs in 3D is a complicated process and particle systems can become oscillatory or even unstable under certain conditions (Kim, Muniyandi, et al., 2004).

With the aim of facing the drawbacks of meshfree methods and combining the advantages of different methods, some hybrid methods have also been developed for simulating soft tissues. As example, Zhu, Gu, et al. (2010) introduce an auxiliary surface mesh into the existing particle-based simulation framework, and utilize the pre-computed surface data with experimental biomechanics parameters for deformable modelling. In Zhu and Gu (2012), they propose a new hybrid deformable model using boundary element method (BEM) to compute global deformation based on a coarse surface mesh and using a mass-spring model to simulate the dynamic behaviour of soft tissue interacting with surgical instruments. Both models have been integrated into a real-time, surgical training system for laparoscopic surgery.

2.3.3 Total Lagrangian Method

This section presents the non-linear Total Lagrangian explicit Finite Element Formulation using a tetrahedral mesh. This kind of formulation is well suited to surgery simulators since it provides a very compact and efficient implementation. The formulation can handle easily non-linear material and large deformations. Additionally the method does not require the computation of a stiffness matrix, which allows an easy adaptation to topological changes.

This formulation allows a direct computation of the elastic forces acting on each node when the model is deformed, as detailed below.

In a Lagrangian approach, the dynamic analysis is performed by tracking the material particles forming a body. In particular, two sets of coordinates can be defined, the spatial coordinates, $\mathbf{x}$, which represents the position of one particle in the deformed state, and its original position or material coordinates, $\mathbf{X}$. In a total Lagrangian representation, all forces, deformations and material stresses are expressed in the material coordinate system, $\mathbf{X}$. We iterate per element and compute the deformation gradient tensor, $\mathbf{F}$.

$$\mathbf{F}(\mathbf{X}) = \frac{\partial \mathbf{x}(\mathbf{X}, t)}{\partial \mathbf{X}} \tag{2.39}$$

In the case of tetrahedral elements, $\mathbf{F}$ can be expressed as:

$$\mathbf{F} = [\mathbf{x}_2 - \mathbf{x}_1, \mathbf{x}_3 - \mathbf{x}_1, \mathbf{x}_4 - \mathbf{x}_1][\mathbf{X}_2 - \mathbf{X}_1, \mathbf{X}_3 - \mathbf{X}_1, \mathbf{X}_4 - \mathbf{X}_1]^{-1} \tag{2.40}$$

The Cauchy stress tensor, $\boldsymbol{\sigma}$, is related with the material model by the strain energy function, W, as Equation (2.41):

$$\boldsymbol{\sigma} = \frac{2}{\sqrt{I_3}}\left[\frac{\partial W}{\partial I_1}\mathbf{B} + I_1\frac{\partial W}{\partial I_2}\mathbf{B} - \frac{\partial W}{\partial I_2}\mathbf{BB}\right] + 2\sqrt{I_3}\frac{\partial W}{\partial I_3}\mathbf{I} \tag{2.41}$$

being $\mathbf{B}$ the left Cauchy-Green deformation tensor and I_i the invariants of $\mathbf{B}$. The left Cauchy-Green deformation tensor is related with deformation gradient tensor as Equation (2.42).

$$\mathbf{B} = \mathbf{F}\mathbf{F}^T \tag{2.42}$$

And invariants of $\mathbf{B}$ are defined as Equation (2.43):

$$\begin{aligned} I_1 &= tr\mathbf{B} \\ I_2 &= \frac{1}{2}[(tr\mathbf{B})^2 - tr\mathbf{B}^2] \\ I_3 &= J^2 = (det\mathbf{B})^2 \end{aligned} \tag{2.43}$$

The Cauchy stress tensor, $\boldsymbol{\sigma}$, is defined with regards to the current configuration of the body. Using Total Lagrangian formulation, it is convenient to define the stress tensor with regards to the initial configuration of the object. First Piola-Kirchhoff stress tensor, $\mathbf{P}$, relates the deformation of the element and the mechanical stress in the material, expressed in material coordinates.

$$\mathbf{P} = J\boldsymbol{\sigma}\mathbf{F}^{-T} \tag{2.44}$$

When the constitutive model is given as a first Piola-Kirchhoff stress $\mathbf{P}$, an element's contribution to the finite element force on one of its nodes $\mathbf{x}_a$ is given as (Irving, Teran, et al., 2005):

$$\mathbf{f}_a^e = \int_{\Omega_m} \mathbf{P}\frac{\partial N_a^T}{\partial \mathbf{X}} d\mathbf{X} = \int_{\Omega_{x}i} \mathbf{P}\frac{\partial N_a^T}{\partial \mathbf{X}} d\left|\frac{\partial \mathbf{X}}{\partial \xi}\right| \xi \tag{2.45}$$

where, Ω_m and Ω_ξ represent the volume of the element in either the global framework and in an ideal system based on isoparametric coordinates. N_a represents the interpolation function for node a and $\mathbf{X}$ the material coordinates of a particle.

$\mathbf{P}$ is constant within a tetrahedron and the integrals can be easily computed, leading to a force generated by each element in each node a equivalent to

$$\mathbf{f}_a^e = -\frac{1}{3}\mathbf{P}\sum_{i \neq a} A_i \mathbf{N}_i \tag{2.46}$$

where $A_i\mathbf{N}_i$ are the area weighted normals of the faces of the tetrahedron incident in node a in the original position which can be precomputed.

The total elastic force acting upon the node a is the sum of the contributions of each element sharing node a:

$$\mathbf{f}_a = \sum \mathbf{f}_a^e \tag{2.47}$$

After the value of elastic forces is updated, we can iterate through each node of the mesh computing its next position and velocity using an explicit integrator. The simulation is performed with a time step (Δt) that has to be computed previously to guarantee the stability of the integrator. In the case of a *Euler Semi-Implicit* integrator the equations are:

$$\begin{aligned} \mathbf{v}_a(t+\Delta t) &= \mathbf{v}_a(t) + \frac{\mathbf{f}_a(t)}{m_a}\Delta t \\ \mathbf{x}_a(t+\Delta t) &= \mathbf{x}_a(t) + \mathbf{v}_a(t+\Delta t)\Delta t \end{aligned} \tag{2.48}$$

being m_a the mass of the node a. The mass matrix is considered diagonal. See Irving, Teran, et al. (2005) for additional details of the method.

2.4 Discussion

Mechanical properties of deformable solids have been presented. Theorical aspects of elasticity and viscosity have been stated, in order to understand the behaviour of viscoelastic materials. Elasticity can be considered linear (Hookean solid) or non-linear, as well as viscosity that can be considered linear (Newton fluid) or non-linear. Depending on these considerations severals mathematical models can be defined, depending on the constitutive equation. Several of those mathematical models are presented in Chapter 4.

It must be borne in mind that the model that represents the behaviour of a material is always an idealisation. The model represents some characteristics of the material and it excludes others. The selection of the characteristics to be modelled depends on the reality that is simulated, in other words, it depends on the application. This work is focused on the modelling of soft tissues for surgical applications. Previous to the modelling of the material, it is essential to know the mechanical properties of the tissue. With this purpose, and without losing sight of the application, the tissue is experimentally tested in Chapter 3. In that way, based on the results obtained experimentally and considering the implementation framework of surgical procedures, some simplifications will be taken for the modelling.

In order to simulate the stress state of a deformable solid, it is possible to solve the problem for simple geometries, but not for complex ones. That is the reason for applying a modelling method. There is a wide range of choices for simulating deformable objects. FEM is able to solve a complex geometry dividing it into simpler geometries. Moreover, its integration in real time is possible using a Lagrangian explicit method.

Linear FEM assumes small deformations as well as a linear material definition. While, non-linear FEM is able to take large deformations as well as material's non-linearities into account.

Summarizing, the objective pursued (accuracy, real-time, robustness, etc.) and the considerations made regarding the soft tissue under surgical loads (load mode, velocity, deformation range, etc) determine the simulation method (FEM, others) as well as the mathematical model used (linear, non-linear, viscoelastic, etc) respectively.

CHAPTER 3

CHARACTERISATION OF BIOLOGICAL SOFT TISSUE

The characterisation of the mechanical properties of a tissue plays an important role in the modelling of a soft tissue with a realistic physical behaviour. There is no agreement in the literature about the actual values of the mechanical properties (such as Young's modulus, shear modulus or Poisson's ratio) of soft tissues, because of the high number of factors that affect them: in-vivo or ex-vivo or procedures, the testing protocol, the tested specimen (the species, genre, age of the tissue) or the preconditioning of the sample are some of them. Other factors including heterogeneity, anisotropy, temperature and hysteresis also influence these measurements.

When modelling a material, one important question is to determine the deformation range to be modelled and therefore the range of deformation at which the tissue will be deformed. In the field of surgical simulation, this question is answered by the no returning point that causes tissue damage. This damage can lead to loss of function or tissue death. It is important to make a clear distinction between functional and mechanical damage. Functional damage can be considered as injury, i.e., change or loss of functionality of the tissue (for example the brain), whereas the mechanical damage only affects the mechanical properties of the tissue (Hrapko, Van Dommelen, et al., 2006). No significant immediate mechanical damage affecting the stress-strain behaviour and no structural changes were observed up to shear strain of 0.45 (Hrapko, Van Dommelen, et al., 2006) or 0.5 (Prange and Margulies, 2002) in porcine brain tissue. However, functional damage can occur in absence of mechanical damage. The functional failure of neural tissue at low loading rates is believed to occur in the range of 10% - 15% shear strain for bovine brain tissue (Darvish and Crandall, 2001).

Another question is the velocity at which the tissue is loaded. Since soft tissues are viscoelastic materials, they do not have the same response at slow or high strain rates. In this way, a distinction between static and dynamic loads should be done. A static load is time independent, while dynamic loads are time dependent and for which inertial effects cannot be ignored. Furthermore, quasi-static load is defined as time dependent but it is slow enough such that inertial effects can be ignored, e.g. when strain rates are slower than 0.1 s^{-1} . Moreover, strain rate will still be included for calculating stresses in the viscoelastic constitutive relation (Kyriacou, Mohamed, et al., 2002). The strain rate value relevant to surgical procedures is about 0.01 s^{-1} (Misra, Ramesh, et al., 2010) or 0.01 - 1 s^{-1} (Gao, Tay, et al., 2006). Brain deformation during surgery is a relatively slow process with negligible dynamic components, therefore, it is quite common to assume a quasi-static model (Misra, Ramesh, et al., 2010).

Another important question when characterising any material is the deformation mode, i.e. the type of loading to which the sample is subjected. There is no agreement about the better testing protocol, and therefore several different tests have been developed in the literature (see Section 3.1). However, several authors justify the presence of shear loads at surgical procedures. Misra, Ramesh, et al. (2010) assert that shear is a common mode of organ deformation either during surgical tool-tissue interaction or during palpation by the hand of the clinician. Horgan and Murphy (2010) state that shearing is induced in soft tissues in numerous physiological settings. Darvish and Crandall (2001) affirm that deformation of the brain is mainly of the shear type due to its incompressibility. Besides, Cheng, Clarke, et al. (2008)

stated that for brain tissue, shear testing is commonly conducted, because it is believed that the primary mechanism behind traumatic brain injury (TBI) is high shear strain.

This chapter presents a methodology in order to carry out the characterisation of biological soft tissues. Section 3.1 summarises the different methods that have been conducted in the literature to characterise tissues. Section 3.2 proposes the methodology to test the tissue at shear loads. Firstly, experimental setup of a parallel plate rheometer is shown. Secondly, rheological tests performed are explained. Lastly, the methodology is applied to an agar gel. Afterward, in Section 3.3 the methodology is applied to porcine brain tissue. Finally, a discussion is presented in Section 3.4.

3.1 State of the Art

Several tests can be found in the literature, determining the mechanical properties of biological soft tissues. These tests can be classified into two main groups: in vivo and in vitro experiments. In vivo experiments are performed in real conditions of the body but are more complex to perform due to ethical requirements. In vitro experiments are easy to perform in the laboratory, but do not reproduce the living conditions of the tissue.

3.1.1 Methods for tissue characterisation In Vivo

Magnetic Resonance Elastography (MRE)

Magnetic Resonance Elastography (MRE) is a non-invasive medical technique that measures the mechanical properties of soft tissues by introducing shear waves and imaging their propagation using magnetic resonance imaging (MRI).

This technique is nowadays under research, but is widely used in several parts of human body. Liver MRE has been widely investigated for the diagnosis of hepatic diseases (Venkatesh, Yin, et al., 2008; Yin, Talwalkar, et al., 2007). It is used in clinical practice for fibrosis and cirrhosis assessment. It is also being investigated as a means to characterise hepatic tumours. Breast MRE is being investigated for the assessment of breast cancer. Skeletal muscle MRE has also been extensively investigated for studying the stiffness of skeletal muscle since it is well known that the stiffness changes significantly depending upon the contractile state of the muscle. Skeletal muscle MRE can be used for studying the physiological response of diseased and damaged muscles. Brain MRE is another area of significant research and clinical interest due to the diagnostic potential of brain tissue stiffness information as it may be related to diseases like Alzheimer's disease, hydrocephalus, brain cancer and multiple sclerosis (Wuerfel, Paul, et al., 2010). For further details and references of these studies, the reader is referred to Mariappan, Glaser, et al. (2010).

Supersonic Shear Imaging (SSI)

Supersonic Shear Imaging (SSI) is an ultrasound based technique for real time visualization of soft tissue viscoelastic properties (Bercoff, Muller, et al., 2003), i.e., it is able to provide quantitative shear modulus mapping of an organ in less than 30 ms (Bercoff, Pernot, et al., 2004). This technique is based on the velocity estimation of a shear wave generated by radiation force.

The first in vivo investigations made on healthy volunteers emphasized the potential clinical applicability of this technique for breast cancer detection (Bercoff, Pernot, et al., 2004). This technique was not only applied to human breast (Jiang, Li, et al., 2015), but also to several tissues such as human liver (Muller, Gennisson, et al., 2009), human muscle (Maïsetti, Hug, et al., 2012). This technique was also applied to ex vivo porcine cornea (Tanter, Touboul, et al., 2009).

Measurements in surgical procedures

In invasive methods, measurements are acquired via direct contact with organs. The easiest way to access to the organs or tissues is during open surgery, since less restrictions exist regarding the size of the testing devices.

Different invasive methods were developed in the literature. Indentation method was applied during open surgery to obtain mechanical properties of porcine liver and kidney (Kim and Srinivasan, 2005) or even human liver in (Carter, Frank, et al., 2001). Indentation was also performed in human cadaveric soft tissues by Lim, Deo, et al. (2009). Miga, Paulsen, et al. (2000) measured porcine brain tissue displacement during controlled surgical intervention by the insertion of stainless steel beads forming a grid of markers within the tissue. Kauer, Vuskovic, et al. (2002) developed a tissue aspiration method (see Figure 3.1) for the in vivo determination of biological soft tissue material parameters during open surgeries.

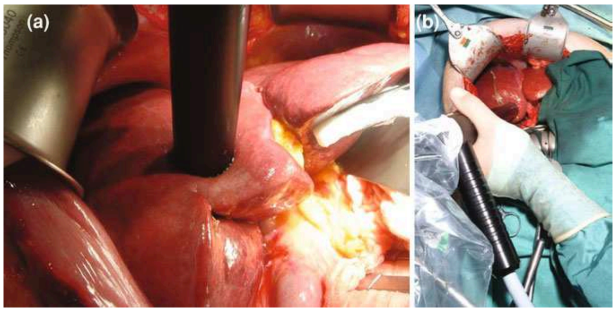

Figure 3.1: Images from in vivo aspiration experiments on the liver from (Hollenstein, Bajka, et al., 2012).

3.1.2 Methods for tissue characterisation In Vitro

Tension

Soft tissues were characterised at tensile loads on several occasions in the literature. Porcine brain tissue was tested at strain rates of 0.01 s^{-1} (Miller and Chinzei, 2002; Velardi, Fraternali, et al., 2006), 0.64 s^{-1} (Miller and Chinzei, 2002), 2 s^{-1} or 90 s^{-1} (Rashid, Destrade, et al., 1991).

Other organs such as porcine and human renal capsules were also tested at tension loads at strain rate range of 0.005 - 250 s^{-1} (Snedeker, Niederer, et al., 2005). Calvo, Sierra, et al. (2014) tested the viscoelastic behaviour of rabbit abdominal wall at 0.1 s^{-1}. Porcine liver was tested by (Gao, Lister, et al., 2010) at tension, compression and shear loads at strain rate of 0.05 s^{-1}.

Human brain tissue was tested by (Franceschini, Bigoni, et al., 2006) at strain rates about 0.005 - 0.009 s^{-1}. Jin, Zhu, et al. (2013) tested human brain tissue at tension, compression and shear at strain rates of 0.5, 5 and 30 s^{-1}.

Compression

Porcine brain tissue was tested at compression loads at strain rates from 0.0000064 to 1 s^{-1} in (Hrapko, Van Dommelen, et al., 2008a; Miller and Chinzei, 1997; Prevost, Balakrishnan, et al., 2011). Bovine brain tissue was tested at 10 s^{-1} by Laksari, Shafieian, et al. (2012).

Other tissues, such as pigskin was also tested at compression loads at different loading speeds, that are in a strain rate range of 0.0002 - 0.27 s^{-1} (Wu, Dong, et al., 2003).

Shear

For shear characterisation of the brain tissue, several tests were carried out in the literature, however, some of them were performed at high strain rates, in order to simulate Traumatic Brain Injury (TBI) more than surgery simulation. For example, Shafieian, Bao, et al. (2011) tested bovine brain tissue at strain rates of 100, 500 and 800 s^{-1}. Darvish and Crandall (2001) applied forced vibrations from 0.5 to 200 Hz in bovine brain tissue. Other shear tests were performed at 10 s^{-1} in a bovine brain (Shafieian, Laksari, et al., 2012) or at 30 s^{-1} in porcine brain tissue (Rashid, Destrade, et al., 2013).

Shear tests at lower strain rates are commonly carried out in a rotational rheometer. Bilston, Liu, et al. (2001) used a parallel plate rheometer to analyse the response of bovine brain tissue to steady shear until failure at different strain rates (0.055 - 0.2335 - 0.947 s^{-1}). They also performed shear relaxation tests (at strain range of 0.1% - 15%), and frequency sweeps over a range of 0.01 - 20 Hz (at strain of 0.1%). Hrapko, Van Dommelen, et al. (2006) presented several shear experiments in a porcine brain tissue at shear rates from 0.01 to 1 s^{-1} at strains up to 0.15. They also performed amplitude sweeps (at 0.16, 1.6 and 16 Hz), frequency sweeps (at 1% strain) and relaxation tests (at 1%, 5%, 10%, 15% and 20% strain).

Nasseri, Bilston, et al. (2002) tested pig kidney in a rheometer performing amplitude sweep (at $1Hz$), frequency sweep (at 0.2% strain), relaxation test (at 0.2% strain) and shear tests between 0.1 and 1 s^{-1}.

3.2 Proposed methodology

In this study, due to the presence of shear loads at surgical procedures and due to the availability of a rotational rheometer as testing machine, simple shear load is considered.

This section presents the experimental setup and the proposed methodology for characterisation of soft tissues at shear loads. As a first step, the methodology is applied to an agar gel (Section 3.2.3). This material is more accessible and simpler to work with than a biological tissue. Besides, it helps to decrease the difficulties that biological tissues present, such as anisotropy or non-homogeneity. The results obtained from the characterisation of the agar gel provide a guide to make some simplifications into the methodology. Some of these experiments can provide slightly different results in the case of brain tissue. However, the differences are not considered large enough to require a different approach.

As it has been seen in Chapter 2, the mechanical behaviour of viscoelastic materials, such as soft tissues, is dependent on temperature and pressure. However, as the purpose of this work is to model the mechanical behaviour of soft tissue for surgical simulation applications, the effects of pressure and temperature are not analyzed. Temperature remains constant in the human body (36 - 37°C) and pressure is also considered constant (the value will be determined for each human body's part and for each procedure).

3.2.1 Experimental setup

The experimental setup used in this work is a parallel-plate rheometer (Anton Paar Physica, MCR 301), shown in Figure 3.2. The specifications of this device are collected in Appendix B. The sample is placed between the top plate (rotating measuring plate) and the lower plate (fixed measuring plate). The top plate of the rheometer is lowered until it contacts the upper surface of the specimen.

Figure 3.2: Parallel plate rheometer (Anton Paar Physica, MCR 301).

Shear deformation and shear rate are not constant in the shear gap. They increase from zero in the center of the plate to the maximun at the edge. Reported data is related to the edge of the plate, where maximum deformation and maximum shear rate occur.

Shear deformation and shear rate are also dependent on the distance between the plates, as can be seen in the following equations. Setting a larger distance, with the same rotational speed (or deflection angle) a lower shear rate (or deformation) is achieved.

Shear rate, $\dot{\gamma}$ [s^{-1}], is defined by Equation (3.1),

$$\dot{\gamma}(R) = \frac{v}{H} = \frac{\omega R}{H} = \frac{2\pi n R}{60H} \tag{3.1}$$

where ω [rad/s] is the angular velocity, R [mm] the radius of the plate, H [mm] the gap between the plates and n [rpm] the rotational speed. Maximum value of shear rate value takes place at the edge of the plate, where the circunferential speed is applied, $v_{max} = v(R) = \omega R$.

Measured strain, γ, is a function of the radius of the plate, R, the gap, H and the deflection angle, φ, as follows:

$$\gamma = \frac{\varphi R}{H} \tag{3.2}$$

Shear stress is determined by Equation (3.3),

$$\tau(R) = \frac{2M}{\pi R^3} \tag{3.3}$$

where M [Nm] is the torque and τ [Pa] the shear stress.

Viscosity is related to the edge of the upper plate holds (i.e. related to the maximal shear rate) as,

$$\eta = \frac{\tau}{\dot{\gamma}} = \frac{2MH}{\pi R^4 \omega} \tag{3.4}$$

3.2.2 Description of the tests

Figure 3.3 shows the methodology followed in order to characterise the soft tissue in a parallel plate rheometer. The first test to be performed is an amplitude test, in order to determine the linear viscoelastic (LVE) limit of the tissue. Knowing the LVE limit, other tests are performed within LVE range. The frequency test is an oscillatory test that provides the dynamic modulus of the material. Controlled shear rate tests give the viscosity curves as well as the time dependent flow behaviour. Finally, creep or relaxation tests can be performed in order to observe the viscoelastic behaviour of the material. Each test is explained below.

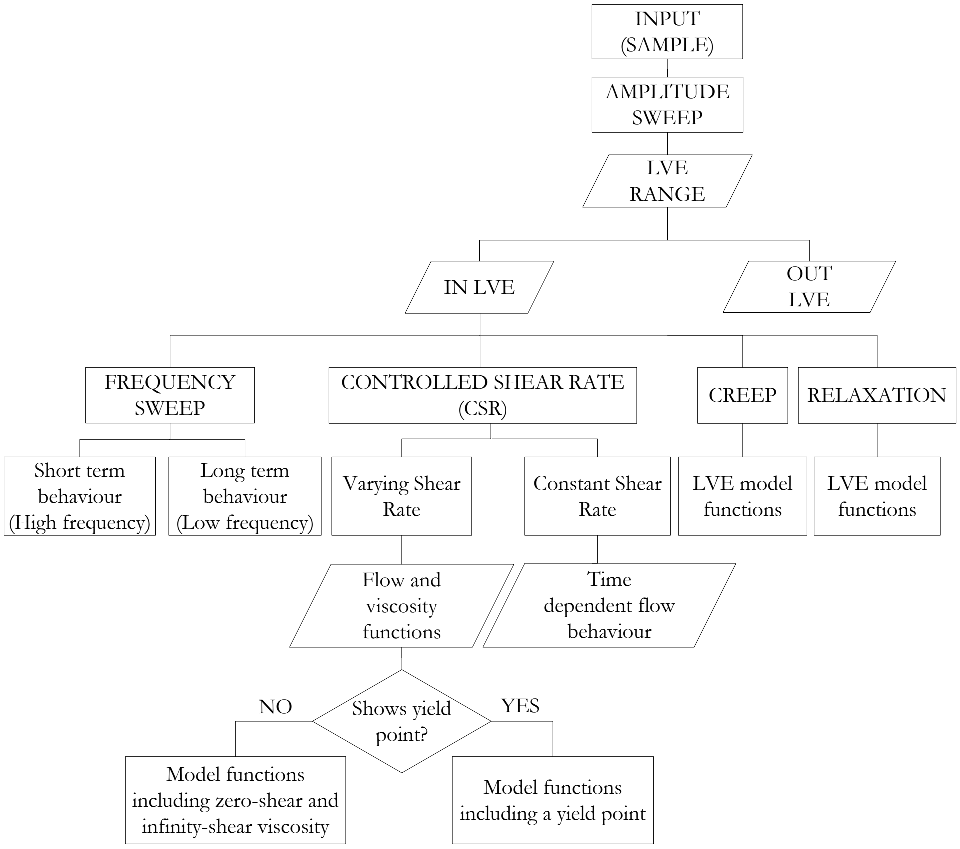

Figure 3.3: Methodology for the characterisation of soft tissues in a rheometer.

Amplitude Sweep

The first step to perform in this methodology is an amplitude test. Amplitude Sweeps (AS) are oscillatory tests performed at variable strain amplitudes, keeping frequency at a constant value. In order to characterise a viscoelastic material, it is important to determine the Linear ViscoElastic (LVE) domain, where the values of the dynamic properties remain steady. Otherwise the results will be dependent on the experimental details and they won't be unique to the material (Liu and Bilston, 2000). As long as strain amplitudes are still below the limiting value γ_L, which defines the limit of LVE range, the material shows reversible-viscoelastic behaviour. It will deform elastically and will return to its original shape when the applied stress is removed. However, at amplitudes higher than γ_L, some fraction of the deformation will be permanent and non-reversible, or the structure of the sample can even be completely destroyed. The limiting value of the LVE range in terms of the shear stress, is the yield stress, τ_y. The yield stress depends on both the strain rate and the temperature at which the deformation occurs. In general, the yield stress increases with strain rate and decreases with temperature. However, as it has been explained above, the temperature is considered constant in this work, and therefore, its influence is not taken into account.

According to the specification for testing polymer melts (ISO 6721-10), the recommended limit of the LVE range is the strain value at which a difference of 5% occurred in the values of any of the parameters shear complex modulus, G^*, storage modulus, G', or loss modulus, G'', compared with their values in the LVE range (Mezger, 2006). This rule is also recommended for soft tissues.

Deformation behaviour outside the LVE range is referred to as non-linear. It can be analysed only approximately, and in that case, further calculations have to be performed, e.g., via differential equations with several additional parameters which have to be preset by the user, based on assumptions. For this reason, rheological analysis is usually carried out using test data only within the LVE range.

Frequency Sweep

Frequency Sweeps (FS) are oscillatory tests performed at variable frequencies, keeping a constant strain amplitude. They are used to study time-dependent shear behaviour since the frequency is the inverse value of time. Short-term behaviour is simulated by rapid motion (high frequencies) and long-term behaviour by slow motion (low frequencies).

Controlled Shear Rate (CSR)

In a Controlled Shear Rate (CSR) test, shear rate is imposed and shear stress is measured. There are two ways to perform a CSR test.

On the one hand, if shear rate varies, flow and viscosity curves are obtained. To avoid transient effects, the duration of the measuring point should be at least as long as the value of the reciprocal shear rate ($1/\dot{\gamma}$) (Mezger, 2006). The viscosity function obtained from this test determines if a material shows or not a yield point.

On the other hand, if a constant shear rate is applied, time-dependency of the material is obtained. To study shear behaviour as a function of time, constant shear rate or constant shear stress can be applied. If we apply a constant shear rate, we obtain stress and viscosity as functions of time. $\tau(t)$ and $\eta(t)$ curves are similar, because τ and η are proportional, since $\tau = \eta\dot{\gamma}$, here with $\dot{\gamma}$ = constant. When preseting low shear rates or shear stresses, the duration for each single measuring point must be long enough, otherwise transient effects are obtained.

Creep Test

In the creep test, a constant stress is suddenly applied to the material and the strain is observed over time. When a constant stress τ_0 is applied, the compliance at time t is given by $J(t) = \gamma(t)/\tau_0$, where $\gamma(t)$ is the shear strain at time t. The compliance is the reciprocal value of the shear modulus.

In viscoelastic materials, the elastic behaviour occurs with a certain time delay. To evaluate this time-dependent deformation behaviour, two parameters are used: the relaxation time and the retardation time. Relaxation time is used for tests when presetting the strain or strain rate, e.g. when performing relaxation tests. And retardation time is used for tests when presetting the stress, e.g. when performing creep tests. Retardation is the delayed response to an applied force or stress and it can be descibed as *delay of the elasticity.*

In the linear region, the applied stress is small and the creep/recovery response is independent of the applied stress. In the non-linear region, there is a break-down of structure and the response varies with the applied shear stress.

Previously, the creep test was the only way to produce very low shear rates. Today, however, when performing CSR tests with modern rheometers, measurements even in the low-shear range are possible when presseting very low-values by tests with direct speed control (Mezger, 2006).

Relaxation Test

Relaxation tests are used to analyse the viscoelastic behaviour performing a strain step. The relaxation time shows how fast the material dissipates stress after receiving sudden deformation and it can be used to characterise the elastic and viscous parts of the behaviour of a material. The stress relaxation modulus is calculated as the ratio of measured stress and applied strain, $G(t) = \tau(t)/\gamma_0$.

In linear viscoelasticity, the relaxation and creep functions are a function only of time. In non-linear viscoelasticity, the relaxation and creep functions are a function of both time and stress or strain. Within the non-linear viscoelasticity, it can be assumed quasi-linear viscoelasticity (QLV). This assumption establishes that strain and time effects are separable. Therefore, the relaxation modulus can be described by the product of two functions, one of strain only, the other of time only, i.e., $S = \xi(\gamma)G(t)$. This fact means that relaxation curves would be perfectly parallel, since the temporal response would be unaffected by changes in strain magnitude, and the strain function would be a scaling function for the linear viscoelastic relaxation modulus, $G(t)$ (Bilston, Liu, et al., 2001).

3.2.3 Application of the methodology to the characterisation of an agar gel

In order to validate the methodology, tests were performed in a synthetic material. In that way, the material is more available, it is more controlable and it has less variability than biological samples. An agar gel is selected for this purpose. Agar is a biological polymer, frequently used in tissue engineering research; due to its consistency, controllable size, and concentration-based properties, it often serves as a representative material for actual biological tissues (Nayar, Weiland, et al., 2012). A concentration of 3% was selected for the gel, because it was more robust and repeatable than gels created with smaller concentrations.

The agar gel was prepared with Agar (Fluka) from Sigma-Aldrich. The gel was prepared mixing 3% Agar and Milli-Q water in a glass beaker. The mixture was stirred at 580 rpm, 85°C, using a magnetic hot-stirrer in order to get a homogeneous mixture. Samples were stored at room temperature until gelification. Cylindrical samples were cut (25 mm diameter and approximately 2 mm height) and were placed between the parallel plates of the rheometer. The sample was irrigated with phosphate buffered saline (PBS) to prevent dehydration during testing. The top plate of the rheometer was lowered until it contacted the upper surface of the specimen. All measurements were performed at 20°C.

Next, different tests presented in the methodology (Figure 3.3) were carried out, in order to determine the mechanical properties of the agar gel.

Amplitude test

A strain ramp was imposed from 0.001% to 10% at 1 Hz. Figure 3.4 shows the results.

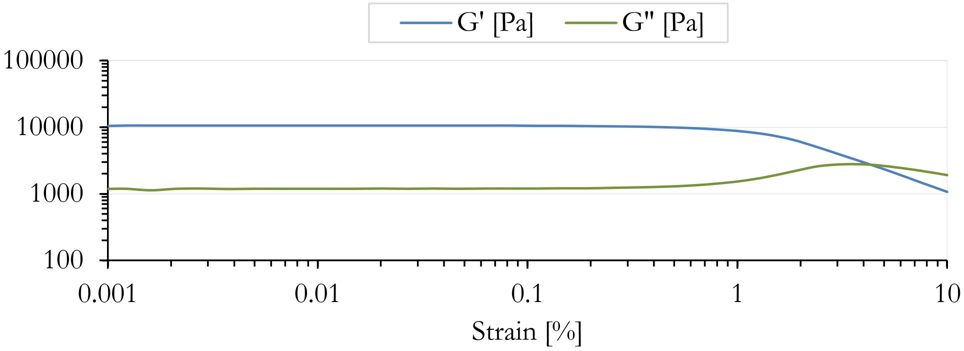

Figure 3.4: Amplitude sweep of 3% agar gel at 1 Hz.

The sample has a viscoelastic solid or gel character in the LVE range, since $G' > G''$ and $45° > \delta > 0°$. Following the specification for testing polymer melts (ISO 6721-10), explained in Section 3.2.2, the limit of LVE range is $\gamma_L = 0.45\%$, being the yield stress $\tau_y = 45.3$ Pa. Flow point occurs at a strain of 4.3%, at $\tau_f = 167$ Pa. Beyond this point the sample is not a viscoelastic solid anymore, and it begins to have a viscoelastic liquid behaviour.

Frequency Sweep

A frequency sweep was performed from 0.16 to 16 Hz at 0.3% strain, being the deformation inside the LVE range. Figure 3.5 shows the result of this test.

An increase of the storage and loss moduli with frequency can be observed.

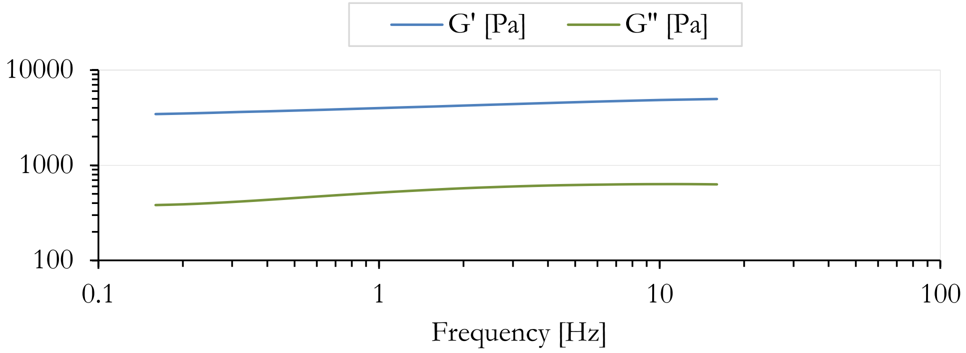

Figure 3.5: Frequency sweep of 3% agar gel at 0.3% strain.

Controlled Shear Rate (CSR) tests

Viscosity function and flow curve

As it has been explained in Section 3.2.2, when shear rate varies, viscosity and flow curves are obtained. With this aim, shear rate was varied from 0.01 to 0.8 s^{-1}. At higher strain rates, migration of the plate was observed. Figures 3.6 and 3.7 show viscosity and flow functions obtained from the agar gel, respectively.

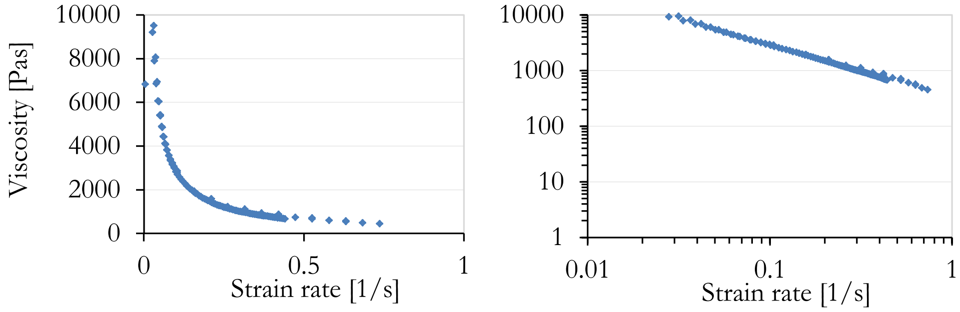

Figure 3.6: Viscosity function of agar gel represented on arithmetic scale (left) and logarithmic scale (right).

Comparing these experimental curves with the theorical ones presented in Section 2.1.2, several behaviours are observed. Comparing the viscosity function of the agar gel in logaritmic form (Figure 3.6 right) with the

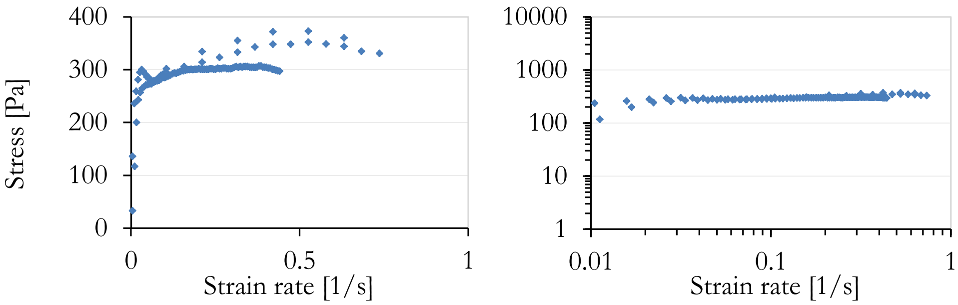

Figure 3.7: Flow curve of agar gel represented on arithmetic scale (left) and logarithmic scale (right).

theoretical one (Figure 2.7), it can be observed that the tested gel does not show a zero-shear viscosity, and therefore, it shows a yield point. This fact is in agreement with the results obtained from the amplitude sweep.

If viscosity and flow curves are compared with Figure 2.5, shear-thinning behaviour is observed, since viscosity function decresases with shear rate, and stress increases concavely with the strain rate.

Time dependence

As it has been explained in Section 3.2.2, a constant shear rate can be applied in order to study the shear behaviour as a function of time. In this case, constant shear rate was applied to analyse the effect of time on the viscosity. Different shear rates of 0.001, 0.005, 0.01 and 0.05 s^{-1} were applied. Figure 3.8 shows time-dependent shear stress and viscosity curves. It can be seen that the stress and viscosity functions are similar when a constant shear rate is applied, i.e., they have similar shape. Comparing Figure 3.8 with Figure 2.6, it can be observed that the gel has not rheopectic neither thixotropic behaviour, since stress and viscosity seem to remain constant with time. The increase of stress or viscosity showed by some curves at the beginning can be due to transient effects. After that, the effect of the time is considered negligible.

Other way to see this, is given by Figure 3.9, that shows viscosity curve at different strain rates. Viscosity can be considered independent of time, because the dependence on the strain rate prevails over the dependence on time.

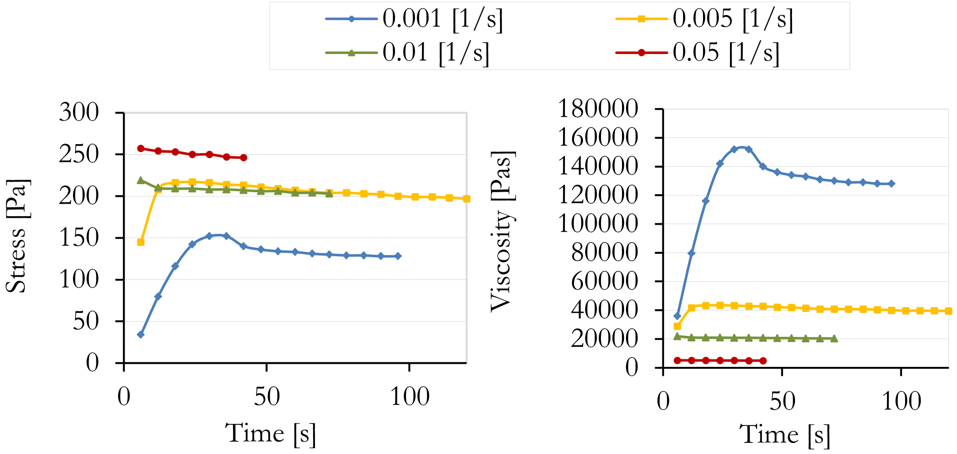

Figure 3.8: Time-dependent shear stress curve (left) and viscosity curve (right) of 3% agar gel.

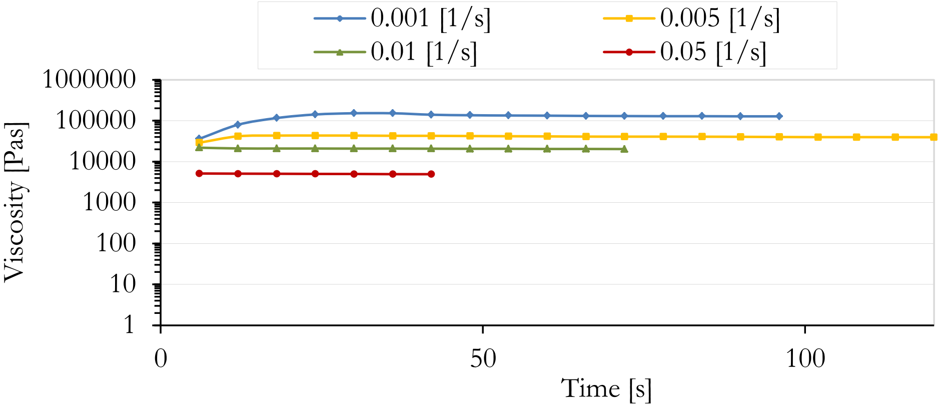

Figure 3.9: Viscosity functions of 3% agar gel at different shear rates.

When strain rate varies, and flow and viscosity curves are obtained as function of shear rate, the material can be classified as shear-thickening or shear-thinning. Similarly, when constant shear rate is imposed and viscosity is represented as function of time, material can be classified as rheopectic and thixotropic. However, these classifications are more valid for fluids than for solids. This thesis is focused on viscoelastic solids, and for solids, the interesting response to be analysed is the strain-stress curve. However, when flow and viscosity curves are presented as function of shear rate or as function of time, the reached strain is not controlled. As a result, in this kind of experiments, the achieved strain is too high, exceeding values of more than 100% in few seconds. This fact entails the risk of sliding and migration of the sample. Therefore, from here, as it will be seen in Section 3.3 for the porcine brain tissue, the viscosity is analysed observing how strain-stress curve changes when strain rate varies, instead of obtaining viscosity curves.

Creep test

Creep tests were performed applying a stress step of 40 Pa, which is within LVE range. Figure 3.10 shows the applied stress (above) and the measured strain (below).

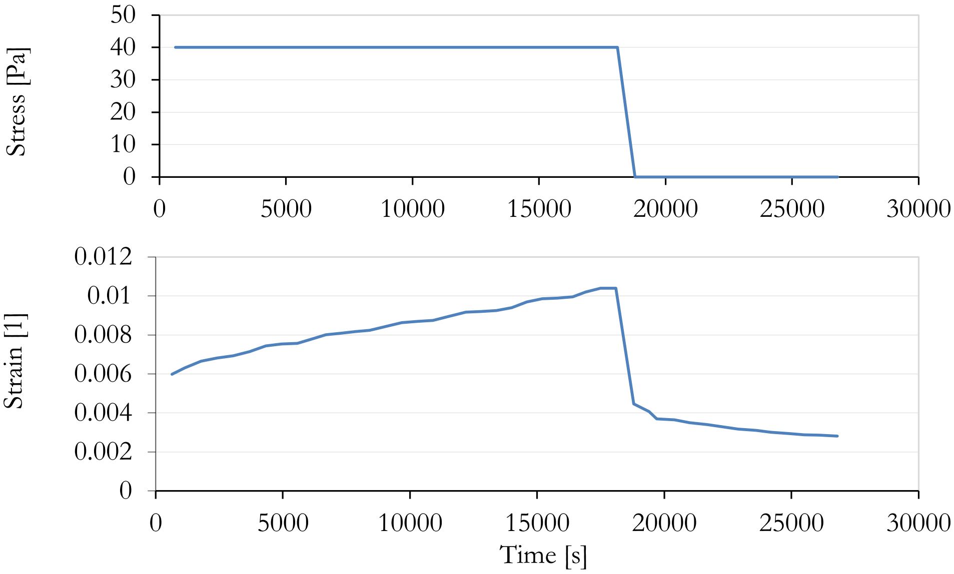

Figure 3.10: Creep function of the 3% agar gel. Input (above): stress pulse of 40 Pa. Output (below): strain versus time.

Regarding the strain response, there is no immediate deformation when applying a stress pulse, and it shows a delay reaching the maximum strain. The same happens in the recovery phase: the material has a reformation, but not immediately. In conclusion, regarding the response of creep test, the viscoelastic solid behaviour of the agar gel can be observed.

Relaxation test

Figure 3.11 shows stress relaxation test performed at 0.4% strain, which is within LVE range. The figure shows the imposed strain of 0.4% (above) and the corresponding shear stress (below).

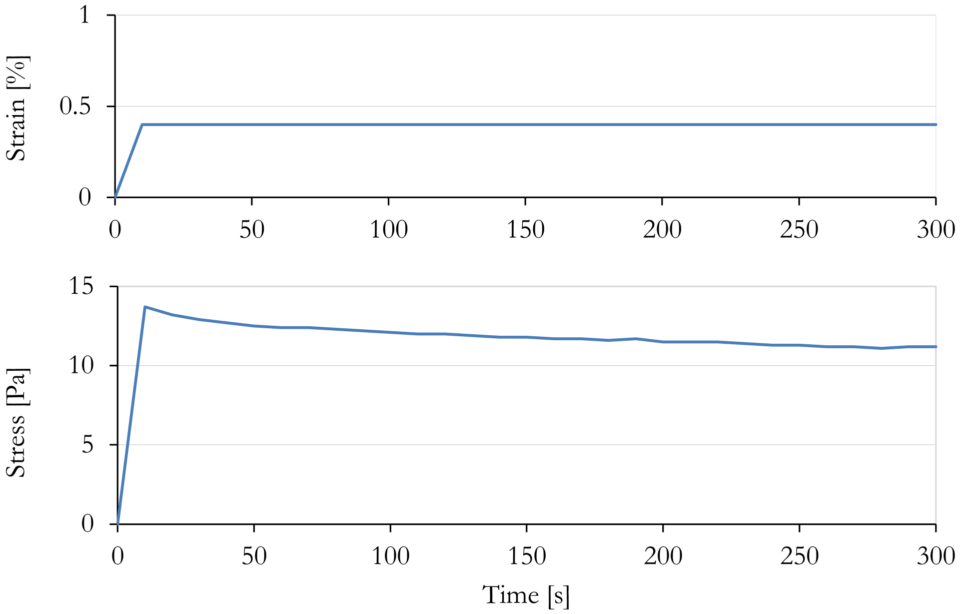

Figure 3.11: Relax function of 3% agar gel. The input (above): strain pulse of 0.4%. Output (below): stress versus time.

Similarly to the creep test, in relaxation test, the viscoelastic behaviour of the agar gel is oberved. Comparing to the Figure 2.10, it can be seen how the stress is relaxing to a certain extent only.

Different relaxation tests were performed applying different constant strain steps. Figure 3.12 shows the relaxation modulus obtained from each relaxation test.

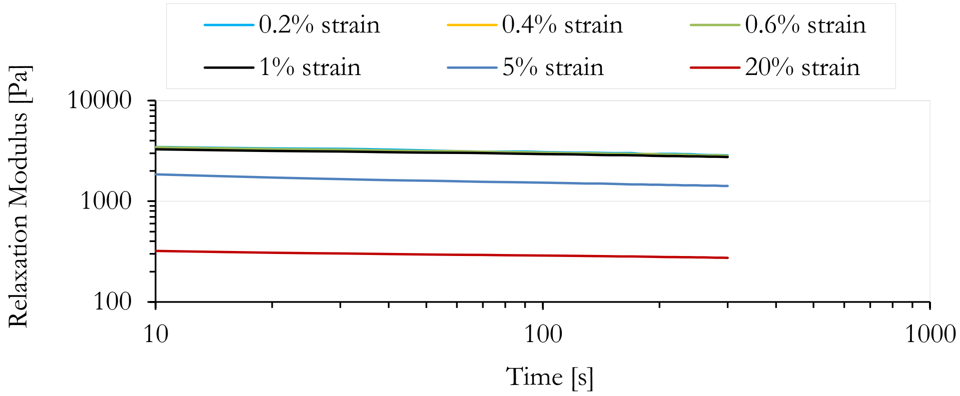

Figure 3.12: Relaxation test of 3% agar gel at different strain steps.

The $G(t)$ curves essentially overlap with one another, independent of the preset strain, γ_0, as long as the limit of the LVE range is not exceeded, or it is not exceeded considerably (Mezger, 2006). Those $G(t)$-curves, which are not overlapping with one another but deviate significantly downwards, have obviously been measured under conditions outside the LVE range, that is what happens with the curves of 5% and 20%. Therefore, under these conditions, material can be considered linear viscoelastic for strains smaller than 1%.

Using an analysis tool, various rheological parameters of viscoelastic functions might be calculated mutual from each other. Computer programs, numerical methods and the corresponding algorithms are available for these calculations, enabling the user to convert data of relaxation test, creep test and oscillatory tests, e.g. from $G(t)$ into G' and $G''(f)$ or from $J(t)$ into G' and $G''(f)$, or vice versa (Mezger, 2006).

Park and Schapery (1999), for example, presented a numerical method of interconversion between compliance (creep test) and relaxation modulus (relaxation test). Although it is possible to convert data from one experimental test to other, it is not simple, and, therefore, it can be easier and less time consuming to perform all the tests that are required to develop a model.

3.3 Experimental testing of Porcine Brain Tissue

Once the methodology is tested and the tests are known, the methodology is applied to biological tissue. Porcine brain tissue is chosen as a substitute for the human brain tissue due to its availability. The differences between human and animal brains are often considered relatively small, which enables animal brains to be a good substitute for human brains (Hrapko, Van Dommelen, et al., 2008b).

3.3.1 Testing of porcine brain tissue

Samples preparation

Brains were collected from 7 to 8 month-old pigs (at this age, the tissue is considered to possess a fully developed micro-structure (Hrapko, Van Dommelen, et al., 2008a)) in a local slaughterhouse, 24 hours post mortem. Brains were refrigerated before being collected and preserved later in a solution of phosphate buffered saline (PBS) at 4°C, to slow down their degradation and dehydration. Testing was then completed within one or two days. In the literature, the postmortem time of the samples can vary from only few hours (Arbogast and Margulies, 1998) to several days (Darvish and Crandall, 2001).

Cylindrical probes were cut from the brain parenchyma (Diameter: 25 mm. Height: 2 - 4 mm). No distinction was made between the properties of grey and white matter. Brain was considered isotropic and no difference was made between different functional brain regions.

A parallel-plate rheometer was used to carry out the rheological tests. Temperature was considered constant at 37°C in all experiments.

Amplitude Sweep

An Amplitude Sweep (AS) was done to determine the LVE limit of the brain tissue. A strain ramp was imposed from 0,001% to 100%, at 1 Hz.

Frequency Sweep

A Frequency Sweep (FS) was performed to determine the strain rate effect on the brain tissue. A strain of 1% was established (within the linear viscoelastic range) over a frequency range of 0.1 - 20 Hz.

Controlled Shear Rate (CSR) tests

Due to the moderate and slow strain rates relevant to surgical procedures, rotational tests at slow shear rates were performed. Constant shear rate tests were carried out at 0.001, 0.01, 0.05 and 0.1 s^{-1} for strains up to 50%.

Creep-Recovery tests

Creep and relaxation tests are performed in order to model the viscoelastic behaviour of the tissue. The parametrization of some viscoelastic models is more complicated with creep data than with relaxation data. For example, there is no known closed form for the creep compliance in terms of the coefficients of the Prony series, a mathematical serie that is used in quasi-linear viscoelastic modelling. That is why, for porcine brain tissue, viscoelastic behaviour is analised by relaxation tests.

Nonetheless, two creep-recovery tests are perfomed, at 5 Pa and at 10 Pa.

Stress Relaxation tests

Relaxation tests are performed to analyse the viscoelastic behaviour performing a deformation step. Different relaxation tests were performed applying constant strain steps of 1%, 10%, 20% and 40%.

3.3.2 Experimental results

Amplitude Sweep

Figure 3.13 presents the results of an amplitude sweep at 1Hz. The average values and the standard deviation of G' and G'' of the tested samples are presented. Following the recommendation of the 5% described in Section 3.2.2, the obtained limit of LVE range is $\gamma_L = 1.5\%$ (being the yield stress, $\tau_y = 4.5$ Pa). The tissue has a viscoelastic solid character in the LVE range, since $G' > G''$. Flow point occurs approximately at a strain of 100%. Outside this point the brain tissue is not a viscoelastic solid anymore and it begins to have a viscoelastic liquid behaviour.

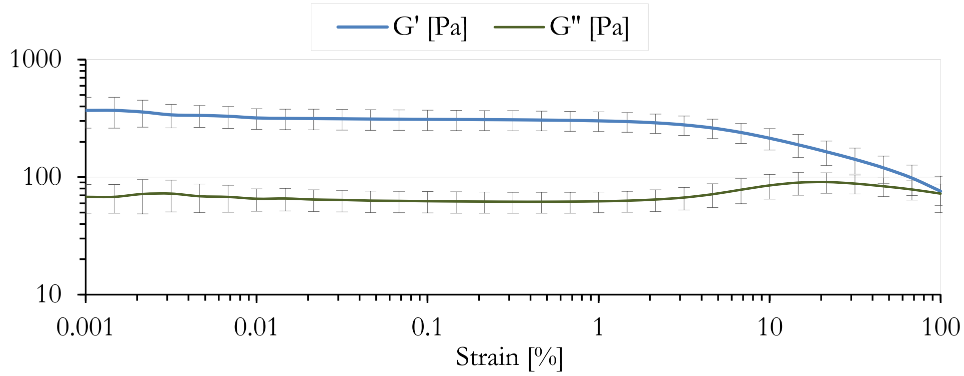

Figure 3.13: Amplitude sweep at 1 Hz. The mean value and standard deviation of 17 samples from 3 brains are represented.

These results determine that LVE range is around 1% strain, which is in the range established in the literature (Brands, Bovendeerd, et al., 1999; Nicolle, Lounis, et al., 2005).

Frequency Sweep

Figure 3.14 shows the average values and the standard deviation of frequency sweep done at 1% strain. The storage and loss moduli at frequencies from 0.1 to 20 Hz vary from 144.6 ± 18.6 to 234.6 ± 71.2 Pa and from 31.3 ± 5.3

to 117.8 ± 28.8 Pa respectively.

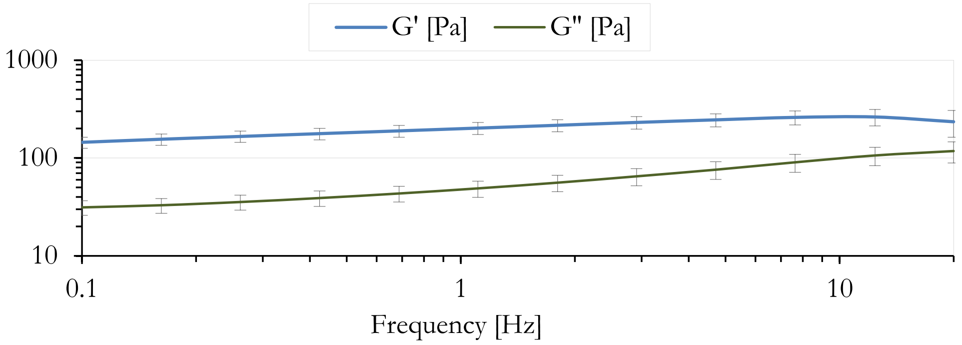

Figure 3.14: Frequency sweep at 1% strain. The mean value and standard deviation of 11 samples from 2 brains are represented.

In comparison with the literature, the experimental values of G' and G'' are lower than those obtained by Hrapko, Van Dommelen, et al. (2006). This can be due to several factors. The main differences between both works, are that the authors used eccentric configuration and they applied a preconditioning to the tissue. The differences on the values can also be due to the differences between the tested species or samples.

Moreover, from the frequency sweep, an increase in the shear moduli with increasing frequency is observed. This fact agrees with the literature (Hrapko, Van Dommelen, et al., 2006, 2008b; Nicolle, Lounis, et al., 2005).

Controlled Shear Rate (CSR) tests

Figure 3.15 presents the average values and the standard deviation of the stress values obtained at different constant shear rates. It can be observed that there is a strong dispersion between values from one sample to another. However, the tissue dependency on the strain rate is observed, increasing the resultant stress with increasing strain rate. This fact agrees with Bilston, Liu, et al. (2001) and Hrapko, Van Dommelen, et al. (2006). The stress obtained experimentally in CSR tests has lower values than those obtained in the literature. The differences with Hrapko, Van Dommelen, et al. (2006) can

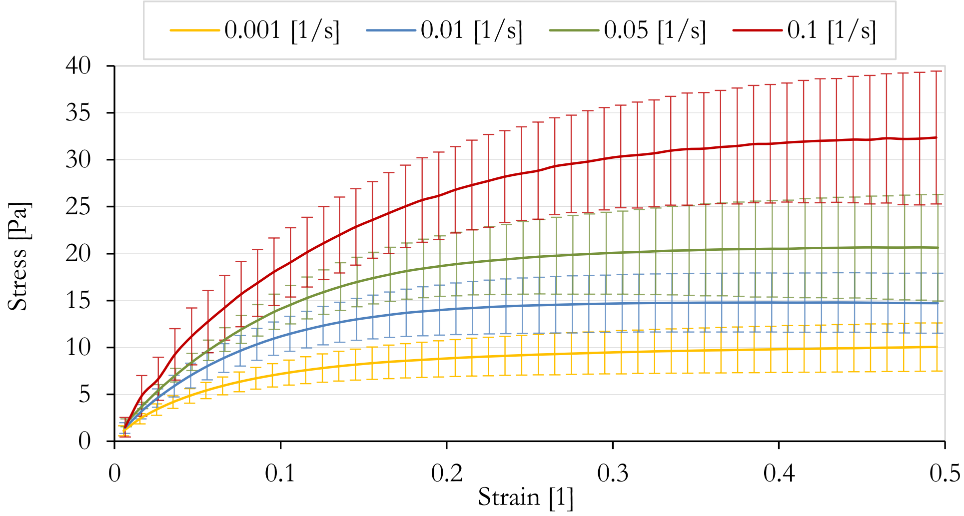

Figure 3.15: CSR at 0.005, 0.01, 0.05 and 0.1 s^{-1}. The average value and the standard deviation of each CSR test is represented. 6 samples from two brains have been tested at 0.001 s^{-1}, 14 samples from four brains at 0.005 s^{-1}, 12 samples from five brains at 0.01 s^{-1}, 7 samples from two brains at 0.05 s^{-1} and 6 samples from one brain at 0.1 s^{-1}.

be due to several aspects, such as the preconditioning of the tissue, the differences between the tested species or samples. Apart from that factors, comparing with Bilston, Liu, et al. (2001), it should be noted that the authors performed similar experiments in a parallel plate rheometer, but to bovine, not porcine, brain tissue, applying a preconditioning to the samples.

Creep-Recovery Test

Figure 3.16 shows the response of one sample under the creep test performed at 5 Pa (within the limit of LVE range) and 10 Pa (out of LVE range). It can be clearly observed a delayed but complete reformation of the strain when the stress pulse is removed, showing the viscoelastic behaviour of the tissue.

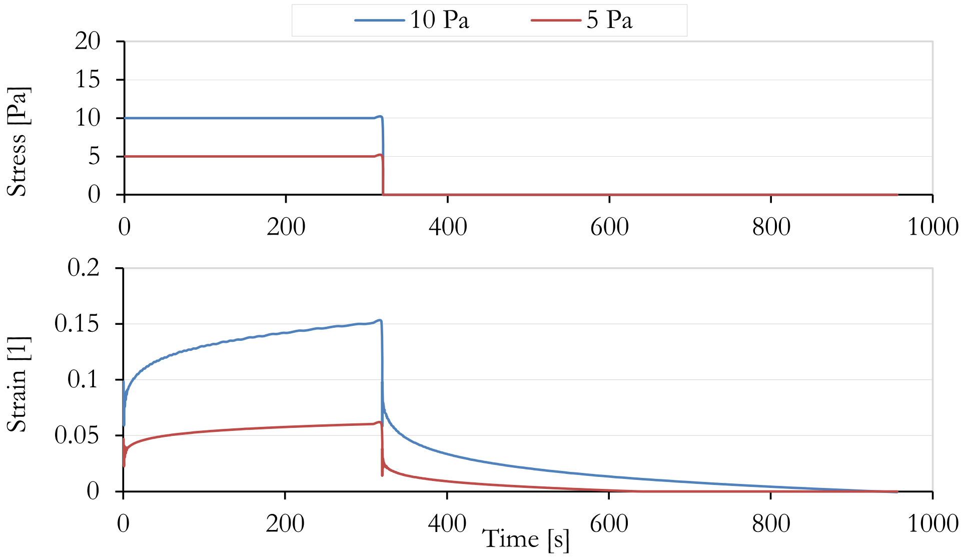

Figure 3.16: Creep and recovery test of porcine brain tissue at stress step of 5 Pa and 10 Pa.

Relaxation Test

Figure 3.17 shows the relaxation modulus obtained for strain steps of 1%, 10%, 20% and 40%.

A decrease of the relaxation modulus with increasing strain was found in the stress relaxation measurements, which is in agreement with Bilston, Liu, et al. (2001) and Hrapko, Van Dommelen, et al. (2006).

As it has been explained in Section 3.2.2, in linear viscoelasticity, the relaxation function is a function only of time. Whereas, in non-linear viscoelasticity, the relaxation function depends on both time and strain. Figure 3.17 shows that for strains larger than 1%, the response of the material depends on the value of the strain, i.e. the material model has a non-linear viscoelastic behaviour. However, if the curves are considered mostly parallel, a quasi-linear viscoelasticity can be assumed.

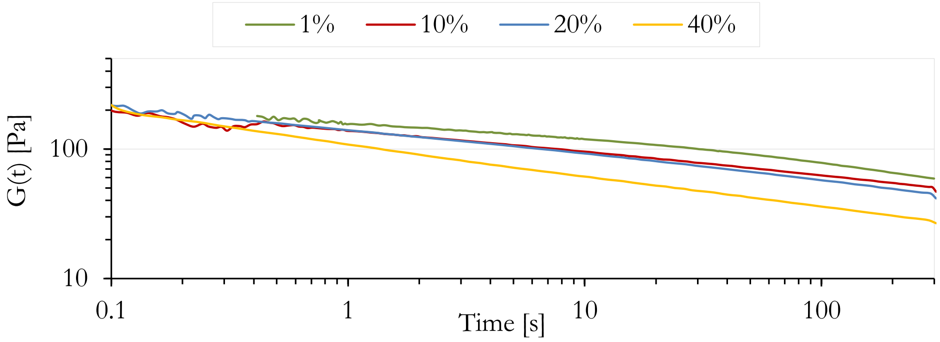

Figure 3.17: Relaxation tests at strain levels of 1%, 10%, 20% and 40%. The average values of relaxation modulus versus time is presented. 8 samples from two brains have been tested at 1% strain, 15 samples for two brains at 10% strain, 9 samples from two brains have been tested at 20% strain and 10 samples from two brains at 40% strain level.

3.3.3 Design of porcine brain tissue laboratory phantom - Comparison between gels and porcine brain tissue

For many applications, it can be interesting to develop a phantom whose mechanical properties are similar to those of the real brain tissue. Phantoms are very useful for the testing and calibration of machines, such as MRE and scanners. In addition, they are a good alternative to work, for performing experiments, since they are cleaner than real tissue, they do not involve biological risks and they do not have any ethical restriction. With this aim, this section makes a comparison between the different gels made in the laboratory with biological porcine brain tissue.

Research studies on brain phantom materials

Several research groups proposed a variety of suitable materials for gel preparation, with the purpose of building soft tissue phantoms. Some of the most recurrent materials which were successfully used are agar and gelatin based blends, described in (Madsen, Hobson, et al., 2005); carrageenan was successfully used in (Kato, Kuroda, et al., 2005) as an alternative to agar; a blend of mineral oil and SEBS copolymer was proposed in (Oudry, Bastard, et al., 2009), with accurate results and providing gels with long durability; polyacrylamide-based phantoms for elastography and imaging modalities (MRI, US) are commercially available (CIRS Inc. Norfolk, Virginia, USA) and show excellent properties, though they seem fragile, complex and expensive compared with water-based phantoms (Kawabata, Waki, et al., 2004). Several combinations regarding other materials like, polyurethane (Campus and Engineering, 2005) or PVA Cryogels (Fromageau, Gennisson, et al., 2007) were used with less repercussion. In fact, experiments using a blend of PVA, pure water and ethanol homopolymer showed that the obtained phantom did not posses long-term stability and were significantly stiffer than biological soft tissue. Preparation of PVA or silicone gels is time consuming and costly and their sizes and shapes cannot be easily changed.

Propylene glycol-based phantoms were proposed in (Ohno, Kato, et al., 2008) as an alternative type of gel. This alternative has not been developed to its full extent despite the promising results obtained. Conventional materials were treated extensively in literature; in any case it is still necessary to explore new stable material blends which might be more finely adjustable and which can mimic better the mechanical properties of soft tissues.

Materials and Methods

Materials used for making gels were as follows: Agar, food-grade from Scharlab; Gelatin, from porcine skin; Poly Propylene Glycol (PPG) and Glutaraldehyde (GTA) from Sigma-Aldrich. Gels were prepared using Milli-Q water. Adequate proportion of water was poured in a glass beaker and components were added to the mixture and stirred at 580 rpm, 85°C, using a magnetic hot-stirrer in order to get a homogeneous mixture. GTA was added to the blend as temperature dropped to 36°C. On Table 3.1, different material blends used for making the gels are presented.

Mixtures were stored at room temperature until gelification. After the gelification, cylindrical samples were cut using the same geometry as for tissue samples. Gel samples were tested in the parallel plate rheometer at 20°C. Each sample was irrigated with PBS to prevent dehydration during testing.

Table 3.1: Gel samples made of different concentrations of gelatin, agar, Poly Propylene Glycol (PPG) and Glutaraldehyde (GTA).

Gel type	Gelatin [%]	Agar [%]	PPG [%]	GTA [%]
A	-	0.5, 0.75, 1	-	-
B	0.3	0.5	1	-
C	0.5	0.4	0.5	-
D	0.5	0.4	0.5	1

Results

In order to determine the values of the mechanical properties (G', G'') of gels and porcine brain tissue, amplitude sweeps were performed at 1 Hz. Figure 3.18 shows the experimental values of G' and G'' obtained for the biological tissue and for the agar gels (A-type gels). The experimental data of porcine brain tissue (17 samples of 3 brains) obtained from AS (1 Hz) in Section 3.3.2 is represented.

The results show that the agar gel which best approximates the behaviour of biological brain tissue is the gel with an agar concentration of 0.5%. This gel fits well the storage modulus of the porcine brain tissue, however, it understimates the loss modulus. An agar gel with higher concentration (see 0.75% agar gel) fits the value of the loss modulus, but it overestimates the value of the storage modulus. Consequently, to obtain a mechanical behaviour similar to that of the brain tissue, agar concentrations should be between 0.5% and 0.7%. Higher concentrations exhibit property values far from those of the biological tissue ($G' \approx 4000$ Pa, $G'' \approx 200$ Pa versus $G' \approx 500$ Pa, $G'' \approx 100$ Pa).

Results of 0.5% agar gel and porcine brain tissue are together presented

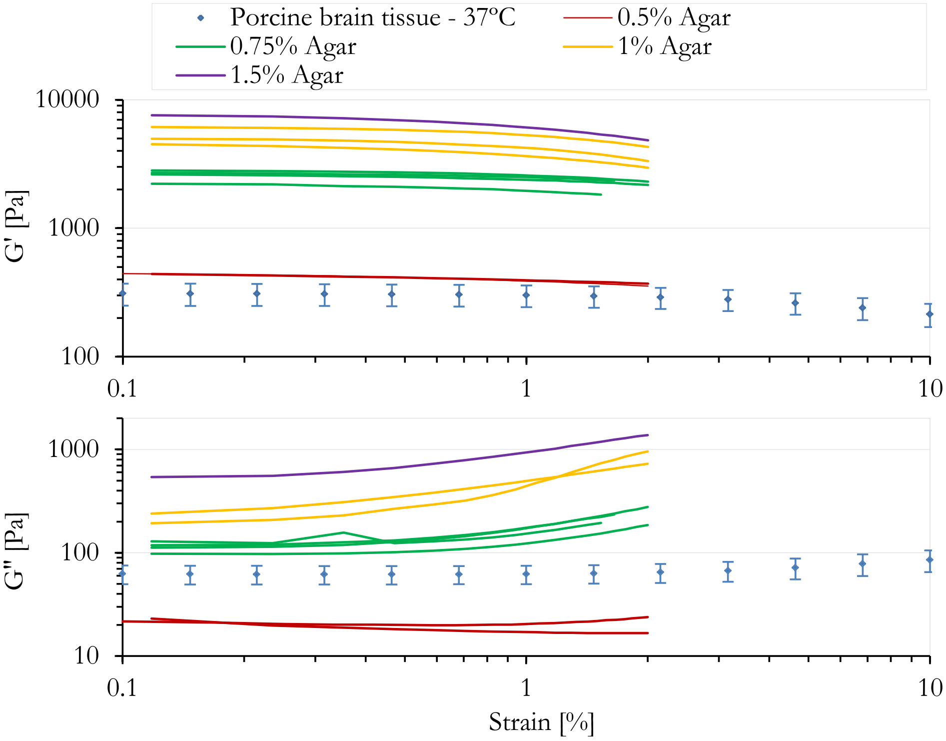

Figure 3.18: G' and G'' values of agar gels and porcine brain tissue obtained from the amplitude sweep at 1 Hz.

with the results of the other gels in Figure 3.19. In that case, 0.5% agar and B-type gel are those who better represent the mechanical behaviour of the porcine brain tissue. Other gels such as, C-type and D-type gels, approximate better the loss modulus of porcine brain tissue. However, gels with larger loss modulus, also have larger storage modulus, and they deviate more from the brain tissue behaviour.

As it has been concluded in (Mendizabal, Landeira, et al., 2012), for simplicity, a gel entirely made of agar can be more appropriate. It seems that other substances do not provide any advantage over agar from a mechanical point of view, since they do not increase G'' without increasing G'. However, the combination of other components like gelatin, PPG or GTA provides a greater range of variability to accurately simulate different soft tissues. Also,

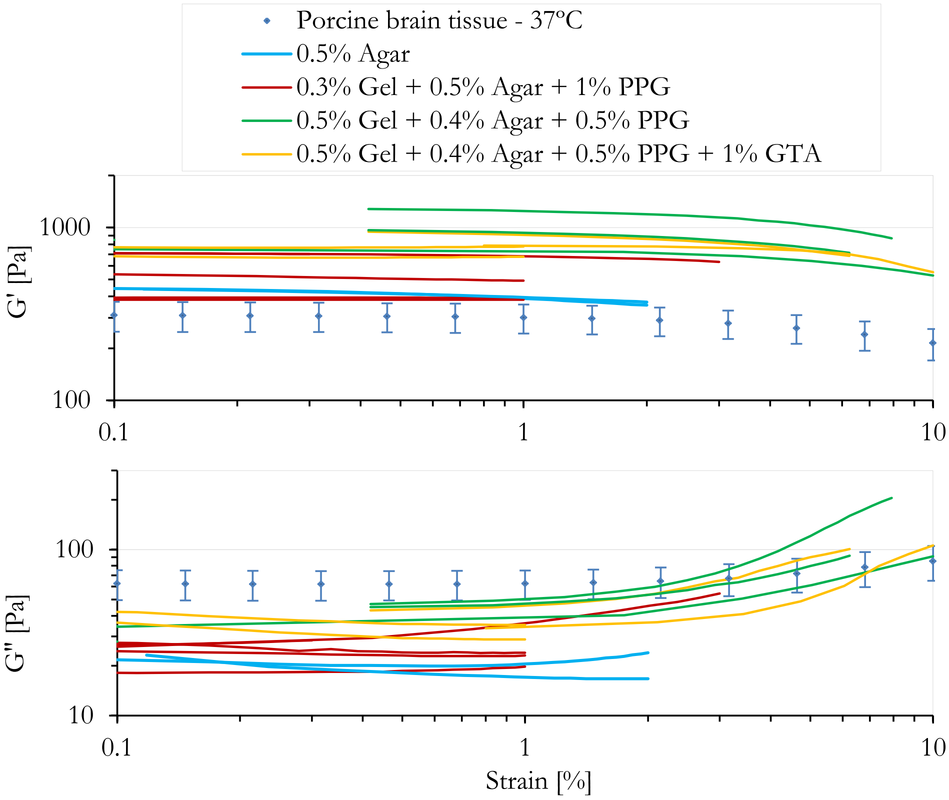

Figure 3.19: G' and G'' values of gels and porcine brain tissue obtained from the amplitude sweep at 1 Hz.

with these combinations different textures of the gel can be obtained getting more realistic gels.

3.4 Discussion

A methodology for the characterisation of biological soft tissues has been presented in this chapter. This methodology has been applied for the tissue characterisation at simple shear loads in a parallel plate rheometer.

Firstly, it is essential to perform an amplitude test to determine the LVE range of the material. It should be noted that scientifically, the deformation behaviour outside the LVE range can be analysed only approximately. As a consequence, rheological analysis is carried out using data within the LVE range. Secondly, a frequency test is recommended in order to see its influence on the mechanical properties of the material. In this work, oscillatory loads are assumed not to be common in surgical procedures. Therefore, the tissue is not characterised dynamically by frequency sweeps. However, it may be interesting for other oscillatory applications. Next, it is convenient to perform the constant shear rate tests. On the one hand, these tests show flow and viscosity curves of the tissue. They have been studied in the characterisation of the agar. However, the study of these curves is more appropriate to characterise fluids than solids. For that reason, in the characterisation of the brain tissue, the flow and viscosity curves have not been studied. On the other hand, CSR tests show strain-stress curve at a constant velocity. These curves have been studied for brain tissue at shear rates similar to those in surgical procedures (0.01 - 1 s^{-1}). It has been observed in the porcine brain tissue experimentation that the stress response increases with the strain rate. This fact is due to the viscoelastic behaviour of the tissue. Lastly, the creep and relaxation tests are presented.

The results presented for the porcine brain tissue characterisation are consistent with the literature, as it has been seen that the behaviour or pattern of brain tissue agrees with other studies in the literature. Although the experimental values obtained are lower than those found in the literature, they are of the same order of magnitude. However, it should be noted that some uncertainties can affect these results, since nowadays their effect is still not completely understood.

Dependence on the gap dimension of parallel plate rheometer can introduce some variability in the obtained results, since shear rate is dependent on the distance between the plates. Setting a larger distance, with the same rotational speed a lower shear rate is achieved. It should be taken into account that a larger shear gap causes the rheological conditions to change for the worse, since there is an increasing risk that the degree of inhomogeneous shear behaviour may grow (Mezger, 2006). However, the gap varies over a relatively narrow range (3±1 mm), therefore, this effect is considered negligible.

The possible variability in the geometry of the samples, such that the faces are not exactly parallel or that the sample is not exactly circular, can also introduce some variability in the results. However, the samples comply with the specifications defined by the testing machine. Besides, the upper plate descends until it makes a sufficient contact with the sample. Hence, it is considered that the variability that may occur is also negligible.

The same samples have been used in different tests. The possible effect of the previous load in the sample has not been taken into account. Some rotational tests have been repeated with the same samples, in order to find the repeatability or to find how this effect can influence. The stiffness has increased slightly or remained constant with the number of tests. It is not clear if these minor differences observed are caused by the previous load of the sample. They may be also due to dehydration of the sample during the test or to the contact between the plates and the sample, that can be slightly changed from one test to another. In any case, this effect seems to be insignificant in comparison with the variability between different samples.

Preconditioning is somewhat controversial for testing tissue samples, like brain tissue, which do not naturally experience cyclic loading. It is intended that the preconditioning redistributes the mobile fluid throughout the tissue sample, thus giving a more consistent response, and less inter-sample variability due to this fluid distribution. Some investigators have used preconditioning, and others have not, and it is not completely clear which is the best option (Bilston, Liu, et al., 2001). In this study, samples have not been preconditioned, however, the tissue has not been submitted to cycling loads, which are those that appear to be the most influenced by the preloading.

CHAPTER 4

MODELS FOR TISSUE REPRESENTATION

Currently, there is no agreement in the literature in how to define the most suitable material models required for surgical simulation; different modellers may choose different models to describe the same phenomenon (Miller, Wittek, et al., 2010). Models for biological tissues must be simple enough to solve a broad range of problems, but complete enough to realistically describe the behaviour under a variety of load conditions (Kerdok, 2006). Due to the non-linearity of soft tissues and the large strains that occur in surgical procedures, it is reasonable to think that non-linear models (e.g. hyperelastic models, non-linear viscoelastic models) will be the most accurate ones to model these tissues. However, to reach a real time simulation, computation speed is an important factor to take into account in surgery simulation, and consequently, simplified linear models are frequently used.

The most appropriate model to represent the real tissue depends on the application where it is used. Advances in mechanical property characterisation of the brain tissue revealed that the material model used in brain impact analysis cannot be directly used in medical or surgical applications due to the strain-rate dependency (Chunping, 2007). Applications can be classified depending on this (Kyriacou, Mohamed, et al., 2002), as high strain-rate or quasi-static processes.

High strain-rate processes can be classified as high strain rates (from 10^2 to 10^4 s^{-1}), very high strain rates (from 10^4 to 10^6 s^{-1}) and ultra high strain rates ($> 10^6$ s^{-1}). High strain-rate processes in general, can be also classified into two main groups: Falls or car accidents, that happen at low strains and high frequencies and ballistic injuries, that happen at high strains and high frequencies. For impacts corresponding to typical velocities from defense-related terminal ballistics (1-2 km/s approximately), the peak strain rates developed are of the order of 10^5 - 10^6 s^{-1}.

Quasi-static (or low strain-rate) processes are slow enough processes for the inertia (i.e. mass acceleration) term to be negligible, for example when strain rates are slower than 0.1 s^{-1}. However, strain rate is still included for calculating stresses in the viscoelastic constitutive relation. Processes as neurological retraction, brain shift during surgery, hematomas, hydrocephalus, etc. are considered quasi-static processes.

During surgical procedures, strain rates are usually relatively small and it can be stated that surgical instruments have relatively slow motions (Brown, Sorkin, et al., 2002). Therefore, surgical simulation can be defined as a quasi-static process. Gao, Tay, et al. (2006) for example, considered brain deformation during surgery a relatively slow process (0.01 - 1 s^{-1}) with negligible dynamic components. One may argue that in such case, strain rate dependency is unlikely to play a major role. If the strain rate dependency is not of interest, the viscoelastic terms can be deleted from the hyper-viscoelastic model, which yields the hyperelastic model (Wittek, Hawkins, et al., 2009). Skrinjar, Nabavi, et al. (2002) for example, affirm that intraoperative brain deformation is a relatively slow process with negligible dynamic components, thus, the authors justify the use of a static model.

In this sense, this chapter aims to define realistic mathematical models for simulation of surgical procedures. Section 4.1 presents the state of the art of the modelling of biological soft tissues for surgical simulations. Section 4.2 describes the constitutive equations of different models. Elasticity, viscosity and viscoelasticity are described from a mathematical point of view. Section 4.3 introduces the modelling of the agar gel and the porcine brain tissue tested in Chapter 3.

4.1 State of the Art

This section presents the purely elastic (linear elastic and hyperelastic) models, as well as the viscoelastic models presented in the literature for the modelling of soft tissues.

Linear Elastic models

Linear elasticity-based FE models are probably the most widely used techniques to model tissue under infinitesimal deformations in surgical simulators. Linear FEM models are commonly used for the modelling of deformable materials, mainly because the equations remain simple and the computation can be optimized. Several authors used linear elasticity to model brain deformations (Clatz, Delingette, et al., 2007; Ferrant, Warfield, et al., 2001; Skrinjar, Nabavi, et al., 2002; Warfield, Talos, et al., 2001), considering that brain deformation is small, relative to the brain size and that it is a relatively slow process with negligible dynamic components.

The main limitation of the linear model is that it is not invariant with respect to rotations. When the object undergoes a rotation, the elastic energy increases, leading to a variation of volume. To adress this problem, the co-rotational approach was introduced (Felippa and Haugen, 2005). This model was used for liver modelling (Haouchine, Dequidt, et al., 2013) or for laparoscopic surgery simulation (Peterlík, Duriez, et al., 2012).

Hyperelastic models

Simulations built upon linear elastic models can only be applied to small strains, while most surgical procedures involve organs being subjected to large ones. The boundary between small and large deformations varies from 1 - 2% (Misra, Ramesh, et al., 2010) to 10% (Chunping, 2007; Picinbono, Delingette, et al., 2003).

The deformation of most biological materials under large strains can be described by the theory of non-linear elasticity (e.g. hyperelastic models). Hyperelastic models were commonly used to simulate brain tissue (Kaster, Sack, et al., 2011), liver tissue (Gao, Lister, et al., 2010; Picinbono, Delingette, et al., 2003), skin (Lapeer, Gasson, et al., 2011), for laparoscopic simulation (Székely, Brechbühler, et al., 2000) or to simulate soft tissues in general (Martins, Natal Jorge, et al., 2006).

Viscoelastic Models

Linear viscoelastic models were used to model brain tissue (Yoshizawa, Okamoto, et al., 2005), liver tissue (Liu and Bilston, 2000; Sedef, Samur, et al., 2006), temporomandibular joint (Fernández Fernández, Lamela Rey, et al., 2007) or porcine cardiac tissue (Bronshtein, Au-Yeung, et al., 2013).

It is quite common to assume a quasi-linear viscoelastic model for surgical simulations. Several authors used this approach to model porcine liver (Ahn and Kim, 2009; Kim and Srinivasan, 2005), porcine kidney (Kim and Srinivasan, 2005), human liver (Nava, Mazza, et al., 2008) or bovine brain (Laksari, Shafieian, et al., 2012).

Soft tissues in general are non-linearly viscoelastic materials, and the modulus is not strain-time separable, therefore a quasilinear model is not suitable (Bilston, Liu, et al., 2001). As a consequence, authors developed more complex non-linear viscoelastic models, considering the non-linearity between stress and strain, as well as between stress and strain rate. These non-linear models have been applied not only to brain tissue (Bilston, Liu, et al., 2001; Brands, Peters, et al., 2004; Hrapko, Van Dommelen, et al., 2006; Miller and Chinzei, 2002), but also to liver (Liu and Bilston, 2002), kidney (Nasseri, Bilston, et al., 2002), orbital connective tissue and fat (Yoo, Gupta, et al., 2011) or for cataract surgery simulation (Comas, Taylor, et al., 2008).

Nevertheless, the estimation of parameter values for the non-linear viscoelastic models can be complex and computationally expensive (Bilston, Liu, et al., 2001).

Although sophisticated tissue models have been developed in the past by the mechanics community, they are not always the best choice for their simulation, since their integration with medical simulators can be difficult due to real-time computation requirements (Basdogan, Ho, et al., 2001).

Liu and Bilston (2002) concluded that if accuracy of the obtained deformation is critical, a complex constitutive model may be required, while in other applications, where accuracy is less important than computational efficiency, a simpler constitutive model may be more appropriate. Wittek, Hawkins, et al. (2009) recommend using linear elastic constitutive model (and geometrically non-linear analysis) for the brain tissue, in the case of craniotomy-induced shift, as it saves computation time and causes no loss of accuracy as compared to a hyperviscoelastic model.

4.2 Mathematical models - Constitutive equations

This section presents different mathematical models: purely elastic models, viscosity models and viscoelastic models. Models are focused on simple shear loads, that are those that are present in the characterisation with the parallel plate rheometer. In Section 4.3 these models are used to model the agar gels and porcine brain tissue characterised in Chapter 3.

4.2.1 Elastic models

The theory of continuum mechanics (Section 2.2) is applied to the case of simple shear deformation mode. Being γ the shear deformation, deformations are as follows:

$$\begin{aligned} x_1 &= X_1 + \gamma X_2 \\ x_2 &= X_2 \\ x_3 &= X_3 \end{aligned} \tag{4.1}$$

Therefore, the deformation gradient tensor, **F**, in simple shear is:

$$\mathbf{F} = \frac{\partial \mathbf{x}}{\partial \mathbf{X}} = \begin{bmatrix} \frac{\partial x_1}{\partial X_1} & \frac{\partial x_1}{\partial X_2} & \frac{\partial x_1}{\partial X_3} \\ \frac{\partial x_2}{\partial X_1} & \frac{\partial x_2}{\partial X_2} & \frac{\partial x_2}{\partial X_3} \\ \frac{\partial x_3}{\partial X_1} & \frac{\partial x_3}{\partial X_2} & \frac{\partial x_3}{\partial X_3} \end{bmatrix} = \begin{bmatrix} 1 & \gamma & 0 \\ 0 & 1 & 0 \\ 0 & 0 & 1 \end{bmatrix} \tag{4.2}$$

The volume ratio, defined as $J = det(\mathbf{F})$, for simple shear load is $J = 1$, that means that simple shear is isochoric (volume preserving), i.e. compressibility it is not taken into account with simple shear test.

Left Cauchy-Green deformation tensor, **B**, is given by Equation (4.3):

$$\mathbf{B} = \mathbf{F}\mathbf{F}^T = \begin{bmatrix} \gamma^2 + 1 & \gamma & 0 \\ \gamma & 1 & 0 \\ 0 & 0 & 1 \end{bmatrix} \tag{4.3}$$

Invariants of **B** for a simple shear load are determined by Equation (4.4):

$$\begin{aligned} I_1 &= tr\mathbf{B} = \gamma^2 + 3 \\ I_2 &= \frac{1}{2}[(tr\mathbf{B})^2 - tr\mathbf{B}^2] = \gamma^2 + 3 \\ I_3 &= det\mathbf{B} = 1 \end{aligned} \tag{4.4}$$

Cauchy stress tensor for simple shear deformation is defined by Equation (4.5):

$$\boldsymbol{\sigma} = -p\mathbf{I} + 2\frac{\partial W}{\partial I_1}\mathbf{B} - 2\frac{\partial W}{\partial I_2}\mathbf{B}^{-1} \tag{4.5}$$

That can also be expressed as follows (Horgan and Murphy, 2009):

$$\sigma_{11} = -p + 2(\gamma^2 + 1)\frac{\partial W}{\partial I_1} - 2\frac{\partial W}{\partial I_2} \tag{4.6}$$

$$\sigma_{22} = -p + 2\frac{\partial W}{\partial I_1} - 2(\gamma^2 + 1)\frac{\partial W}{\partial I_2} \tag{4.7}$$

$$\sigma_{33} = -p + 2\frac{\partial W}{\partial I_1} - 2\frac{\partial W}{\partial I_2} \tag{4.8}$$

$$\sigma_{12} = 2\gamma\left(\frac{\partial W}{\partial I_1} + \frac{\partial W}{\partial I_2}\right) \tag{4.9}$$

p is the arbitrary hydrostatic pressure arising due to the incompressibility constraint. Since the considered simple shear deformation is homogeneous, the equilibrium equations in the absence of body forces are satisfied if and only if p is a constant. The value of this constant is usually determined by using appropriate boundary conditions.

Strain energy functions

There has been ample research into different forms of W that one may choose to describe a tissue. Below, some hyperelastic models are described.

Saint Venant-Kirchhoff model

The simplest hyperelastic material model is the Saint Venant-Kirchhoff model which is just an extension of the linear elastic material model to the non-linear regime. Strain energy density function for the Saint Venant-Kirchhoff model is given by Equation (4.10):

$$W(\mathbf{E}) = \frac{\lambda}{2}(tr(\mathbf{E}))^2 + \mu tr(\mathbf{E}^2) \tag{4.10}$$

with $\mathbf{E}$ being the Green-Lagrange infinitesimal deformation tensor and μ, λ the Lamé coefficients. These coefficients are related to Young's modulus, E, shear modulus, G, and Poisson's ratio, ν, by

$$\lambda = \frac{\nu E}{(1+\nu)(1-2\nu)} \tag{4.11}$$

$$\mu = G = \frac{E}{2(1-\nu)} \tag{4.12}$$

The first Piola-Kirchhoff stress in that case is,

$$\mathbf{P} = \mu(\mathbf{F} + \mathbf{F}^T - 2\mathbf{I}) + \lambda tr(\mathbf{F} - \mathbf{I})\mathbf{I} \tag{4.13}$$

The second Piola-Kirchhoff stress is,

$$\mathbf{S} = \frac{\partial W}{\partial \mathbf{E}} = \lambda tr(\mathbf{E})\mathbf{I} + 2\mu\mathbf{E} \tag{4.14}$$

This model is simple for its practical implementation, however, although it is suitable for large displacements, this model is not recommended for large strains.

Neo-Hookean

The incompressible Neo-Hookean model is defined by Equation (4.15):

$$W = \frac{\mu}{2}(I_1 - 3) \tag{4.15}$$

being μ the shear modulus of the material.

Replacing the Neo-Hookean strain energy function in the expression of simple shear stress (Equation (4.9)), simple shear stress is defined by Equation (4.16):

$$\sigma_{12} = \mu\gamma \tag{4.16}$$

Neo-Hookean is known to describe reasonably well the mechanical response of rubbery materials at small and moderate deformations. However, it is not valid to approach the gel or brain tissue behaviour at simple shear at large strains, since it has a linear response.

Mooney-Rivlin

Mooney-Rivlin strain energy function is:

$$W = C_{10}(I_1 - 3) + C_{01}(I_2 - 3) \tag{4.17}$$

where C_{01} and C_{10} are empirically determined material constants. For consistency with linear elasticity in the limit of small strains, the shear modulus is defined by $\mu = 2(C_{10} + C_{01})$.

Simple shear stress is defined by:

$$\sigma_{12} = 2(C_{10} + C_{01})\gamma \tag{4.18}$$

Equation (4.18) shows that Mooney-Rivlin model also has a linear response at simple shear, therefore it is not valid to approach the gel and brain tissue behaviour at large strains.

Ogden

Ogden strain energy function is postulated as a function of principal stretches $\lambda_1, \lambda_2, \lambda_3$ by Equation (4.19), (Holzapfel, 2000),

$$W = \sum_{i=1}^{N} \frac{\mu_i}{\alpha_i} (\lambda_1^{\alpha_i} + \lambda_2^{\alpha_i} + \lambda_3^{\alpha_i} - 3) \tag{4.19}$$

with

$$2\mu = \sum_{i=1}^{N} \mu_i \alpha_i \tag{4.20}$$

being μ the classical shear modulus in the reference configuration. In Equation (4.19), N is a positive integer which determines the number of terms in the strain-energy function, μ_i are shear moduli and α_i are dimensionless constants. Under the assumption of incompressibility, $\lambda_1\lambda_2\lambda_3 = 1$. Therefore, Ogden strain function can be writen as

$$W = \sum_{i=1}^{N} \frac{\mu_i}{\alpha_i} (\lambda_1^{\alpha_i} + \lambda_2^{\alpha_i} + \lambda_1^{-\alpha_i}\lambda_2^{-\alpha_i} - 3) \tag{4.21}$$

For one-term Ogden material, the strain energy function is:

$$W = \frac{\mu_1}{\alpha_1} (\lambda_1^{\alpha_1} + \lambda_2^{\alpha_1} + \lambda_3^{\alpha_1} - 3) \tag{4.22}$$

Cauchy stress in simple shear as a function of principal stretches is defined by Equation (4.23) (Horgan and Murphy, 2009):

$$\sigma_{12} = \frac{\lambda_1^2}{\lambda_1^2 + 1} \frac{\partial W}{\partial \lambda_1} - \frac{\lambda_2^2}{\lambda_2^2 + 1} \frac{\partial W}{\partial \lambda_2} \tag{4.23}$$

The principal stretches are related to shear deformation by Equation (4.24) (Horgan and Murphy, 2009),

$$\begin{aligned} \lambda_1 &= \frac{\gamma + \sqrt{4 + \gamma^2}}{2} \qquad (> 1) \\ \lambda_2 &= \frac{1}{\lambda_1} \\ \lambda_3 &= 1 \end{aligned} \tag{4.24}$$

Substituting the principal stretches (Equation (4.24)) and the strain energy function (Equation (4.22)) in Equation (4.23), the model can be fitted with experimental strain, γ.

Arruda Boyce

Strain energy function:

$$\begin{aligned} W = \mu\Big\{ & \frac{1}{2}(I_1 - 3) + \frac{1}{20\lambda_m^2}(I_1^2 - 9) + \frac{11}{1050\lambda_m^4}(I_1^3 - 27) \\ & + \frac{19}{7000\lambda_m^6}(I_1^4 - 81) + \frac{519}{673750\lambda_m^8}(I_1^5 - 243)\Big\} \end{aligned} \tag{4.25}$$

being μ and λ_m the parameters to be fitted. Substituting strain energy function in Equation (4.9), shear stress is obtained:

$$\sigma_{12} = 2\gamma\mu\left(\frac{\gamma^2+3}{10\lambda_m^2} + \frac{11(\gamma^2+3)^2}{350\lambda_m^4} + \frac{19(\gamma^2+3)^3}{1750\lambda_m^6} + \frac{519(\gamma^2+3)^4}{134750\lambda_m^8} + \frac{1}{2}\right) \tag{4.26}$$

Reordering Equation (4.26), a polynomial equation is obtained for simple shear stress:

$$\begin{aligned} \sigma_{12} = & \frac{67375\lambda_m^8 + 40425\lambda_m^6 + 38115\lambda_m^4 + 39501\lambda_m^2 + 42039}{67375\lambda_m^8}\mu\gamma \\ & + \frac{13475\lambda_m^6 + 25410\lambda_m^4 + 39501\lambda_m^2 + 56052}{67375\lambda_m^8}\mu\gamma^3 \\ & + \frac{4235\lambda_m^4 + 13167\lambda_m^2 + 28026}{67375\lambda_m^8}\mu\gamma^5 \\ & + \frac{1463\lambda_m^2 + 6228}{67375\lambda_m^8}\mu\gamma^7 + \\ & + \frac{519}{67375\lambda_m^8}\mu\gamma^9 \end{aligned} \tag{4.27}$$

This model seems to give the same result as reduced polynomial model of fifth order, but with more complex coefficients.

Polynomial models

The form of the polynomial strain energy potential for incompressible materials is given by Equation (4.28):

$$W = \sum_{i+j=1}^{N} C_{ij}(I_1 - 3)^i (I_2 - 3)^j \tag{4.28}$$

with C_{ij} material constants.

Simple shear stress for these models is given by:

- Polynomial order 2

$$\sigma_{12} = 2(C_{01} + C_{10})\gamma + 4(C_{11} + C_{02} + C_{20})\gamma^3 \tag{4.29}$$

- Polynomial order 3

$$\begin{aligned}\sigma_{12} &= 2(C_{01} + C_{10})\gamma + 4(C_{02} + C_{11} + C_{20})\gamma^3 \\ &\quad + 6(C_{03} + C_{12} + C_{21} + C_{30})\gamma^5\end{aligned} \tag{4.30}$$

Reduced Polynomial models

The form of the reduced polynomial strain energy potential for incompressible materials is given by Equation (4.31):

$$W = \sum_{i=1}^{N} C_{i0}(I_1 - 3)^i \tag{4.31}$$

being C_{i0} material constants.

Simple shear stress for these models is given by:

- Reduced Polynomial order 2

$$\sigma_{12} = 2C_{10}\gamma + 4C_{20}\gamma^3 \tag{4.32}$$

- Reduced Polynomial order 3

$$\sigma_{12} = 2C_{10}\gamma + 4C_{20}\gamma^3 + 6C_{30}\gamma^5 \tag{4.33}$$

- Reduced Polynomial order 4

$$\sigma_{12} = 2C_{10}\gamma + 4C_{20}\gamma^3 + 6C_{30}\gamma^5 + 8C_{40}\gamma^7 \tag{4.34}$$

- Reduced Polynomial order 5

$$\sigma_{12} = 2C_{10}\gamma + 4C_{20}\gamma^3 + 6C_{30}\gamma^5 + 8C_{40}\gamma^7 + 10C_{50}\gamma^9 \tag{4.35}$$

- Reduced Polynomial order 6

$$\sigma_{12} = 2C_{10}\gamma + 4C_{20}\gamma^3 + 6C_{30}\gamma^5 + 8C_{40}\gamma^7 + 10C_{50}\gamma^9 + 12C_{60}\gamma^{11} \tag{4.36}$$

In the case of simple shear loads, the polynomial models present no advantage over reduced polynomial models, since both result in the same equation.

Nunes model

Nunes (2011) proposed a strain energy to characterise a silicone rubber at simple shear load.

$$W = \frac{1}{2}(C_1(I-3) + C_2(I-3)^{3/4}) \tag{4.37}$$

where the invariants are $I_1 = I_2 = I$.

Simple shear stress is given by:

$$\sigma_{12} = 2C_1\gamma + \frac{3}{2}C_2\sqrt{\gamma} \tag{4.38}$$

To guarantee the necessary and sufficient conditions for the proposed strain energy function, i.e., to be strictly polyconvex, the relations $C_1 > 0$ and $C_2 > 0$ has to be taken into account.

Lopez-Pamies model

Lopez-Pamies (2010) proposed a new I_1-based hyperelastic model for rubber elastic solids applicable over the entire range of deformations.

$$W(I_1) = \sum_{r=1}^{M} \frac{3^{1-\alpha_r}}{2\alpha_r}\mu_r(I_1^{\alpha_r} - 3^{\alpha_r}) \tag{4.39}$$

the integer M denotes the number of terms included in the summation, while μ_r and α_r $(r = 1, 2, ..., M)$ are real-valued material parameters that need to be determined from experiments. The initial shear modulus is defined as $\mu = \sum_{r=1}^{M} \mu_r$.

- One term $(M = 1)$

$$W(I_1) = \frac{3^{1-\alpha_1}}{2\alpha_1}\mu_1(I_1^{\alpha_1} - 3^{\alpha_1}) \tag{4.40}$$

$$\sigma_{12} = \mu_1\gamma\left(\frac{\gamma^2+3}{3}\right)^{\alpha_1-1} \tag{4.41}$$

- Two terms $(M = 2)$

$$W(I_1) = \frac{3^{1-\alpha_1}}{2\alpha_1}\mu_1(I_1^{\alpha_1} - 3^{\alpha_1}) + \frac{3^{1-\alpha_2}}{2\alpha_2}\mu_2(I_1^{\alpha_2} - 3^{\alpha_2}) \tag{4.42}$$

$$\sigma_{12} = \frac{\gamma}{\gamma^2+3}\left(3^{1-\alpha_1}\mu_1(\gamma^2+3)^{\alpha_1} + 3^{1-\alpha_2}\mu_2(\gamma^2+3)^{\alpha_2}\right) \tag{4.43}$$

Amin model

Amin, Wiraguna, et al. (2006) developed an incompressible, hyperelastic model for high damping rubber. The authors define the strain energy function as:

$$\begin{aligned} W(I_1, I_2) = {} & C_5(I_1 - 3) + \frac{C_3}{N+1}(I_1 - 3)^{N+1} + \frac{C_4}{M+1}(I_1 - 3)^{M+1} \\ & + C_2(I_2 - 3) \end{aligned} \tag{4.44}$$

Substituting strain energy function in the Equation (4.9):

$$\sigma_{12} = 2\gamma(C_5 + C_2 + C_4\gamma^{2M} + C_3\gamma^{2N}) \tag{4.45}$$

Hyperelasticity parameters $(C_2, C_3, C_4, C_5, M, N)$ are identified using simple shear data, and minimizing least-square residuals. Simplifying the Equation (4.45):

$$\sigma_{12} = 2(C_5 + C_2)\gamma + 2C_4\gamma^{2M+1} + 2C_3\gamma^{2N+1}) \tag{4.46}$$

The coefficients of the Equation (4.46) are changed and are grouped for simplicity:

$$\begin{aligned} A_1 &= 2(C_5 + C_2) \\ A_2 &= 2C_4 \\ A_3 &= 2C_3 \\ B_1 &= 2M + 1 \\ B_2 &= 2N + 1 \end{aligned} \tag{4.47}$$

The simple shear stress can be written as:

$$\sigma_{12} = A_1\gamma + A_2\gamma^{B_1} + A_3\gamma^{B_2} \tag{4.48}$$

4.2.2 Viscous models

Viscosity curves and flow functions seen in Section 3.2.3 can be modelled by different equations. Some viscosity models are presented next.

- Newton's model for idealviscous flow behaviour:

  $$\tau = \eta\dot{\gamma} \tag{4.49}$$

  being τ the shear stress, η the viscosity and $\dot{\gamma}$ the shear rate.

  Other models describe the non-newtonian behaviour of fluids, for example:

- Ostwald/de Waele (or Power-Law):

  $$\tau = c\dot{\gamma}^p \tag{4.50}$$

  with the flow coefficient, c, and the exponent p. For shear thinning behaviour $p<1$, for shear thickening $p>1$ and for idealviscous flow $p=1$.

- Bingham:

  $$\tau = \tau_B + \eta_B\dot{\gamma} \tag{4.51}$$

  where τ_B is the *Bingham yield point* (which is the intersection of the *Bingham straight line* and the τ-axis) and η_B is the *Bingham viscosity.*

4.2.3 Viscoelastic models

Viscoelastic models incorporate both elastic and viscous models. Regarding the relation between stress and strain viscoelasticity can be classified in three groups: linear, quasi-linear and non-linear viscoelasticity. These groups are presented below.

4.2.3.1 Linear Viscoelastic models

Linear response means that stress is proportional to the strain, and thus, the modulus is independent of the strain, but it depends on time.

$$\sigma(t) = G(t)\gamma \tag{4.52}$$

The differential equations that describe linear viscoelasticity are linear and their coefficients are constant. These invariables of the material such as viscosity or elastic modulus remain constant when variables change. Because of these restrictions, the linear theory is applicable only when the changes in variables are small enough (Moreno Botella, 2005).

In that case, creep compliance is independent of stress and relaxation modulus is independent of strain. That means that, the creep compliance curves corresponding to different stresses or the relaxation modulus curves corresponding to different strains overlap. The creep compliance and relaxation modulus are empirically determined and describe the creep and stress relaxation behaviour of the viscoelastic material as a function of time.

The one-dimensional models of creep deformation and stress relaxation are respectively,

$$\epsilon(t) = \sigma_0 J(t) \tag{4.53}$$

$$\sigma(t) = \epsilon_0 G(t) \tag{4.54}$$

where $J(t)$ is the creep compliance for constant stress, σ_0, and $G(t)$ is the stress relaxation modulus for constant strain, ϵ_0.

There are several constitutive models for linear viscoelastic materials. All these models decompose the stress and strain in two summands, one representing the elastic effects and the other representing viscous effects. The simplest way to introduce the notion of viscoelasticity is to make use of analogies with simple mechanical models consisting of springs (elastic behaviour) and dampers (viscous behaviour). These analogies make it possible to have some conceptual insight into the physical behaviour of complex materials by breaking down the dissipative viscous processes (time-dependent) and energy-storage processes. Two basic elements are used:

- Spring: According to Hooke's law, the strain, γ, is proportional to the applied stress, τ, which reads $\tau = G\gamma$, with G the elastic modulus. The behaviour is independent of time, and physically, elastic elements represent the possibility of storing energy.

- Damper: The response of the damper, the plunger of which is pushed at the velocity $\dot{\gamma}$ is $\tau = \eta\dot{\gamma}$, where η is the viscosity. Physically, dampers represent dissipative processes that occur as a result of the relative motion between molecules, particles or polymer chains.

Depending on the configuration of the springs and dampers, different linear viscoelastic models are defined in the literature. Each model has each constitutive equation depending on the configuration. Therefore, each model has a different behaviour under creep-recovery and relaxation tests. Responses of each model are analysed here, and they will be used for the modelling of the agar gel, fitting these responses to the experimental data.

Maxwell Model

The Maxwell Model consists of a spring (G_1) and a damper (η_1) in series, see Figure 4.1. This model predicts that if a material is under constant strain, the stress relaxes gradually until it becomes zero. The model can anticipate relaxation behaviour but may not model creep accurately.

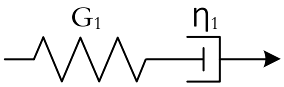

Figure 4.1: Maxwell Model.

In serie configuration, the total strain is divided into a spring, γ_{spring} and a damper, γ_{damper}. Equilibrium requires that the stress, τ be the same in both elements. So, $\gamma_{spring} = \frac{\tau}{G_1}$, $\dot{\gamma}_{spring} = \frac{\dot{\tau}}{G_1}$ and $\dot{\gamma}_{damper} = \frac{\tau}{\eta_1}$. Substituting shear rate expressions in Equation (4.55),

$$\dot{\gamma} = \dot{\gamma}_{spring} + \dot{\gamma}_{damper} \tag{4.55}$$

the differential equation of the model is obtained (Equation (4.56)),

$$\dot{\gamma} = \frac{\tau}{\eta_1} + \frac{\dot{\tau}}{G_1} \tag{4.56}$$

- Stress Relaxation response:

  If the strain is held constant then the differential equation becomes

  $$0 = \frac{\dot{\tau}}{G_1} + \frac{\tau}{\eta_1} \tag{4.57}$$

  Solving this differential equation with the initial condition $\tau_0 = G_1\gamma_0$ at $t = t_0$ then,

  $$\tau(t) = \tau_0 e^{-t/\lambda} \tag{4.58}$$

  with $\tau_0 = G_1\gamma_0$ and $\lambda = \eta_1/G_1$ relaxation time.

- Creep-Recovery response:

  If a constant stress, τ_0, is applied, the spring will stretch immediately and the damper will take time to react. The differential equation is

  $$\dot{\gamma}(t) = \frac{\tau_0}{\eta_1} \tag{4.59}$$

  Integrating this differential equation with the boundary condition of initial strain, $\gamma_0 = \tau_0/G_1$ leads to:

  $$\gamma(t) = \tau_0(\frac{1}{G_1} + \frac{t}{\eta_1}) \qquad \forall t \leq t_a \tag{4.60}$$

If the stress is removed after the applied pulse of τ_0, the spring reacts immediately, thus, there is an immediate elastic recovery τ_0/G_1. So, the strain function for recovery is,

$$\gamma(t) = \frac{\tau_0 t_a}{G_1} \qquad \forall t > t_a \tag{4.61}$$

When the stress is removed there is an instantaneous recovery of the elastic strain, and then, the strain rate is zero so that there is no further recovery. Although the relaxation behaviour of this model is acceptable as a first approximation to the actual response, it is inadequate in its prediction for creep and recovery behaviour.

Kelvin-Voigt Model

The Voigt Model is composed of a spring (G_1) and a damper (η_1) in parallel, see Figure 4.2.

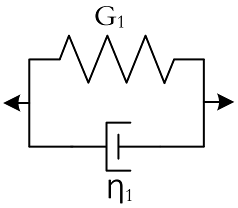

Figure 4.2: Kelvin-Voigt Model.

Differential equation for Kelvin-Voigt model is given by Equation (4.62),

$$\tau = G_1\gamma + \eta_1\dot{\gamma} \tag{4.62}$$

- Stress Relaxation response:
  If the strain is held constant, γ_0, the differential equation becomes

$$\tau = G_1\gamma_0 \tag{4.63}$$

Thus the stress is taken up by the spring and is constant, so there is no stress relaxation over time.

- Creep-Recovery response:

  If an instantaneous effort is applied, τ_0, at $t = 0$, the spring stretches immediately, but is held back by the damper, which cannot react immediately. The differential equation becomes

$$\tau_0 = G_1\gamma + \eta_1\dot{\gamma} \tag{4.64}$$

  Resolving this differential equation, with the initial condition of $\gamma_{(t=0)} = 0$

$$\gamma(t) = \frac{\tau_0}{G_1}(1 - e^{\frac{-t}{\lambda}}) \qquad \forall t \leq t_a \tag{4.65}$$

  where $\lambda = \eta_1/G_1$ is retardation time. If stress is suddenly removed from the strained body at time $t = t_a$, the body will revert to the unstrained state following Equation (4.66):

$$\gamma(t) = \frac{\tau_0}{G_1}\big(1 - e^{-\frac{G_1 t_a}{\eta_1}}\big)e^{-\frac{G_1(t-t_a)}{\eta_1}} \qquad \forall t > t_a \tag{4.66}$$

  When time tends to infinity, complete recovery of the strain takes place, thus strain tends to cero.

Standard Linear Model I

The Standard Linear Model I consists of a Voigt element (G_1 in parallel with η_1) in serie with a spring (G_2), as is shown in Figure 4.3.

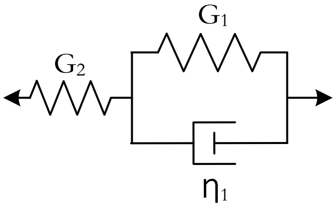

Figure 4.3: Standard Linear Model I.

Differential equation for Standard Linear Model I is

$$\tau + \frac{\eta_1}{G_2 + G_1}\dot{\tau} = \frac{G_2 G_1}{G_2 + G_1}\gamma + \frac{G_2\eta_1}{G_2 + G_1}\dot{\gamma} \tag{4.67}$$

- Stress Relaxation response:

  If a constant deformation is applied, at $t = 0$, the differential equation turns into,

$$\tau + \frac{\eta_1}{G_2 + G_1}\dot{\tau} = \frac{G_2 G_1}{G_2 + G_1}\gamma \tag{4.68}$$

  Solving this linear first order ordinary differential equation, yields:

$$\tau(t) = \gamma_0\left(\frac{{G_2}^2}{G_2 + G_1}e^{-\frac{G_1+G_2}{\eta_1}t} + \frac{G_2 G_1}{G_2 + G_1}\right) \tag{4.69}$$

- Creep-Recovery response:

  A constant stress pulse is applied, so,

$$\tau_0 = \frac{G_2 G_1}{G_2 + G_1}\gamma + \frac{G_2 \eta_1}{G_2 + G_1}\dot{\gamma} \tag{4.70}$$

  Resolving this equation, with the initial condition, that only the spring reacts initially, $\gamma_0 = \tau_0/G_2$,

$$\gamma(t) = \tau_0\left(\frac{1}{G_2} + \frac{1}{G_1}(1 - e^{-\frac{G_1}{\eta_1}t})\right) \qquad \forall t \leq t_a \tag{4.71}$$

  When time tends to infinity, strain tends to, $\gamma_\infty = \tau_0(\frac{1}{G_2} + \frac{1}{G_1})$. If the model is kept unloaded for a long period of time, creep recovery of the element occurs which is governed by the following equation:

$$\gamma(t) = \frac{\tau_0}{G_1}(1 - e^{-\frac{G_1 t_a}{\eta_1}})e^{-\frac{G_1(t-t_a)}{\eta_1}} \qquad \forall t > t_a \tag{4.72}$$

Standard Linear Model II - Kelvin Model - Zener Model

The Standard Linear Model II, also called as Kelvin model or Zener model, consists of a Maxwell element (G_1 in series with η_1) in parallel with a spring (G_2), see Figure 4.4.

Differential equation for this model is

$$\tau + \frac{\eta_1}{G_1}\dot{\tau} = G_2\gamma + \frac{\eta_1}{G_1}(G_2 + G_1)\dot{\gamma} \tag{4.73}$$

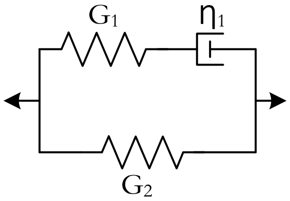

Figure 4.4: Standard Linear Model II.

- Stress Relaxation response:

  If the strain is constant with a value of γ_0, then the governing equation becomes

  $$\tau + \frac{\eta_1}{G_1}\dot{\tau} = G_2\gamma \tag{4.74}$$

  This differential equation can be solved with the boundary condition that $\tau = \tau_0 = \gamma_0(G_1 + G_2)$ at $t = 0$.

  $$\tau(t) = \gamma_0(G_2 + G_1 e^{\frac{-G_1 t}{\eta_1}}) \tag{4.75}$$

- Creep-Recovery response:

  If a constant stress, τ_0, is applied the governing equation becomes:

  $$\tau_0 = G_2\gamma + \frac{\eta_1}{G_1}(G_2 + G_1)\dot{\gamma} \tag{4.76}$$

  The solution of this differential equation can be obtained using the boundary condition $\gamma_0 = \tau_0/(G_2 + G_1)$ at $t = 0$. So

  $$\gamma(t) = \frac{\tau_0}{G_2} - \frac{\tau_0 G_1}{(G_2 + G_1)G_2} e^{\frac{-G_2 G_1 t}{\eta_1(G_2+G_1)}} \qquad \forall t \leq t_a \tag{4.77}$$

  If the stress is at a value of τ_0 and then completely removed, the governing equation becomes

  $$\frac{\eta_1}{G_1}(G_1 + G_2)\dot{\gamma} + G_2\gamma = 0 \tag{4.78}$$

  The solution of this differential equation can be obtained using boundary condition so that when the stress is removed, only the spring G_2 reacts

  $$\gamma(t) = \frac{\tau_0 G_1}{G_2(G_1 + G_2)}\big(e^{\frac{-G_1 G_2 (t-t_a)}{\eta_1(G_1+G_2)}} - e^{\frac{-G_1 G_2 t}{\eta_1(G_1+G_2)}}\big) \qquad \forall t > t_a \tag{4.79}$$

This predicts an instantaneous recovery of strain followed by an exponential decay.

Burgers Model

The Burgers Model consists of a Maxwell model (G_1 and η_1 in series) in serie with a Voigt model (G_2 // η_2), as is shown in Figure 4.5.

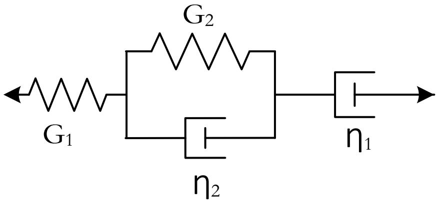

Figure 4.5: Burgers Model.

Differential equation for this model is:

$$\left(1+\frac{G_2}{G_1}+\frac{\eta_2}{\eta_1}+\frac{\eta_2}{G_1}\right)\ddot{\tau}+\frac{G_2}{\eta_1}\tau=(\eta_2+G_2)\ddot{\gamma} \tag{4.80}$$

- Creep-Recovery response:

  For stresses remaining constant with time, and in the absence of any initial strain, the strain in the Burger element at any instant of time is expressed as follows (Dey, Basudhar, et al., 2010):

  $$\gamma(t)=\tau_0\left(\frac{1}{G_1}+\frac{t}{\eta_1}+\frac{1}{G_2}(1-e^{-\frac{G_2 t}{\eta_2}})\right) \qquad \forall t\leq t_a \tag{4.81}$$

  where $\lambda=\eta_2/G_2$ is retardation time.

  If the Burger element is kept unloaded for a long period of time, creep recovery of the element occurs governed by the following equation (Dey, Basudhar, et al., 2010):

  $$\gamma(t)=\frac{\tau_0}{G_2}(1-e^{-\frac{G_2 t_a}{\eta_2}})e^{-\frac{G_2(t-t_a)}{\eta_2}} \qquad \forall t>t_a \tag{4.82}$$

Generalized Maxwell Model

The Generalized Maxwell Model consist of several maxwell elements (G_i in serie with η_i) positioned in parallel (see Figure 4.6).

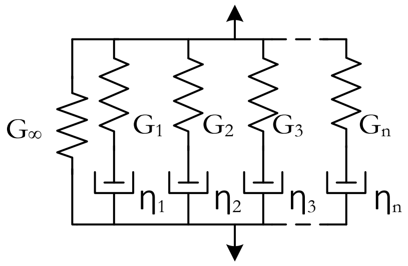

Figure 4.6: Generalized Maxwell Model.

- Stress Relaxation response:

  The solution of this model for stress relaxation is

$$\tau(t) = \sum_{i=1}^{n} \gamma_0 G_i e^{\frac{G_i}{\eta_i}t} \tag{4.83}$$

  Sometimes, an extra spring and an extra damper are connected in series as additional components to the generalized Maxwell model to enable also the description of a reversible elastic behaviour at very low strains and purely viscous flow behaviour at high-strain deformations.

  The Prony series for the shear relaxation is

$$G(t) = G_\infty + \sum_{i=1}^{N} G_i e^{-t/\tau_i} \tag{4.84}$$

  where G_∞ is the long term modulus (equilibrium modulus) once the material is totally relaxed, τ_i are the relaxation times (the higher their values, the longer it takes for the stress to relax).

  An alternative form is obtained noting that the elastic modulus is related to the long term modulus by

$$G(t=0) = G_0 = G_\infty + \sum_{i=1}^{N} G_i \tag{4.85}$$

Therefore,

$$G(t) = G_0 - \sum_{i=1}^{N} G_i(1 - e^{-t/\tau_i}) \tag{4.86}$$

This form is convenient when the elastic shear modulus G_0 is obtained from data independent from the relaxation data, and/or for computer implementation, when it is desired to specify the elastic properties separately from the viscous properties.

$$G(t) = G_0\left[1 - \sum_{i=1}^{N} g_i(1 - e^{-t/\tau_i})\right] \tag{4.87}$$

with $\sum_{i=1}^{N} g_i \leq 1$.

Generalized Kelvin-Voigt Model

The Generalized Kelvin Model consist of several Kelvin-Voigt elements (G_i in parallel with η_i) in serie, as is represented in Figure 4.7.

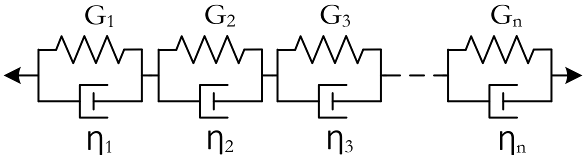

Figure 4.7: Generalized Voigt Model.

- Creep-Recovery response:

  The solution of this model for creep is

$$\gamma(t) = \sum_{i=1}^{n} \frac{\tau_0}{G_i}(1 - e^{-\frac{G_i}{\eta_i}t}) \tag{4.88}$$

  Sometimes, an extra spring and an extra damper are connected in series as additional components to the generalized Kelvin model to enable also the description of a reversible elastic behaviour at very low strains and purely viscous flow behaviour at high-strain deformations.

4.2.3.2 Quasi-Linear Viscoelastic (QLV) Model

The quasi-linear viscoelasticity (QLV) framework proposed by Fung (1981) relies on the use of two separate functions to describe the strain and time dependence, which requires that the material response be strain-time separable.

That is, this theory assumes that the mechanical behaviour can be decoupled into two parts: a linear viscoelastic stress-relaxation response and a time-independent elastic response. These behaviours are determined separately from the experiments. Typically, a relaxation function with fading memory is chosen to describe the temporal response, and an elastic model, such as hyperelasticity, describes the strain dependence (Bilston, Liu, et al., 2001).

The three-dimensional constitutive relationship in the framework of QLV is given by:

$$\sigma(t) = \int_0^t G(t-\tau)\frac{\partial\sigma^e(\epsilon)}{\partial\epsilon}\frac{\partial\epsilon}{\partial\tau}d\tau \tag{4.89}$$

where $\sigma^e(\epsilon)$ is the instantaneous elastic function and $G(t)$ is the reduced relaxation function. A discrete spectrum approximation in the form of Prony series can be assumed for $G(t)$.

$$G(t) = G_0\left[1-\sum_{i=1}^{N} g_i(1-e^{-t/\tau_i})\right], \qquad \sum_{i=1}^{N} g_i \leq 1 \tag{4.90}$$

where g_i and τ_i are the Prony series' parameters.

Although highly specific in its applicability, the attractive feature of the QLV model is its simplicity: it identifies a class of quasi-linearity that is appropriate for many tissues. However, for many other biological and bio-artificial tissues, the QLV model cannot achieve the desired accuracy (Geris, 2013). Some studies affirm that on the viscous side, QLV is limited to low strain-rates (0.06 - 0.75% s^{-1}) and is not sufficiently generalized to describe many of the complicated behaviours of soft tissue such as different short-term and long-term viscous responses. It is also unable to capture the effects of preconditioning unless a history-dependent state variable is added (Kerdok, 2006).

4.2.3.3 Non-linear Viscoelastic models (Visco-Hyperelastic)

In non-linear responses, stress is not proportional to the strain and modulus depends of the strain and the time. In this case, the material is not strain-time separable. Both the curves for creep at different stress, and the curves of stress relaxation at different strains, have different shape. Then neither linear viscoelasticity nor QLV describe the behaviour, because the relaxation modulus function depends on both time and strain, see Equation (4.91). The creep compliance function also depends on both time and stress.

$$G(t,\gamma) = \frac{\sigma(t,\gamma)}{\gamma} \tag{4.91}$$

The material may obey a more general non-linear superposition law, such as non-linear superposition in which the relaxation modulus function is written explicitly as a general function of time and strain. Some of the non-linear viscoelastic models developed in the literature are explained below.

Pioletti model

Pioletti, Rakotomanana, et al. (1998) presented a viscoelastic constitutive law for soft biological tissues, which is fully compatible with the principles of thermodynamics and is valid for large deformations. The proposed constitutive law describes the non-linearity of the stress-strain curves and the strain rate is considered as an explicit variable. Homogeneity, isotropy and incompressibility are assumed. The general constitutive law was expressed in term of elastic, W_e, and dissipative, W_v, potentials. The second Piola-Kirchhoff stress tensor, $\mathbf{S}$, is defined as:

$$\begin{aligned}\mathbf{S} = &-p\mathbf{C}^{-1} + 2\rho_0\bigg(\frac{\partial W_e}{\partial I_1} + I_1\frac{\partial W_e}{\partial I_2}\bigg)\mathbf{I} - 2\rho_0\frac{\partial W_e}{\partial I_2}\mathbf{C}\\ &+ 2\frac{\partial W_v}{\partial J_1}\mathbf{I} + 4\frac{\partial W_v}{\partial J_2}\dot{\mathbf{C}} + 6\frac{\partial W_v}{\partial J_3}\dot{\mathbf{C}}^2 + 2\frac{\partial W_v}{\partial J_4}\mathbf{C} + 2\frac{\partial W_v}{\partial J_5}\mathbf{C}^2\\ &+ 2\frac{\partial W_v}{\partial J_6}(\mathbf{C}\dot{\mathbf{C}} + \dot{\mathbf{C}}\mathbf{C}) + 2\frac{\partial W_v}{\partial J_7}(\mathbf{C}^2\dot{\mathbf{C}} + \dot{\mathbf{C}}\mathbf{C}^2)\end{aligned} \tag{4.92}$$

where $I_1 - I_3$ and $J_1 - J_7$ are the strain and strain rate invariants, respectively. p is the hydrostatic pressure and $\mathbf{I}$ is the identity tensor.

The elastic potential, W_e is taken from Veronda and Westmann (1970):

$$W_e = \frac{\alpha}{2}e^{\beta(I_1-3)} - \frac{\alpha\beta}{2}(I_2 - 3) \tag{4.93}$$

where α and β are two elastic (immediate) parameters and I_1, I_2 are two invariants of the deformation tensor.

The viscous potential for short time memory is presented by Pioletti, Rakotomanana, et al. (1998):

$$W_v = \frac{\eta}{4}J_2(I_1 - 3) \tag{4.94}$$

where η is a viscous parameter, and J_2 is a strain rate invariant, $J_2 = tr\dot{\mathbf{C}}^2$.

Incorporating the elastic and viscous potentials in Equation (4.92):

$$\mathbf{S} = -p\mathbf{C}^{-1} + \alpha\beta(2e^{\beta(I_1-3)} - I_1)\mathbf{I} + \alpha\beta\mathbf{C} + \eta(I_1 - 3)\dot{\mathbf{C}} \tag{4.95}$$

Miller model

Miller and Chinzei (2002) proposed a hyper-viscoelastic constitutive model, assuming incompressibility and isotropy. The model considers the non-linearity in stress-strain relationship as well as between stress and strain rate. The model is based on the Ogden hyperelastic constitutive model. The strain energy function is represented in the form of a convolution integral

$$W = \frac{2}{\alpha^2}\int_0^t \bigg(\mu(t-\tau)\frac{d}{d\tau}(\lambda_1^\alpha + \lambda_2^\alpha + \lambda_3^\alpha + 3)\bigg)d\tau \tag{4.96}$$

where λ_1, λ_2, λ_3 are the principal extensions, α is a material coefficient without physical meaning. t and τ denote time. Equation (4.97) describes viscous response of the tissue.

$$\mu = \mu_0 \left(1 - \sum_{k=1}^{n} g_k (1 - e^{-(t/\tau_k)}) \right) \tag{4.97}$$

μ describes the relaxation of the shear modulus of the tissue. μ_0 is the instantaneous shear modulus in undeformed state. τ_k are characteristic times.

The authors applied this model to swine brain tissue. The model accounts well for tissue mechanical properties in compression as well as in extension for strains up to 30% and strain rates ranging over five orders of magnitude. This model was later used by other authors (Gao, H Tay, et al., 2005; Wittek, Hawkins, et al., 2009) to model brain deformations.

Bilston model

Bilston, Liu, et al. (2001) developed a non-linear differential constitutive equation. The model couples a modified multi-mode convected Maxwell model (where the relaxation constants are strain-dependent and the viscosities are strain-rate dependent), with a modified Mooney hyperelastic elastic response. Both of these are modified by a non-linear damping function which is dependent on strain. The total Cauchy stress, $\boldsymbol{\sigma}$, is written as:

$$\boldsymbol{\sigma} = -p\mathbf{I} + \boldsymbol{\sigma}_E + \boldsymbol{\sigma}_V \tag{4.98}$$

where p is the hydrostatic pressure, $\boldsymbol{\sigma}_E$ is the elastic stress and $\boldsymbol{\sigma}_V$ is the viscoelastic stress. The elastic stress, $\boldsymbol{\sigma}_E$, is written as a Mooney-Rivlin rubber model, modified by a damping function, $f(I_1, I_2)$ which allows non-linear response in shear:

$$\boldsymbol{\sigma}_E = f(I_1, I_2) \left(\frac{G_E}{1+a} (\mathbf{B} - a\mathbf{B}^{-1}) \right) \tag{4.99}$$

where $\mathbf{B}$ is the left Cauchy-Green strain tensor, G_E is a long-term elastic modulus and a is a constant. The viscoelastic stress, $\boldsymbol{\sigma}_V$, is defined as a multi-mode Maxwell model, modified by the same damping function, f:

$$\boldsymbol{\sigma}_V = f(I_1, I_2) \sum_{i=1}^{N} \boldsymbol{\sigma}_i \tag{4.100}$$

where $\boldsymbol{\sigma}_i$ is the viscoelastic stress of each mode $i = 1, ..., N$.

The authors applied this model to bovine liver tissue (Liu and Bilston, 2002) and bovine brain tissue (Bilston, Liu, et al., 2001). However, the model was quite complex and it was computationally expensive to estimate parameter values. This model was later used to model pig kidney under shear loads (Nasseri, Bilston, et al., 2002) and the viscoelastic properties of bovine orbital connective tissue and fat (Yoo, Gupta, et al., 2011).

Brands model

Brands, Peters, et al. (2004) developed a non-linear viscoelastic material model for brain tissue and implemented it in an explicit FE code, to improve capabilities of FE head models to predict TBI in traffic accidents, falls or sports. For the modelling of the nearly incompressible brain tissue, the Cauchy stress, $\boldsymbol{\sigma}$, is written as the sum of a volumetric part, $\boldsymbol{\sigma}^v$, which depends on volumetric changes only, and a deviatoric part, $\boldsymbol{\sigma}^d$, which depends on change of shape only. The volumetric behaviour is assumed linearly elastic:

$$\boldsymbol{\sigma}^v = K(\sqrt{I_3} - 1)\mathbf{I} \tag{4.101}$$

with identity tensor, $\mathbf{I}$, and bulk modulus, K. The deviatoric part of the stress is modelled non-linear viscoelastic. It is decomposed in a number of viscoelastic modes, $\boldsymbol{\sigma}_i^d$, where N is the number of modes used.

$$\boldsymbol{\sigma}_i^d = \sum_{i=1}^{N} \boldsymbol{\sigma}_i^d \tag{4.102}$$

Hrapko model

Hrapko, Van Dommelen, et al. (2006) presented a differential viscoelastic model to describe the mechanical response of porcine brain tissue. The model considers non-linear viscous deformations in combination with non-linear elastic behaviour. The authors assumed the model incompressible in (Hrapko, 2008; Hrapko, Van Dommelen, et al., 2006). The total Cauchy stress tensor was written as the summation of the elastic and viscoelastic contributions. The authors also modelled the tissue as compressible in (Hrapko, Van Dommelen, et al., 2008a).

4.3 Modelling of experimentally tested materials

Some of the models presented in the previous section are used to described the mechanical behaviour of the materials tested in Chapter 3. Firstly, agar gel is modelled in Section 4.3.1. The flow curve of the agar gel is used in order to fit viscosity models. Viscoelastic behaviour of the agar gel is modelled by linear viscoelastic models. For these models, creep-recovery and relaxation tests of the agar are fitted. Secondly, porcine brain tissue is modelled in Section 4.3.2. The brain tissue is modelled using purely elastic models (based on constant shear rate tests) and by quasi-linear viscoelastic model. For that model, constant shear rate and relaxation tests are used.

4.3.1 Modelling of agar gel

Results from experiments performed on 3% agar gel in Section 3.2.3 are used with the aim of modelling its mechanical behaviour. Experimental data from rotational tests is modelled with viscous models. Experimental data from creep-recovery and relaxation tests is fitted with several linear viscoelastic models (explained in Section 4.2.3.1). The least squares method is used to obtain the parameters of the models.

4.3.1.1 Viscous models

The flow curve of 3% agar gel obtained from the rotational tests is modelled with viscous models presented in Section 4.2.2. Table 4.1 summarizes the parameters for each model.

Table 4.1: Parameters for rotational test

Model	**Parameters**
Newton (Ideal-viscous)	η = 905
Ostwald/de Waele (Power- law)	c = 356 p = 0.1
Bingham	τ_B = 237 η_B = 218

Figure 4.8 shows how models fit the flow experimental curve. It shows that a Newton model does not fit the experimental shear stress, that means that the gel has non-newtonian viscous behaviour. Both models for non-newtonian behaviour (Power-law and Bingham) fit well the experimental curve.

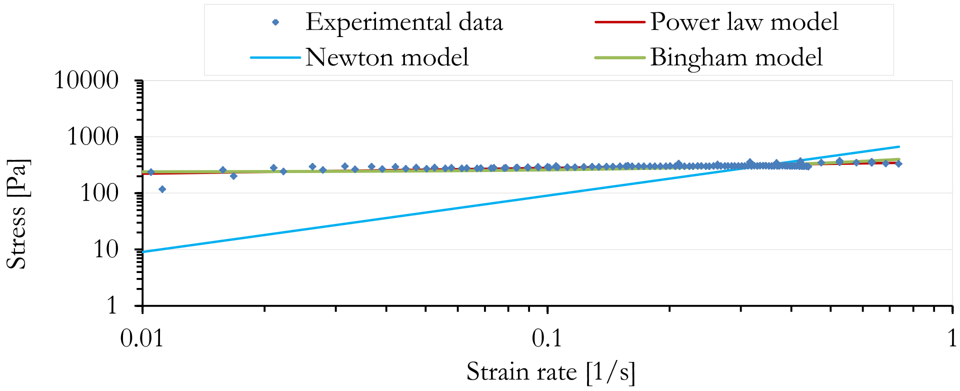

Figure 4.8: Flow curve of the 3% agar gel fitted with different viscous models.

4.3.1.2 Linear Viscoelastic Models

Relaxation tests

The relaxation curve obtained for the agar gel in Figure 3.11 is modelled with these linear viscoelastic models: Maxwell (Equation (4.58)), Voigt (Equation (4.63)), SLM I (Equation (4.69)), SLM II (Equation (4.75)) and Maxwell generalized (Equation (4.83)). Table 4.2 shows the parameters determined for each model.

Table 4.2: Parameters for relaxation test at $\gamma = 0.4\%$ of the tested 3% agar gel.

Model	Parameters	
Maxwell simple	$G_1 = 3255$	$\eta_1 = 5.4686{\cdot}10^6$
Kelvin-Voigt	$G_1 = 2972$	
SLM I	$G_1 = 14406$	$\eta_1 = 2.0284{\cdot}10^6$
	$G_2 = 3403$	
SLM II	$G_1 = 650$	$\eta_1 = 7.4058{\cdot}10^4$
	$G_2 = 2753$	
Maxwell II	$G_1 = 433$	$\eta_1 = 1.058{\cdot}10^4$
	$G_2 = 3145$	$\eta_2 = 7.28{\cdot}10^6$
Maxwell II with extra spring	$G_0 = 1184$	
	$G_1 = 433$	$\eta_1 = 1.0104{\cdot}10^4$
	$G_2 = 1969$	$\eta_2 = 2.68{\cdot}10^6$
Maxwell III	$G_1 = 676$	$\eta_1 = 1.8175{\cdot}10^5$
	$G_2 = 419$	$\eta_2 = 6.3{\cdot}10^3$
	$G_3 = 2561$	$\eta_3 = 2.5614{\cdot}10^8$
Maxwell III with extra spring	$G_0 = 2535$	
	$G_1 = 691$	$\eta_1 = 1.8916{\cdot}10^5$
	$G_2 = 419$	$\eta_2 = 6.309{\cdot}10^3$
	$G_3 = 10$	$\eta_3 = 2.6108{\cdot}10^4$

Figure 4.9 shows relaxation modulus of the agar gel fitted with linear viscoelastic models. Maxwell and Kelvin-Voigt simple models do not fit well the relaxation modulus of the experimental data. SLM I and SLM II give the same result and they give a more accurate approximation for the experimental data. Generalized Maxwell models fit the experimental curve completely. However, the improvement of generalized Maxwell models over SLM models is minimal. No differences are observed between Maxwell II or Maxwell III models or between Maxwell model with and without an additional spring.

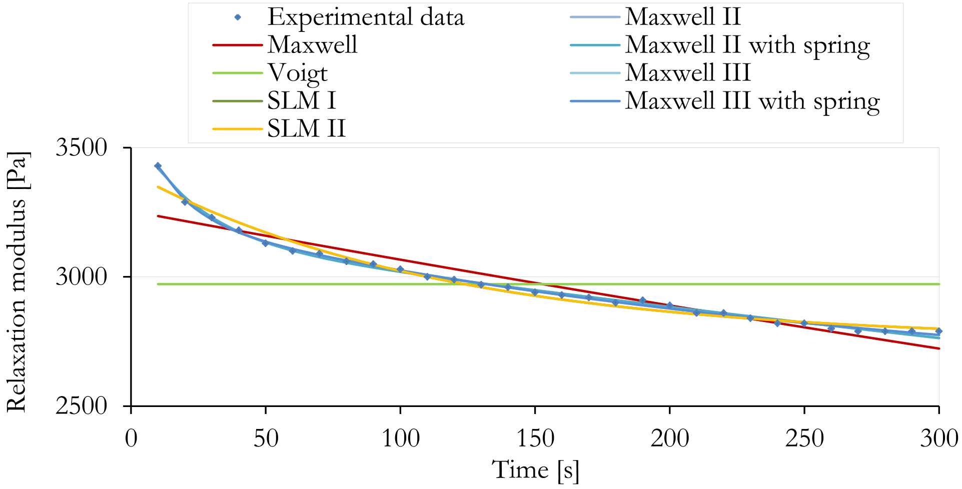

Figure 4.9: Relaxation modulus of the 3% agar sample fitted with linear viscoelastic models.

Creep-Recovery tests

Creep-Recovery results of the tested 3% agar gel (Figure 3.10) are fitted with the following linear viscoelastic models: Maxwell (Equations (4.60), (4.61)), Voigt (Equations (4.65), (4.66)), SLM I (Equations (4.71), (4.72)), SLM II (Equations (4.77), (4.79)) and Burgers (Equations (4.81), (4.82)). The parameters for each model are collected in Table 4.3.

Table 4.3: Parameters for creep and recovery test at $\tau = 40$ Pa of the tested 3% agar gel.

Model	**Parameters**	
Maxwell simple	$G_1 = 2.2475{\cdot}10^8$	$\eta_1 = 5.396{\cdot}10^7$
Kelvin-Voigt	$G_1 = 4424$	$\eta_1 = 1.0376{\cdot}10^7$
SLM I	$G_1 = 6237$ $G_2 = 6678$	$\eta_1 = 1.1122{\cdot}10^8$
SLM II	$G_1 = 3453$ $G_2 = 3225$	$\eta_1 = 2.9738{\cdot}10^7$
Burgers	$G_1 = 22862$ $G_2 = 8906$	$\eta_1 = 1.70{\cdot}10^8$ $\eta_2 = 9{\cdot}10^{-9}$

Figure 4.10 shows the experimental data together with the linear viscoelastic models. Maxwell simple model and Kelvin-Voigt simple models do not fit well the creep and recovery behaviour of the tested material. Burgers model fits the creep behaviour accurately, but it fails in the recovery range. It can be appreciated that standard linear models fit creep and recovery data precisely.

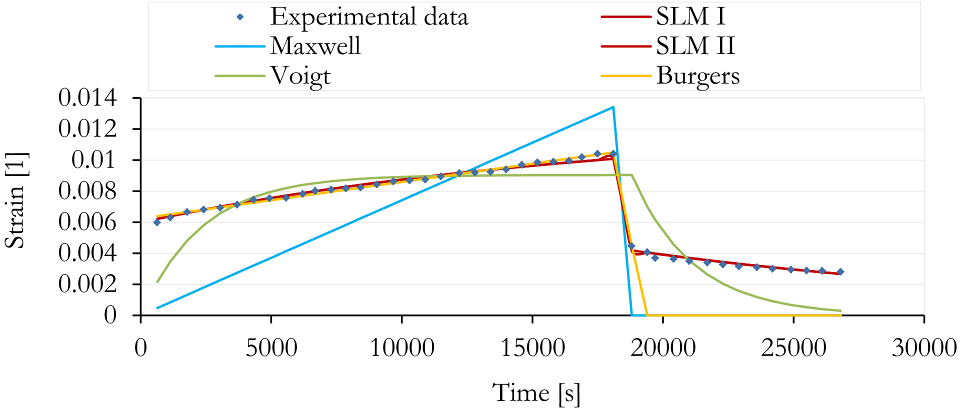

Figure 4.10: Creep and recovery experimental data of the 3% agar gel fitted with linear viscoelastic models.

4.3.2 Modelling of Porcine Brain Tissue

Porcine brain tissue is modelled based on the experimental results obtained in Section 3.3. It is characterised with linear elastic models and hyperelastic models. In order to model viscoelasticity, viscoelastic models are also used. In this case, a further step has been taken, and instead of modelling the material with linear viscoelastic model as in the agar modelling, quasi-linear viscoelastic models are used.

4.3.2.1 Linear Elastic model

The purely elastic models (linear elastic and hyperelastic) do not take the strain rate effect into account, therefore, these models are suitable at quasi-static strain rates, where the effect of the strain rate may be negligible. The lowest strain rate is chosen for the modelling of purely elastic models (0.001 s^{-1}).

Linear elastic models can be defined with two parameters, Young modulus, E, and Poisson's ratio, ν. In order to obtain the Young modulus, linear elasticity, isotropy, homogeneity and incompressibility of the material

($\nu = 0.5$) is assumed by,

$$E = 2G(1 + \nu) \tag{4.103}$$

The shear modulus is taken from three different tests and therefore three linear elastic models are defined, as it is shown in Table 4.4. Firstly, the plateau value of shear modulus, G, is taken from an amplitude sweep at 1 Hz. Secondly, the value of shear modulus at 0.1 Hz is taken from the frequency sweep at 1% strain. Thirdly, the linear elastic model is defined from the CSR test at 0.001 s^{-1}, fitting the shear modulus by the least square method, assuming linear elasticity at strains up to 10%.

Table 4.4: Linear elastic parameters for porcine brain tissue.

AS (1 Hz)	**FS (0.1 Hz)**	**CSR (0.001 s^{-1})**
$G' = 310.6$ Pa	$G' = 144.6$ Pa	
$G'' = 62.4$ Pa	$G'' = 31.3$ Pa	
$G = 316.8$ Pa	$G = 147.9$ Pa	$G = 82.3$ Pa
$E = 950.4$ Pa	$E = 443.7$ Pa	$E = 247$ Pa

4.3.2.2 Hyperelastic model

Porcine brain tissue is modelled with three different hyperelastic models: reduced polynomial model of 3^{rd} order (RP3), reduced polynomial model of 4^{th} order (RP4) and Lopez-Pamies model of 2^{nd} order (LP2). These hyperelastic models have been explained in Section 4.2.1.

Reduced polynomial models were used for brain tissue modelling in (Kaster, Sack, et al., 2011). Both the Polynomial and Reduced Polynomial models reached very good accuracy for the modelling of brain tissue under indentation loads to strains up to 15 - 20%. From our best knowdlege, these models have not been applied for the modelling of brain tissue under simple shear loads. Lopez-Pamies model is an hyperelastic model developed for rubber in (Lopez-Pamies, 2010) and from our best knowledge, this model has not been applied to soft tissues before.

Coefficients of the hyperelastic models are determined by least square method, fitting the mean value of the experimental data of CSR test at 0.001 s^{-1} with the simple shear stress equations of the RP3 (Equation (4.33)), RP4 (Equation (4.34)) and Lopez-Pamies (Equation (4.43)) models respectively. Table 4.5 shows the hyperelastic coefficients of each model.

Table 4.5: Hyperelastic parameters for porcine brain tissue from CSR at 0.001 s^{-1}.

RP3	**RP4**	**LP2**
C_{10} = 31.16	C_{10} = 35	μ_1 = 62.3
C_{20} = -102.67	C_{20} = -182.6	α_1 = -169.99
C_{30} = 169.94	C_{30} = 666.6	μ_2 = 41.43
	C_{40} = -951.25	α_2 = -8.64

4.3.2.3 Quasi-Linear Viscoelastic (QLV) Model

As it has been discussed with the results of the relaxation test (Section 3.3.2), quasi-linear viscoelasticity is assumed for the brain tissue. The QLV approach assumes that material behaviour can be decoupled into two effects: a time-independent elastic response and a linear viscoelastic stress relaxation response. These models can be determined separately from the experiments.

On the one hand, the elastic response is fitted with the experimental data of CSR at 0.1 s^{-1} (the fastest experimental data), defining in that way, the elastic response as instantaneous response. The elastic response is modelled by linear elastic model and by hyperelastic models, as it is explained below.

On the oher hand, viscoelastic behaviour is represented by Prony series of the relaxation modulus, defined by Equation (4.104).

$$G(t) = G_0\left[1 - \sum_{i=1}^{N} g_i(1 - e^{-t/\tau_i})\right], \qquad \sum_{i=1}^{N} g_i \leq 1 \tag{4.104}$$

g_i and τ_i are determined fitting $G(t)$ with experimental values obtained by the relaxation test at 1% strain (6 samples from two brains are tested). Table 4.6 shows the Prony serie parameters, considering shear modulus, $G_0 = 200$ Pa (determined by CSR test at 0.1 s^{-1}).

Table 4.6: Prony Serie parameters at 1% strain.

Prony 4 Terms	
$\tau_1 = 0.100$	$g_1 = 0.00033$
$\tau_2 = 1.09$	$g_2 = 0.23447$
$\tau_3 = 9.91$	$g_3 = 0.21368$
$\tau_4 = 100.02$	$g_4 = 0.14447$

Figure 4.11 shows the adjustment of Prony serie with experimental relaxation data at 1% strain.

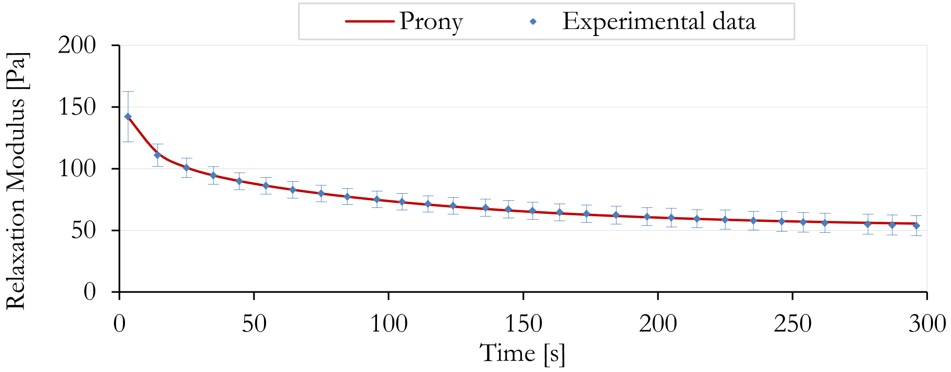

Figure 4.11: Experimental data from relaxation test at 1% of six samples of porcine brain tissue, together with Prony serie.

QLV model with Linear Elastic Part

A QLV model is defined by a linear elastic model as instantaneous response. A linear elastic model is fitted with experimental data from CSR at 0.1 s^{-1}, assuming linear elastic behaviour to strains up to about 10%. Therefore, the model is defined by $G = 200$ Pa. Assuming incompressibility, $\nu = 0.5$, the Young modulus is obtained, $E = 600$ Pa. As it is shown in Figure 4.12, linear elastic model fits experimental data to strains up to 10%.

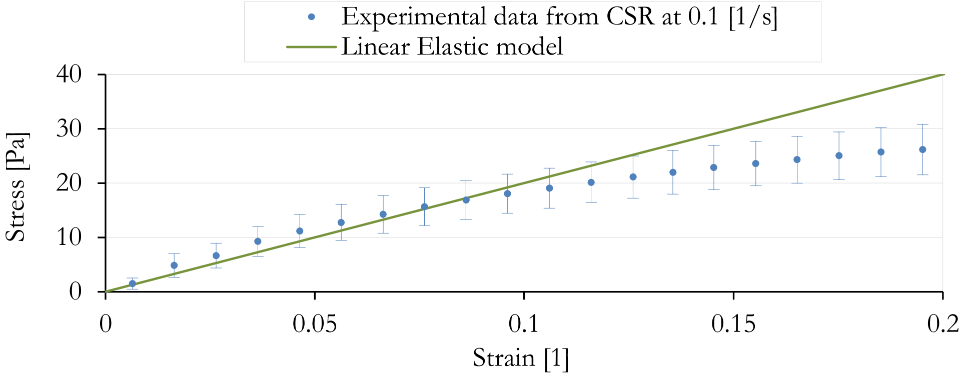

Figure 4.12: Experimental data of porcine brain tissue from CSR test at 0.1 s^{-1} with linear elastic model fitted by least square method to strains up to 10%.

QLV model with Hyperelastic Part

QLV model is also represented with hyperelastic model as elastic response. While linear elastic model can fit experimental data to strains up to 10%, hyperelastic models can fit experimental data to strains up to 50%. Reduced polynomial models of 3^{rd} and 4^{th} orders and Lopez-Pamies model of 2^{nd} are defined (Table 4.7).

Table 4.7: Hyperelastic parameters for porcine brain tissue from CSR at 0.1 s^{-1}.

RP3	**RP4**	**LP2**
$C_{10} =$ 100	$C_{10} =$ 96	$\mu_1 =$ 118
$C_{20} =$ -337	$C_{20} =$ -413	$\alpha_1 =$ -52.3
$C_{30} =$ 571	$C_{30} =$ 1420	$\mu_2 =$ 81.9
	$C_{40} =$ -2000	$\alpha_2 =$ -1.6

Figure 4.13 shows experimental data of CSR at 0.1 s^{-1} fitted with the mentioned hyperelastic models, to strains up to 50%.

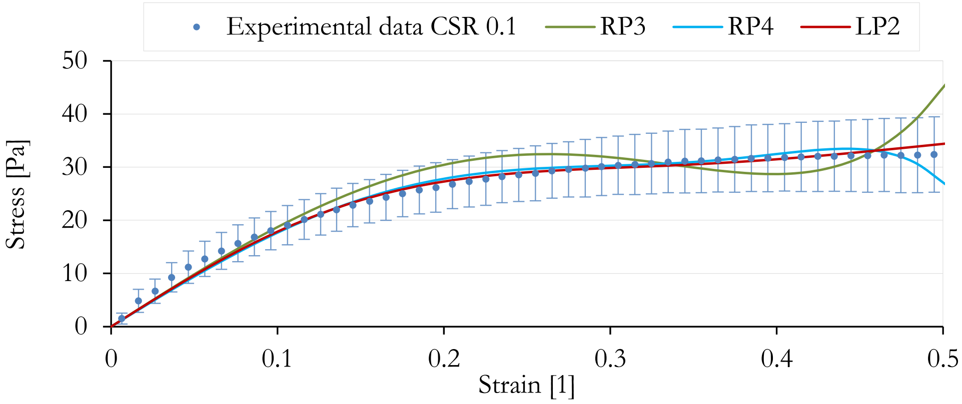

Figure 4.13: Experimental data of porcine brain tissue from CSR test at 0.1 s^{-1} with hyperelastic models fitted by least square method to strains up to 50%.

4.3.3 Results

The defined models are simulated in ABAQUS (6.13). A cylindrical sample is modelled with a height of 2 mm (the average gap value of the 6 samples tested at 0.001 s^{-1}). 6400 C3D8H eight-node, hexahedral elements are used. The center of the sample is modelled by 800 C3D6H six-node, wedge elements. Because of the tissue incompressibility, hybrid elements are chosen. In order to simulate rotational shear load performed by the rheometer, the displacement on the lower surface of the sample is fixed and a boundary condition prescribing a rotation is applied on the upper surface. For the simulation of purely elastic models, *Static General* step is used, whereas a *Visco* step is applied for the viscoelastic models. A direct method is used to solve the simulation, with *Full Newton* solution technique.

Linear Elastic Models

Figure 4.14 shows the linear elastic models together with the experimental data. Strains up to 20% are presented, since for larger strains, linear elastic models differ significantly from experimental data.

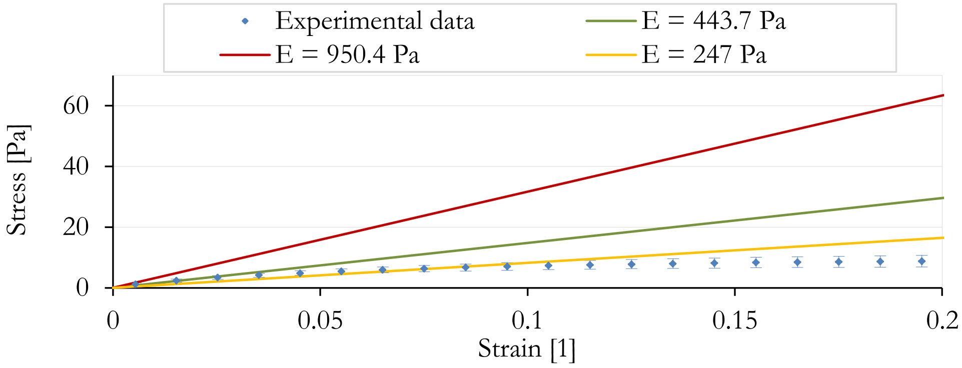

Figure 4.14: Linear elastic models with the experimental data of the CSR test at 0.001 s^{-1}.

It can be observed that linear elastic model could be apropiate to strains up to 10% in the case that linear elastic properties are defined at low strain rates (CSR at 0.001 s^{-1}).

Hyperelastic Models

Figure 4.15 shows the simulation in Abaqus of hyperelastic models at low strain rate (0.001 s^{-1}).

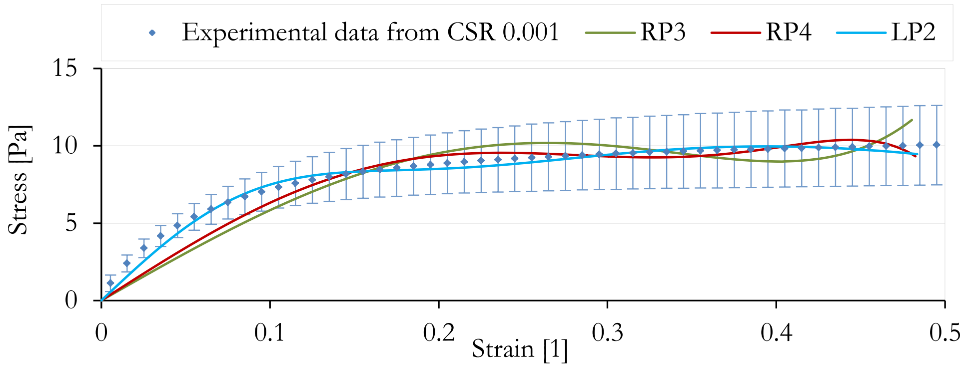

Figure 4.15: Experimental data of CSR at 0.001 s^{-1} with hyperelastic models.

It is observed that at low strains (0 - 10%) polinomial models do not fit experimental data accurately. Lopez-Pamies model however fits accurately the experimental data from small strains to large ones. It fits well the average of the experimental data and it is within the dispertion of the values of the samples. Besides, it avoids the oscillations of polynomial models.

QLV model with Linear Elastic Part

A QLV model is defined by linear elastic model ($G = 200$ Pa, $\nu = 0.5$, $E = 600$ Pa) as instantaneous response. Figure 4.16 shows the QLV model simulated in Abaqus together with the experimental data at different strain rates.

This model can approximate the porcine brain behaviour at different strain rates to strains up to 8 - 10%.

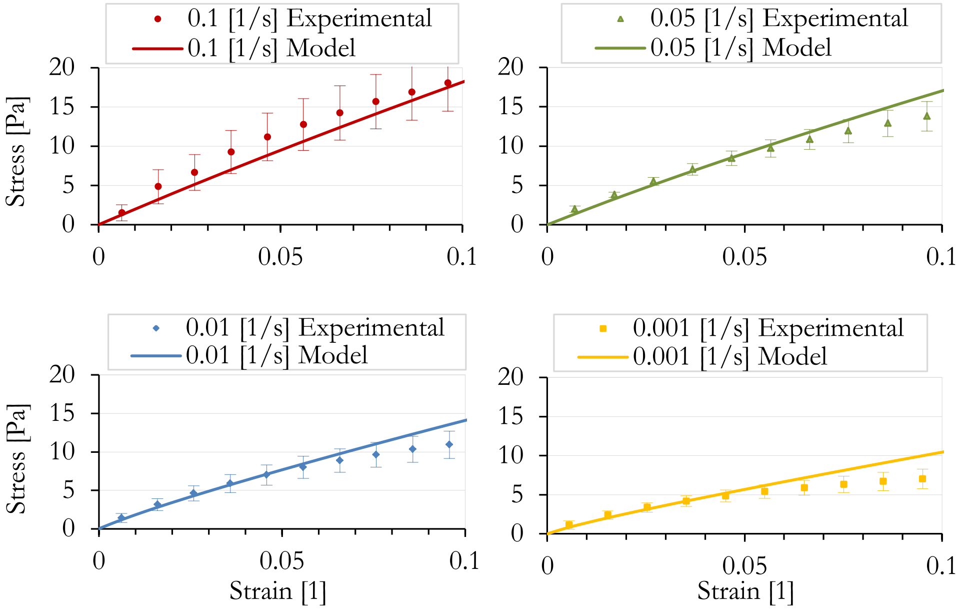

Figure 4.16: Quasi-linear viscoelastic model with linear elastic part. And experimental data at 0.001, 0.01, 0.05 and 0.1 s^{-1}.

QLV model with Hyperelastic Part

Figure 4.17 shows the response of QLV models with hyperelastic part, together with the experimental data at each strain rate.

It can be observed that the three models adjust well the experimental data with the effect of the strain rate to strains up to 10%. For larger strains RP3 model shows oscillations making this model not suitable for this experimental data. RP4 and LP2 models have similar behaviour and they fit accurately the medium velocities of 0.01 and 0.05 s^{-1} to strains up to 50%. At fast strain rate (0.1 s^{-1}), they underestimate the experimental behaviour from 20% strain. And at low strain rates (0.001 s^{-1}), they overestimate the tissue's behaviour from 10% of strain.

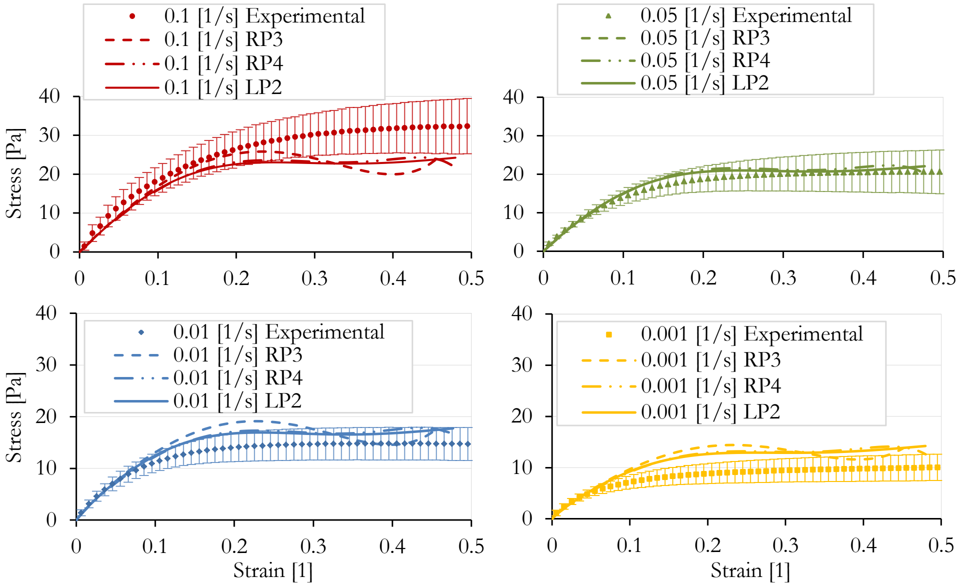

Figure 4.17: Quasi-linear viscoelastic models with hyperelastic part. And experimental data at 0.001, 0.01, 0.05 and 0.1 s^{-1}.

The elastic part of a viscoelastic model is considered the instantaneous response. In that case, the instantaneous response is considered 0.1 s^{-1}, since at higher strain rates, it has been observed a risk of migration of the sample from the gap of the rheometer. In order to fit better the experimental data of CSR 0.1 s^{-1} and improve the underestimation, the Lopez-Pamies model of 2^{nd} order is fitted to the higher values obtained from CSR test at 0.1 s^{-1} instead of to the medium values, as it is shown in Figure 4.18.

Figure 4.19 shows the results of Abaqus simulation with Lopez-Pamies model fitted at higher values. The model fits experimental data at 0.1 s^{-1}, but it slightly overestimates the experimental data at other velocities. It can be shown that the LP2 model fitted with previous values fits the experimental data more accurately.

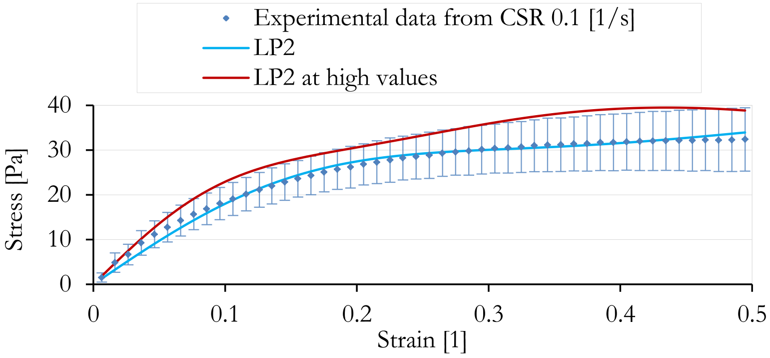

Figure 4.18: Fitting of the LP2 models with experimental data of CSR at 0.1 s^{-1}.

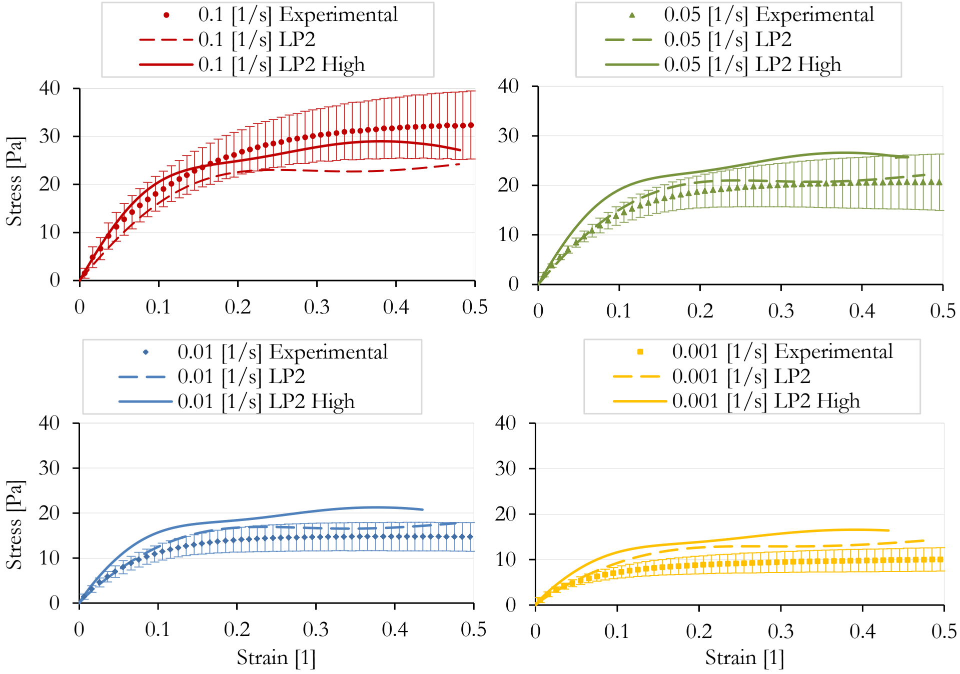

Figure 4.19: Quasi-linear viscoelastic model with LP2 models as elastic part. And experimental data at 0.001, 0.01, 0.05 and 0.1 s^{-1}.

4.3.4 Simulation at oscillatory loads

Linear elastic, hyperelastic and quasi-linear viscoelastic models defined for porcine brain tissue have been analysed in the previous section. The models have been simulated at constant shear rate, i.e. in a rotational experiment. However, in order to compare these models at other load configurations, some synthetic experiments have been performed.

A cube of 20x20x20 mm is simulated in Abaqus. The models are defined above (Section 4.3.2): Linear elastic model (Table 4.4 (data taken from FS at 0.1 Hz)), hyperelastic model (Table 4.5 (LP2)), QLV model with linear elastic part (Table 4.6 with $E = 600$ Pa) and QLV with hyperelastic part (Table 4.6 and Table 4.7 (RP3)).

Shear load

An instantaneous shear load of 4 N is applied to the top surface of the cube. The response of the cube is observed during 10 s. *Dynamic, Implicit* step was used, with *Full Newton* solution technique. Figure 4.20 shows the response of the models at the shear load.

Compression load

An instantaneous compression load of 10 N is imposed in the top surface of the cube. The response of the cube is observed during 10 s. *Dynamic Implicit* step was used, with *Full Newton* solution technique. Figure 4.21 shows the response of the models at a compressive load. It presents the displacement of the center node of the upper surface of the cube in the load direction.

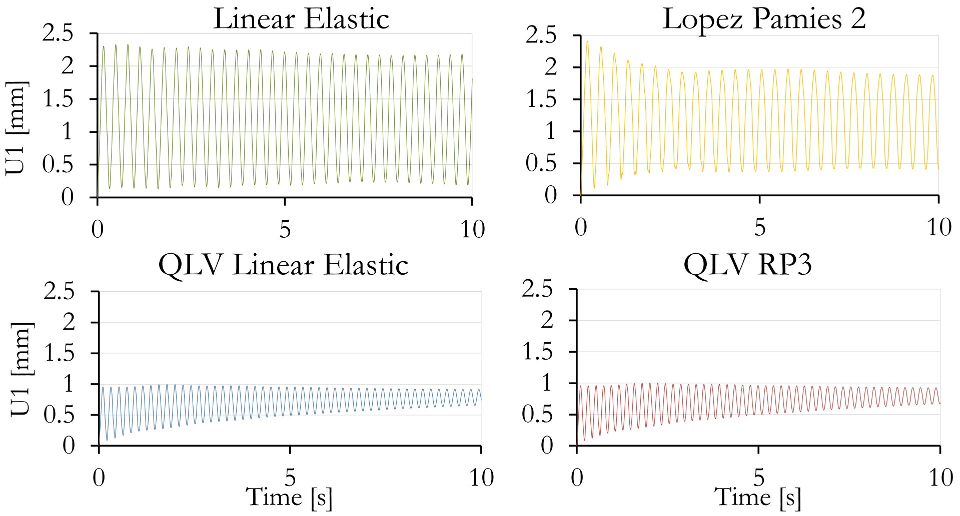

Figure 4.20: Responses of different models at an instantaneous shear load of 4 N. Results obtained from Abaqus simulation.

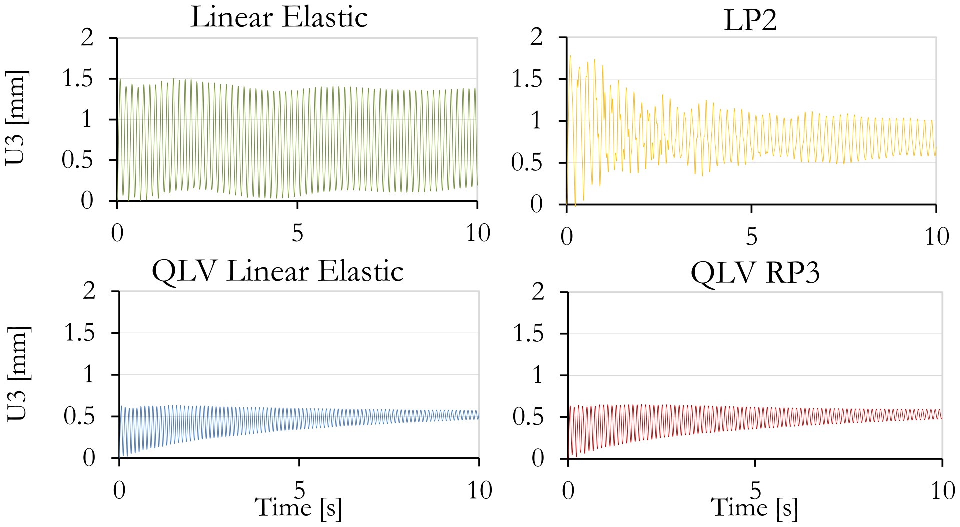

Figure 4.21: Responses of different models at an instantaneous compression load of 10 N. Results obtained from Abaqus simulation.

In both cases, shear and compression loads, the most notable result is that QLV models show a damped response, comparing with purely elastic materials. The response of linear elastic and hyperelastic models are very similar. Some damping can be observed in hyperelastic models, compared to linear elastic models. However, this effect is negligible if it is compared with the damping of QLV models. The difference between QLV model with linear elastic or hyperelastic part is completely negligible.

4.4 Discussion

Although several tests have been performed in this methodology, not all of them are necessary for the modelling of the tissue. Amplitude sweep is essential in order to know the LVE range. Frequency sweep is not considered necessary for the application of surgical simulation, since tissue is not excited at high frequencies neither at oscillatory loads. Provided that the analysed material is a solid and not a fluid, it is not of interest to model it with viscous models. Therefore, test for obtaining flow and viscosity curves can be also taken out.

In order to characterise and model the tissue, some steps can be taken into account: if the tissue needs to be modelled with a purely elastic model, the viscous part is considered negligible. For the elastic part, it would be enough to perform a constant shear rate, concretely at the shear rate that the real tissue will be excited. To model the material with linear elastic model, the model will be fitted with the initial slope of the curve, i.e., the linear zone of the curve. On the contrary, if a hyperelastic model is used, the model will be fitted until the desired strain range. In this case, the model describes the mechanical behaviour of the tissue in all the deformation zone, not only in the linear elastic zone. To model the tissue with a linear viscoelastic model, it would be necessary to perform a creep-recovery test and/or relaxation test, in order to adjust the parameters of the model and choose the model that best fits the experimental data (as it has been seen in Section 4.3.1).

Finally, with the aim of characterising the material with a QLV model, two tests are necessary: on the one hand, CSR at high strain rate provides the elastic response, i.e. the instantaneous response of the tissue. On the other hand, a relaxation test describes the viscoelastic behaviour of the tisse, and it can be easily described by the Prony serie.

In the case that these models are not realistic enough, and more accuracy is required, a non-linear viscoelastic model should be applied. For this case, non-linear elastic and non-linear viscous models will be joined. The application of this kind of models is out of scope of this thesis, due to the mathematical complexity and its difficulties for their real-time application.

Brain tissue is modelled with linear elastic, hyperelastic and quasi-static viscoelastic models. The purely elastic models are defined with mechanical properties characterised at quasi-static strain rate (0.001 s^{-1}). Linear elastic model fits the experimental curve reasonably well to strains up to 10%, whereas hyperelastic models represent accurately the tissue behaviour to strains up to 50%. Lopez-Pamies model is more accurate than reduced polynomial models, besides, the model avoids the oscillations produced by polynomial models. QLV models are defined by a linear viscoelastic part (from relaxation test at 1% strain) and by an elastic instantaneous response (from CSR at 0.1 s^{-1}). Defining the elastic response by linear elastic model, QLV model can be an adequate approximation to strains up to 10%. Defining the elastic response with hyperelastic models, the tissue behaviour is well represented to strains up to 50%.

Although all presented models aim to be feasible for haptic systems for surgical simulation, the choice of the model would still depend on the application. As it is concluded in (Mendizabal, Aguinaga, et al., 2015), there are two main questions in order to choose the most suitable model: does the strain rate effect really take place in brain surgery procedures? What are the largest strains that would occur in a brain surgery?

If the strain rate is not taken into account and the maximum strains are around 10%, the linear elastic model turns out to be the best choice.

The model would be fitted to quasi-static experimental data or to the strain rate considered in the process. Conversely, if the strains are larger than 10%, the hyperelastic models (fitted to the desirable strain rate) would cover the requirements.

However, if the strain rate is taken into account, the QLV model with linear elastic part is the best choice for strains up to 10%. Whereas, for larger strains, QLV with hyperelastic part should be used.

In the case that all requirements should be met, i.e., the strain rate effect, the large strains and a very high accuracy, the model should be a non-linear viscoelastic model. However, due to the complexity of the implementation of these models, the execution time of the simulation can easily grow beyond the limits required to achieve a real-time simulation. If these models are used, the computation should have less strict time requirements.

When an instantaneous force is applied to the material and the response of the models (linear elastic, LP2, QLV with linear part and QLV with hyperelastic part) is observed, it can be noted that the difference relies on the purely elastic and viscoelastic models. Viscoelastic models show a damping that makes the displacement smaller over the time. Whereas, the purely elastic materials continue oscillating without damping.

CHAPTER 5

APPLICATION: SURGERY SIMULATION SYSTEM

5.1 Introduction

Robotic system integration in medicine and more specifically in the surgical field entails a remarkable improvement in the delivery of healthcare services. Nowadays, robotic devices and computer-assisted technologies are included as a mean of guidance, diagnosis, verification and general assistance during the performance of a surgical intervention (Landeira, 2014).

However, the use of robotic devices in surgery creates new challenges that must be overcome for their successful deployment. A robot acting on a tissue exerts a force and produces deformations over which the surgeon has no direct feedback. Surgeons do not have an idea of the stress to which the tissue is subjected. The human eye cannot quantify the functional or mechanical damage of the tissue. Therefore, surgeons judge the damage range based on their own experience.

In this context, the tracking of the deformation of the organs is required for assistive technologies such as augmented reality (AR). Augmented reality is a technology that aims to embed virtual objects in the real world, showing the user the set of objects (virtual and real) as a single world. In contrast to virtual reality, where the user is completely immersed in a synthetic world, AR consists in adding virtual objects to the real world.

These assistive technologies aim to support the surgeon with a visual feedback of the deformations that are taking place on the tissues, or to support the surgeon by locating the position of a malignancy to be removed from an organ. In most cases, the inclusion of sensors to track the position of the organs of the patient is not feasible. Thus, the use of alternative approaches such as computer vision techniques has become a real need to solve this kind of problems.

Nevertheless, the very presence of the robot produces occlusions that limit how much information can be obtained using only computer vision. The combination of computer vision with a suitable physical simulation can be used to reduce the missing information. In this case, the accuracy required for surgical simulators remains important. In contrast to deformable models used in video games and animations, the purpose of soft tissue models in medical simulation is to model realistically the behaviour of biological tissues. Consequently, the simulation of the deformation of the tissue should be controlled using real material parameters. Thus, these parameters should be obtained from biomechanics experiments instead of intuitively adjusted parameters. However, in robotic guidance and surgery assistance systems, accuracy is not only essential, but also computational performance must be taken into account, in order to provide a fast enough visual feedback to the surgeon. Therefore, it is critical to obtain a compromise between accuracy and computational cost, in this application. Being able to provide surgical realism at interactive rates of simulation is one of the most challenging problem in robot surgical assistance systems (Cotin, Delingette, et al., 2000).

In this sense, this chapter presents the basis for the development of a robot-assisted surgical system (Landeira, Sánchez, et al., 2014) combined with a vision module through which it is possible to obtain the deformations of a non-rigid object when a force is applied to it. A visual feedback system for the surgeons could be developed based on the information obtained from this system.

This chapter is divided in the following sections: Section 5.2 describes some research works presented in the literature, that aim to complement a robotic system with vision techniques, in order to support surgeons with a visual feedback of the deformations of the tissues in surgical procedures. Section 5.3 describes the proposed method. The configuration of the system, the robotic platform and the object deformation are described. The method is applied to ex-vivo calf brain and porcine kidney tissues in Section 5.4. In that section, the accuracy level and computation time of the method are studied. Finally, a discussion is presented in Section 5.5.

5.2 State of the Art

Some recent works in the literature present robotic systems complemented by vision techniques in surgery. Hamarneh, Amir-Khalili, et al. (2014) presented pre-operative surgical planning, intra-operative image registration and augmented reality visualization for image-guided tumour identification. Their work aims to help the surgeon determining the tumour localization and resection margins. They focused on kidney cancer cases with robot-assisted partial nephrectomy performed with a da Vinci surgical robot (Intuitive Surgical, Inc.). They built the biomechanical model of kidney tissue and tumour with FEM using a co-rotational tetrahedral formulation and an Eulerian implicit solver. However, their work is more focused on surface reconstruction than the 3D deformation of an organ.

Haouchine, Dequidt, et al. (2013) present an image-guided biomechanical model that captures the complex deformations undergone by the liver during surgery. The system works with laparoscopic stereo cameras and a FEM is used to capture the behaviour of the object and compute the deformation. The FEM is based on a co-rotational formulation with stress-strain relationship taken from the literature. However, the position of the camera should be static, and in some cases, the simulations are not executed in real time. Furthermore, Haouchine and Dequidt (2014) proposes a real-time method to register the non-linear elastic model deformations using the image points acquired from a monocular camera. Nevertheless, this solution is based on an orthographic projection, whose computation is more simple to solve compared to the perspective projection. In that case, they used a Saint-Venant-Kirchhoff model in FEM formulation.

In both, (Haouchine and Dequidt, 2014; Haouchine, Dequidt, et al., 2013) the authors perform a computer vision based tracking of the organs based on features (characteristics such as corners, blobs, etc. which are easily identifiable in an image). However, in environments such as medicine or industry, it is sometimes difficult to perform a tracking based only on visual cues (often essential for a vision system), either by the lack of textured areas and models or the environmental conditions (as blood in medicine).

5.3 Proposed method

Compared to existing solutions, the tracking algorithm used in this application does not requiere features. That means that the proposed method avoids the use of formulations that are not usually robust for texture-less surfaces or objects. This makes the approach robust against illumination changes and adaptable for tracking any type of object (in terms of its geometrical shape). Furthermore, this method avoids the ambiguity that can be caused by orthographic projections. Another advantange of the method is that the camera is not required to be static.

The visual feedback of the deformation state of the object relies on a non-linear Total Lagrangian Finite Element formulation, that provides a fast and accurate enough biomechanical model of the object. In this case, a Saint-Venant-Kirchhoff model is implemented, but more complex material laws, such as hyperelasticity and viscoelasticity could be easily implemented.

Moreover, compared to other works, the mechanical properties of the models are obtained experimentally, using the methodology developed in this thesis, in order to simulate a more realistic behaviour of the materials.

Additionally, the presented method is modular, i.e., it allows the incorporation or replacement of certain modules. Thus, the performance of the presented framework can be improved, for example, by using new tracking methods, or accuracy can be improved using more complex material models.

5.3.1 Configuration of the system

Figure 5.1 illustrates the configuration of the system. The vision module is composed by a RGB-D camera that obtains both the colour and depth data of a scene. However, this information is incomplete since it has noise and large holes. Thus, it is not suitable to provide a correct visual feedback. The acquired raw information is used to feed the input of a FEM physical model in order to obtain a correct physical behaviour of the tissue and use the resulting deformation to complete the deformation in areas whose surface is missing. In this sense, the model represented as a triangle mesh is converted to a tetrahedral mesh to adjust it to the FEM formulation. This triangle mesh, in turn, is captured through a scanning process performed by the 3D Sense Scanner. It is worth mentioning that the phases that the physical model simulation involves, require specific types of models (different geometry mesh and material properties of the bodies). Two different models have been used to perform the experimentation process: a porcine kidney and a calf brain.

The system is divided into two main sections: *Robotic Platform* and *Object Deformation*. Since we focus only on the deduction of the deformations of the organ, the process of computation the camera pose (camera tracking problem) is carried out through a marker based system. This provides a level of accuracy high enough to ignore the error of the position of the camera. Next, a description of each step is presented.

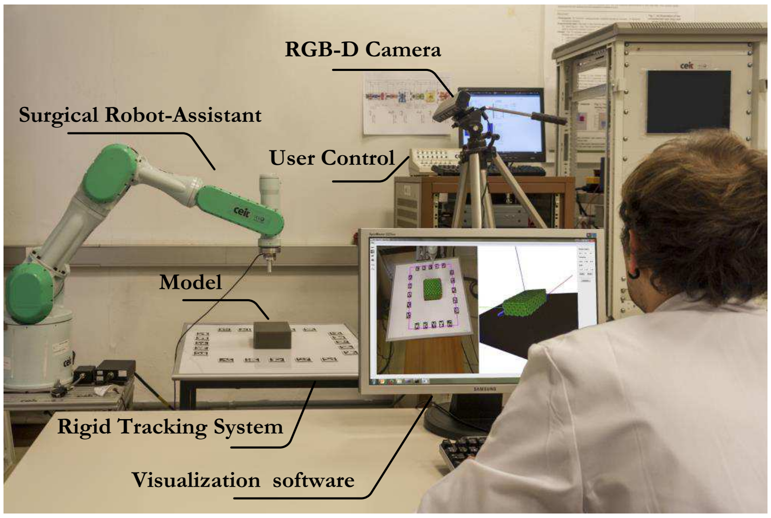

Figure 5.1: Configuration of the system. Robot-assisted surgical system combined with a vision module.

5.3.2 Robotic Platform

The selected robot-assistance module has been developed as a prototype for a cooperative robotic platform aimed at assisting in surgery for lumbar transpedicular fixation in (Landeira, Sánchez, et al., 2014).

The surgical assistant used is composed by a commercial PA10-7C robotic arm (Mitsubishi Heavy Industries Ltd.) with open control architecture. This implies that, using a generic programming language, it is possible to develop the control algorithms of the robot in a control PC in an independent way. The PA10-7C is a 7DoF open chain serial manipulator, with all revolute joints that have a well-defined rotation axis. Its maximum load capacity is 98 N and it can achieve a distance of 1.03 m when fully extended. The robot has a force/torque sensor, Mini40 (ATI Industrial Automation, NC, USA). In that way, the force performed by the robot in the soft tissue is recorded. Figure 5.2 shows the robotic arm used as indenter (left) and its exploded view (right). The end of the robotic arm consists of a force/torque sensor, a grip, a large indenter and an smaller one.

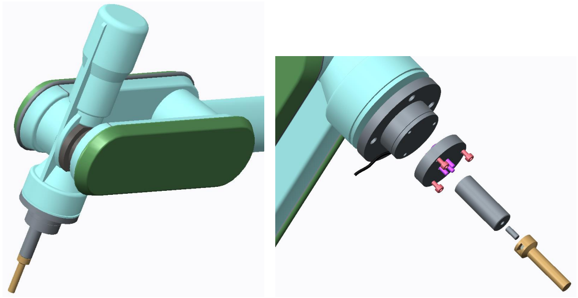

Figure 5.2: Representation of the robotic arm (left) and exploded view of its end (right).

5.3.3 Object deformation

The main challenge of the non-rigid tracking problem is to know the transformation of the mesh after suffering a deformation. Therefore, this phase is responsible for performing the deformable registration of the non-rigid model.

As it is shown in Figure 5.3, this step is divided into two main steps: *Model Preprocessing* and *Mesh Physical Registration.*

The *Model Preprocessing* is an offline process which consists in defining a proper parametrization of the physical model. This process comprises three steps: the keypoint generation, material characterisation and FEM initialisation.

The online execution *Mesh Physical Registration*, calculates the correspondences between the model and the input point cloud acquired from the RGB-D camera to subsequently obtain the physical registration with the FEM formulation. This process comprises two steps: The keypoint selection and the correspondence matching.

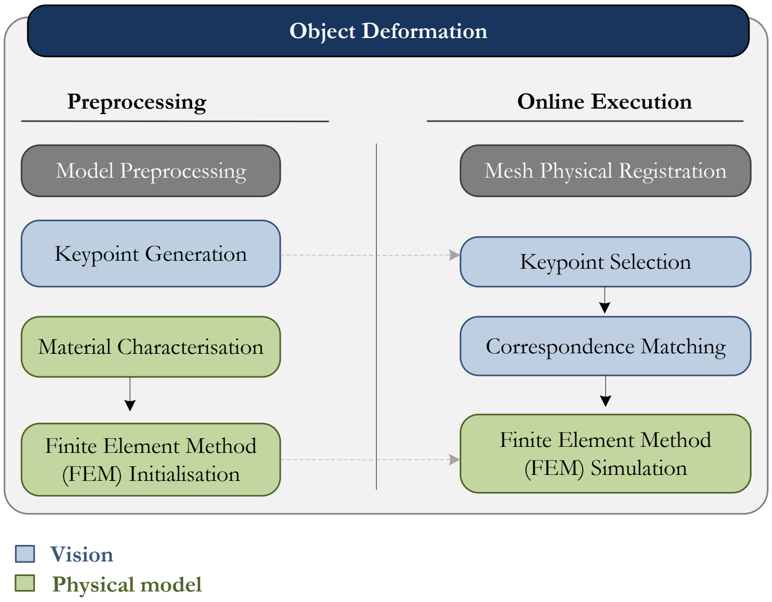

Figure 5.3: Overview of the proposed object deformation method (offline and online phases).

5.3.3.1 Model Preprocessing

Keypoint generation

This phase generates a set of control points to relate the input point cloud acquired in each frame of the camera and the 3D mesh of tetrahedrons. These control points or keypoints are in fact the vertices that are on the surface of the tetrahedral mesh, thereby obtaining a set of uniformly distributed points on the surface.

Material characterisation

The procedure to be simulated is an indentation deformation performed by the robot arm at a constant and slow velocity. Therefore, although it could be interesting to simulate the strain rate effect of the soft tissue, it is not taken into account in this section. If the viscoelasticity is not considered and the maximun strains are supposed to be around 10%, as a first step, a linear elastic characterisation would provide a sufficiently precise simulation, while allowing real-time performance.

Amplitude sweeps have been performed in cylindrical samples (diameter = 25 mm and thickness = 2 - 4 mm). The mechanical properties of the tissues are defined within linear viscoelastic range. A strain ramp was imposed from 0.001% to 100% at 1 Hz. The value of shear modulus, G, within linear viscoelastic range is obtained. Density, ρ, has been considered constant within the tissue sample. Poisson's ratio, ν, has been selected for each material. Linear elasticity, isotropy and homogeneity of the material has been assumed, and therefore, Young modulus, E, is defined by $E = 2G(1+\nu)$. Table 5.1 shows the values of the mechanical properties established for each material.

Table 5.1: Mechanical properties of the tested materials: porcine kidney and calf brain.

	Kidney	**Brain**
ρ [kg/m^3]	1000	1000
E [Pa]	1500	1085
ν	0.45	0.48

Finite Element Method (FEM) Initialisation

Two requirements have been set for the development of the simulation system. The system has to be able to handle large deformations and to simulate the deformations with fast enough execution times, enabling a real-time simulation. In order to fulfill both demands, a non-linear Total Lagrangian explicit Finite Element formulation has been selected. This method has been explained in Section 2.3.3.

The linear elastic material extended to non-linear deformation regime is the Saint Venant-Kirchhoff model, whose strain energy density function is given by Equation (4.10). The Lamé coefficients of the function, μ, λ, are related to Young's modulus, E, and Poisson's ratio, ν defined in Table 5.1, by the Equations (4.11, 4.12).

5.3.3.2 Mesh Physical Registration

This phase is executed every frame. For this purpose we exploit the information from the RGB-D camera. The colour information of the camera is used to project the 3D deformed mesh in the image while the depth information serves for obtaining a point cloud describing the surface of the tissue.

Keypoint selection

In addition to the keypoints discarded in the preprocessing step, the system must take into account that all keypoints are not visible during the online execution due to the point of view of the camera. Therefore, all the keypoints that are not visible must be discarded, whether deformation is being applied at that point or not.

Correspondence matching

The main goal of this step is to find the associations (also called correspondences), between the visible keypoints (defined in the tetrahedral mesh) with the input raw point cloud (obtained from the camera). For more details of the method, please refer to Leizea, Mendizabal, et al. (2015).

Finite Element Method (FEM) Simulation

Once the nodes of the simulation mesh have been matched to the deformed surface, they are used to control a dynamic simulation of the deformation of the solid. During this simulation, the nodes are displaced from their original position to the distance detected using the vision system. The simulation runs through a virtual time until it achieves the final configuration that we consider, i.e., until it represents the deformed state of the solid. The simulation is performed with a time step that has been computed previously and guarantees the stability of the semi-implicit Euler integrator that is employed.

5.4 Experiments

This section presents the experimental results of the proposed method. These experiments evaluate the performance (error estimation and computation time) and the adaptability of the system to different kind of models. To develop this set of experiments the robotic arm described above was used. Moreover, two cylindrical indenters were used to deform the tissue (Figure 5.2). These identers differ in size: one has a diameter of 15 mm and 45 mm length, while the smaller one has a diameter of 8 mm and a 36 mm length.

The hardware setup consists of an Intel Core 2-Quad Q9550 at 2.83 GHz and 4 GB of RAM equipped with a Kinect XBOX 360. Porcine *Kidney* and calf *Brain* models were used to evaluate the performance of the framework. Furthermore, for each of these two categories of models two different samples were used. The aim was to check with different samples, using the same material parametrisation and doing indentations in different areas, that the behaviour of our system was correct. For the *Brain* and *Kidney* categories, for each sample a force was applied in different areas: *Brain I*, *Brain II*, *Kidney I* and *Kidney II*. For the *Kidney II* sample, the smaller indenter was used in order to test the deformation with different tools. Figure 5.4 depicts the previous categorisation as well as the number of tetrahedrons of each model since it is a determining factor in the experimental results.

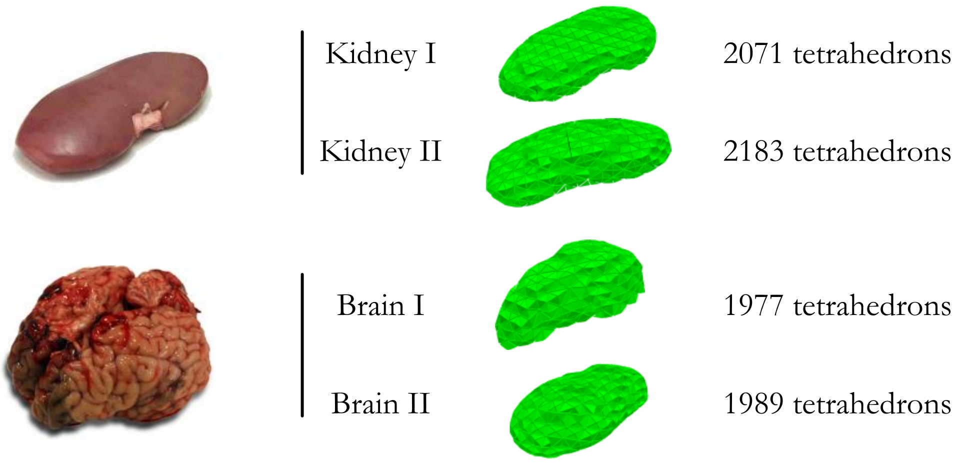

Figure 5.4: The real object (left) represented as tetrahedral mesh (right) for the FEM formulation.

5.4.1 Accuracy level

Two different techniques were used to validate the level of accuracy of the online FEM formulation. These consist in comparing the results obtained from the online FEM simulation with a simulation of the same experiment using Abaqus and with the 3D reconstruction obtained through a 3D scanner. Both techniques (Abaqus simulation and scanner reconstruction) are explained below.

Abaqus

The experiments were simulated in Abaqus. The stiffness of both tools was considered high enough compared to the indented tissues (ρ = 7850 kg/m^3, E = 3000000 Pa, ν=0.2) to model them as rigid solids. Deformable objects were modelled with the same mesh as the one used in the online FEM simulation. Materials were defined by the properties presented in Table 5.1.

The curve of the displacement versus time recorded by the robot in each experiment was imposed to the tool in the Abaqus simulation. Simulations were defined in a *Dynamic, Implicit* step with *Quasi-Newton* solution technique.

Deformed meshes from Abaqus and from online FEM simulation were compared. The error between both meshes was obtained calculating the point-to-point euclidean distance. Table 5.2 shows the values of this error for each material. The visual results of this comparison are displayed in Figure 5.5.

Table 5.2: The mean error, standard deviation and the maximum error (in mm) between the model obtained through online FEM simulation and Abaqus simulation.

	Mean error	**Std dev**	**Max error**
Kidney I	1.28	2.23	14.97
Kidney II	0.40	0.68	6.42
Brain I	1.09	1.10	7.24
Brain II	1.08	1.37	10.36

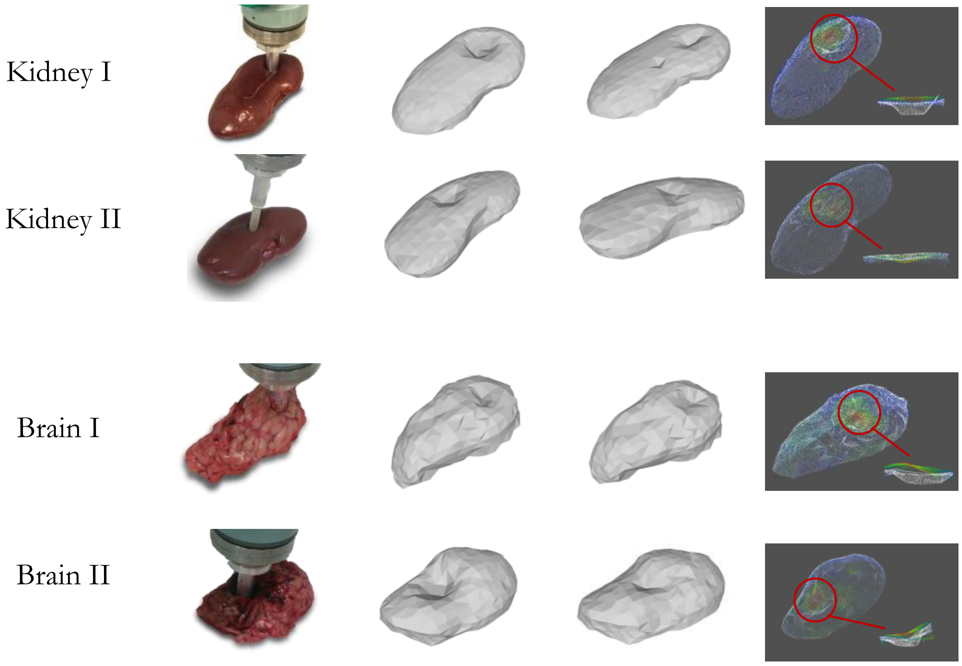

Figure 5.5: Comparison between FEM formulation and Abaqus simulation for different models. For each model: reconstructed mesh with Abaqus, FEM returned mesh and a colour map that represents the error between the solutions (extracted from CloudCompare).

Scanner

The evaluation of this error technique has different stages. First, a force was applied with the robotic arm and through the online FEM formulation, the deformation was computed. Simultaneously, the body was scanned by means of a 3D Sense Scanner during the deformation. The reconstruction of this scanner served as reference for the error estimation, that is, it was used as the ground truth. According to the technical specifications of the 3D Scanner reported by Cubify, the accuracy at 0.5 m depth resolution is 1 mm, and the spatial x/y resolution at 0.5 m is 0.9 mm.

Once the two regions of the two point clouds were selected, the open source CloudCompare software[1] was used to compute the error estimation. This is an application for managing and comparing 3D point clouds.

The mean errors (in mm) are displayed in Table 5.3 and Figure 5.6 shows the visual results of this experiment.

Table 5.3: The mean error, standard deviation and the maximum error (in mm) between online FEM simulation and scanner mesh.

	Mean error	**Std dev**	**Max error**
Kidney I	1.46	0.78	4.87
Kidney II	1.33	0.86	4.00
Brain I	2.26	2.00	11.68
Brain II	2.30	1.21	4.44

In conclusion, the error values are low enough to achieve a correct visual feedback. In these experiments the visual feedback consists in showing a gradient colour map to emphasize the degree of deformation. Figure 5.7 illustrates the visual results for each of the deformations applied to the four samples.

---

[1] Open source implementation of this method can be found in *http://www.danielgm.net/cc/*.

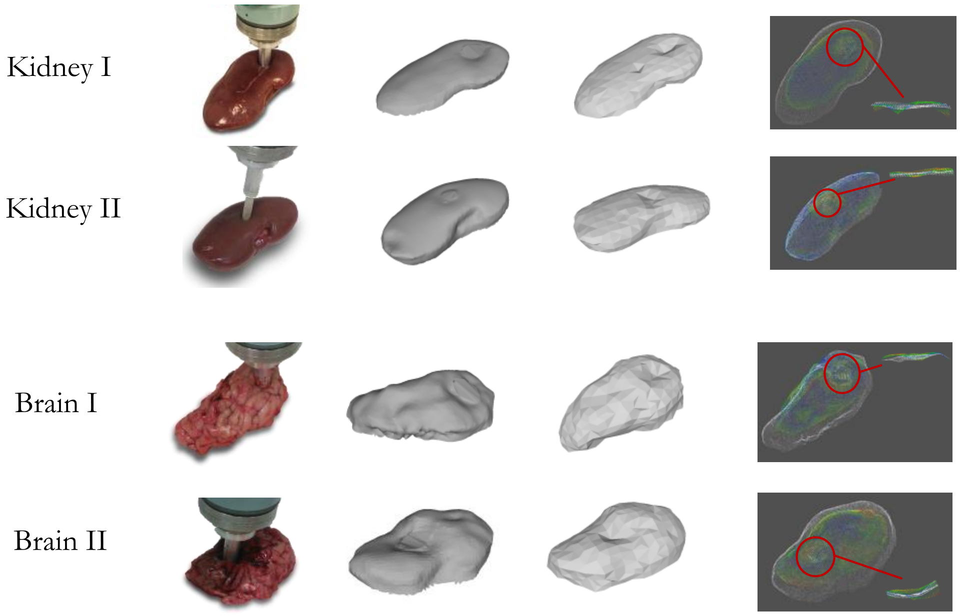

Figure 5.6: Comparison between FEM formulation and scanner reconstruction for different models. For each model: the mesh of the scanner, the mesh of FEM and a colour map that represents the error between both meshes (extracted from CloudCompare).

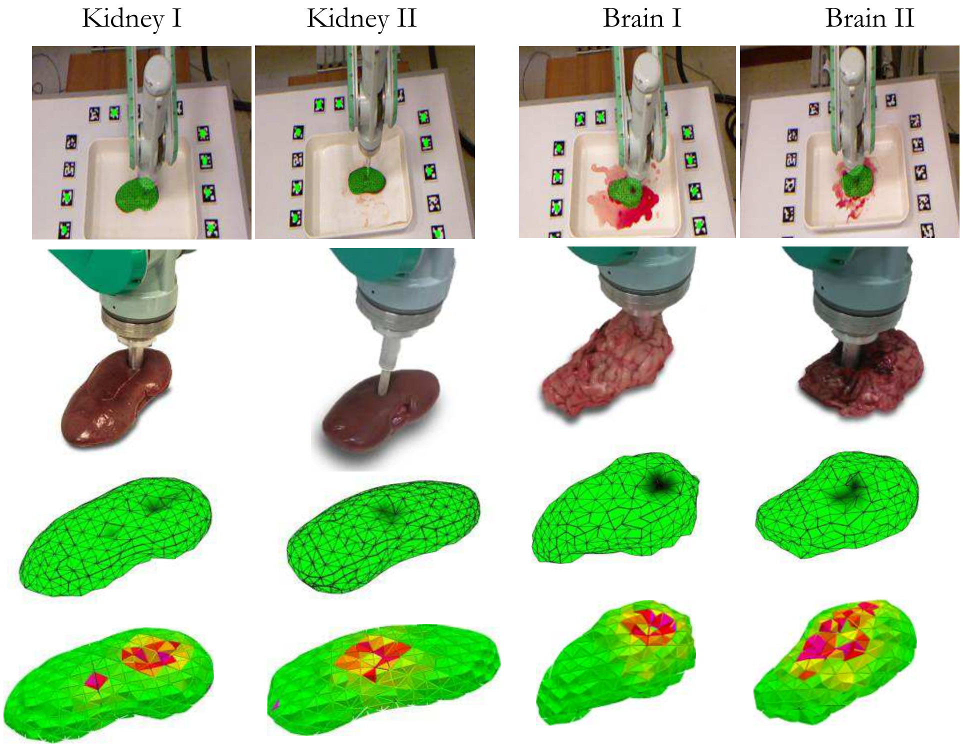

Figure 5.7: Visual feedback to surgeon when the soft tissue is deformed in a robot-assisted procedure. Two type of examples: kidneys and brains.

5.4.2 Computation time

This section shows the execution times of the object deformation module for all models. In this case, the computation times for the marker tracking system, as well as the matching step between the keypoints and the input point cloud, have not been taken into account. These results vary between 4 and 10 ms depending on the model. This computation time is not a bottleneck for the performance of the method, therefore, the attention has been focused on the physical module. More concretely, Figure 5.8 presents the execution times of the mesh physical simulation step, that is, the FEM physical simulation step. The process consisted in calculating 10 different times of the physical module and compute the mean time deleting the extreme values in order to discard the outliers. As it can be seen, the execution time varies from 14 to 40 ms depending on the model.

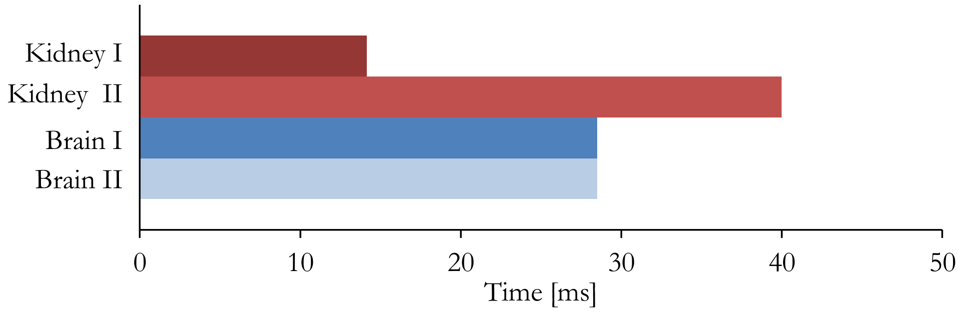

Figure 5.8: Execution times (in ms) of the FEM physical formulation for the different models.

These differences on the execution time are due to two reasons. Firstly, the execution time depends on the number of tetrahedrons of the model. As it might be expected, the larger the number of elements, the longer the execution time required. Secondly, the execution time depends on the time step set for each model. The smaller the time step, the longer the total execution time. Besides, the time step depends on the total simulation time of the experiment and on the mechanical properties of the material. The time step has been selected in each case in order to ensure the stability of each simulation.

5.5 Discussion

The deformation values obtained using the online FEM are smaller than those obtained by Abaqus software. This is due to the fact that, while the input of the Abaqus simulation is the displacement recorded by the robot, the input of the FEM is the displacement acquired by the cameras. However, these cameras do not get the exact displacements because of the occlusion of the tool or the material itself.

In the same way, it has been observed that deformations simulated with Abaqus are larger than those obtained by the scanner. This is because the scanner is not able to acquire the real deformation due to the occlusion of the tool. That is, the scanner acquires more accurate deformation than the cameras, but the deformation is less accurate than the one obtained with the simulation performed with Abaqus.

To improve the accuracy of the results higher density meshes could be employed. However, this will increase the computation time. Depending on the concrete application where the method is applied, a correct balance between precision and computation cost needs to be found, as it is the case in most real-time applications. The simulation approach is highly parallelizable an thus, the need for better accuracy could be solved using computers with a higher core count or with a GPU based implementations. However, as it can be seen in Table 5.2, the average errors obtained in the experiments with the current implementation are low enough to be considered valid to serve as basis for visual feedback in surgery, using Augmented Reality.

CHAPTER 6

CONCLUSIONS AND FUTURE WORK

6.1 Conclusions

This research work presents a methodology to characterise and model soft tissues for surgery simulation. It is important to understand the loads that take place in the tissue under the surgical procedure. That means that three key aspects must be kept in mind: *deformation mode*, *strain rate* and *deformation range*. The modelling (and therefore, also the characterisation) of the tissue depends entirely of these three aspects. And they are really important in order to improve the existing models. This may lead us to define models based on surgical procedures, rather than on the type of tissue, as it is usual. In other words, the same tissue or organ may have different models depending on the surgical procedure that represents the simulator.

In this thesis, simple shear deformation mode to strains up to 50% at quasi-static strain rates has been considered. However, other boundary conditions can be established by medical doctors and engineers depending on the characteristics of the surgical procedure to simulate.

6.1.1 Characterisation of soft tissues

The characterisation of soft tissues has been carried out in a parallel-plate rheometer. As a result, tissue characterisation has been performed under simple shear loads.

A methodology for the characterisation of the mechanical properties of soft tissues has been presented. The methodology has been carried out at large deformations and slow strain rates which are the boundary conditions established for surgical procedures.

Amplitude sweep is important in order to define the LVE range. Frequency sweep is not applied for the characterisation of the mechanical properties in this work. Controlled shear rate tests varying shear rate are not necessary in this case, since flow and viscosity functions are not used for the modelling of the presented elastic, hyperelastic and viscoelastic models. Besides, a risk of sliding and migration of the sample has been observed during these tests. On the contrary, constant shear rate tests are very recommended and useful for characterisation of the tissue. They provide strain-stress response until the imposed strain, without showing any problems of migration of the samples at slow strain rates. Finally, creep-recovery and relaxation tests are recommended for linear viscoelastic models, since the model can be easily fit at both responses. For QLV models, one of these test is enough in order to model the viscoelastic behaviour. In this case, for simplicity in mathematical formulation, relaxation test is recomended.

Porcine brain tissue has been characterised. The mechanical properties obtained under the established conditions are in the range of the values obtained in the literature. Besides, the obtained results contribute to the characterisation of porcine brain tissue, since tests at slow strain rates are rarely presented in the literature.

Agar gel has been characterised. Agar gels with low concentration of agar show similar mechanical properties to those of porcine brain tissue under the tested conditions.

6.1.2 Modelling of soft tissues

As the characterisation has been carried out in a parallel-plate rheometer, the modelling of the tested materials is defined at simple shear loads.

Different mechanical models have been studied. Elasticity has been studied, from linear elastic models to different hyperelastic models. Viscoelasticity has been studied through linear, quasi-linear viscoelastic and non-linear viscoelastic models.

Agar gel has been modelled with viscous models and linear viscoelastic models. Viscosity component of the mechanical behaviour of the agar gel has been modelled with non-newtonian models. Both of the presented models (Power-law and Bingham models) show an accurate representation of the viscous behaviour of agar. The modelling of agar gel has also been done using linear viscoelastic models. Experimental data from relaxation and creep-recovery tests has been used to this end. From all the linear viscoelastic models studied (Maxwell, Kelvin-Voigt, SLM, etc), the SLM models are the best choice to model an agar gel.

Porcine brain tissue has been modelled, taking into account the non-linearity and viscoelasticity of the tissue. Linear elastic model has been defined in order to study its limitations. To model the non-linear behaviour of the tissue, different hyperelastic models have been tested: reduced polinomial of 3^{rd} order, reduced polinomial of 4^{th} order and Lopez-Pamies model of 2^{nd} order. In order to model the viscoelastic behaviour of porcine brain tissue, QLV models have been defined. The elastic part of the QLV model has been defined with a linear elastic model and also with hyperelastic model.

For the modelling of porcine brain tissue under the considered loads, the next selection criterion has been concluded: If the strain rate is not taken into account and the maximum strains are around 10%, a linear elastic model turns out to be the best choice. Conversely, if strains are larger than 10%, hyperelastic models would cover the requirements. However, if the strain rate is taken into account, a QLV model with a linear elastic part is the best choice for strains up to 10%. Whereas, for larger strains, QLV with hyperelastic component should be used. In the case that all requirements should be met, i.e., strain rate effect, large strains and a very high accurate simulation are required, the model should be based on a non-linear viscoelastic model. However, due to the complexity of the implementation of these models, the execution time of the simulation can easily grow beyond the limits required to achieve a real-time simulation. If these models are used, the computation should have less strict time requirements.

Different models have been analysed under other loads. If the tissue is subjected to an instantaneous force and it is let without any restriction, the linear elastic, hyperelastic and QLV models has an oscillatory response as it is expected. The main difference lies in purely elastic and viscoelastic models. Both, linear elastic and hyperelastic models have similar behaviour and they continue oscillating over time. Conversely, the two QLV models (with linear and hyperastic parts) show a considerable damping. Differences between these two models are imperceptible.

6.1.3 Real-time application

A complete framework for tracking and registering deformations of objects using a physics-based formulation has been presented. The proposed approach is able to provide surgeons with a visual feedback of the deformation of the tissue during robotically-assisted surgical procedures.

Even in zones where there are occlusions with the robot arm and the camera does not measure directly the tissue deformation, a FEM model can complete the missing deformation information by simulating the volume of an organ. This also helps obtaining the stresses of the organ. In this way, a surgeon can establish a stress range in which the tissue is subjected to mechanical or functional failure. The visual feedback helps the surgeon to avoid this range of stress on the tissue.

The developed application has been applied to two ex-vivo organs: calf brain and porcine kidney. Both organs have been modelled with a Saint-Venant Kirchhoff model. The characterisation and modelling of the soft tissue have been appropriate for the requirements of realism and interactive computation times. However, in order to improve accuracy, other hyperelastic models can be used, as well as viscoelastic ones. Nevertheless, in this application, tissue is subjected to indentation loads. Therefore, if hyperelastic models are used, an additional characterisation of the tissue under indentation loads is recommended.

6.2 Future work

There are three main factors to take into account in the characterisation and modelling of soft tissues for surgery simulation: the load mode applied to the tissue, the velocity at which the deformation occurs and the strain range to be modelled. However, this data remains unknown to medical doctors and engineers. It would be interesting to study the surgical procedure that aims to be simulated in order to be able to establish these boundary conditions. In other words, it is interesting to study how the tissue actually deforms during surgery and to measure the maximum strains that the tissue is being subjected to during a surgical procedure.

In this thesis, characterisation of the tissue has been performed under simple shear loads, consequently, the studied modelling is valid under this kind of loads. It is interesting to study how the models defined from shear tests behave at other deformation modes. Taking advantage of the experiments perfomed with the robot, presented in Chapter 5, some shear models have been studied under indentation loads. However, due to the lack of conclusive results, they have not been included in this thesis.

Calf brain and porcine kidney tissues are characterised in the rheometer (CSR test at 0.0005 s^{-1}) and modelled with hyperelastic RP3 models. These models are simulated in Abaqus at the same indentation loads perfomed by the robot. RP3 models fit experimental shear curve accurately and they underestimate the tissue deformation under indentation loads. However, further research is required in order to determine the limit of the models characterised at simple shear loads.

It could be possible to find a hyperelastic model that represents the soft tissue at different load modes, at least at small deformations. More research is required to fit the same model at different load modes and at large strains. Besides, it is possible to define a single model at different load modes, fitting the model to experimental data obtained from different load tests, for example at shear and indentation loads. However, in that way, accuracy may decrease when simulating the mechanical behaviour under a single load.

The characterisation of porcine brain tissue has been performed ex-vivo. However, some differences may exist between in-vivo and ex-vivo tissue. It would be interesting to study how much the mechanical properties characterised ex-vivo differ from the values obtained from in-vivo tests, in order to asses the validity of the applied ex-vivo method.

Similarly, porcine brain tissue has been chosen as a surrogate for human brain tissue. It would be convenient to quatify the error made having characterised a porcine tissue instead of human tissue.

Regarding the characterisation of soft tissues, several simplifications have been made in this thesis, taking the objective application into account.

Brain has been considered a homogeneous organ. Actually, grey matter and white matter may have different values of mechanical properties.

Similarly, different sections of brain (i.e., lobes, cerebellum, corpus callosum or thalamus) may also present different values of these properties. Although, the approach of homogeneneity is considered valid for the purpose of this thesis, it could be interesting to study the mechanical behaviour of different parts of the brain.

In addition, brain tissue has been considered isotropic. Currently, the anisotropy of brain tissue remains under research. Some researches concluded that white matter of brain tissue appears to be mechanically transversely isotropic with respect to the dominant axonal fiber direction, while other studies did not find clearly anisotropic material properties for the tested brain tissue. Further research is required in order to characterise the brain tissue. Anisotropy of tissues can be modelled with hyperelastic models, including other strain invariants in their strain energy density function.

It is well known that viscoelastic materials show elastic hysteresis. In this thesis, it has been considered that hysteresis is not a fundamental effect to be modelled in surgery simulations, since it is unlikely that soft tissues would be subjected to load-unload cycles in surgical procedures. Similarly, the temperature effect into the mechanical properties of soft tissues is not characterised and modelled in this thesis, since in has been considered that the temperature remains almost constant during surgical procedures. However, if the modelling of hysteresis and temperature effect is required, the rheometer enables the characterisation of the elastic hysteresis, as well as the temperature effect.

In the modelling of mechanical properties of the brain, only the tissue has been characterised and modelled. However, some boundary conditions can be important in the brain modelling. Some authors state that more research is needed, especially into the appropriate modelling of the interface between the brain and the skull. Miller, Chinzei, et al., 2000 affirmed that this direction of research, is at least equally important to the investigation of the mechanical properties of brain internal structures themselves.

It is also interesting to continue studying the mechanical behaviour of agar gels. According to the results, these gels represent the mechanical behaviour of porcine brain tissue quite accurately. More testing is required to obtain a more extensive comparison between gels and the soft tissue, in order to develop agar gels that can be used as surrogate for brain tissue in medical applications.

Some hyperelastic material models are unstable under certain range of deformation or under certain modes of deformations. This can be due to limitations of the hyperelastic models themselves, or due to instabilities caused by Abaqus finite element analysis. It would be convenient to study these limitations of the models, if a unique model is required for different deformation modes.

In regards to the used models, it would be adequate to implement the selected hyperelastic and viscoelastic models in a real-time FEM platform. In that way, a discussion or a selection criterion can be performed about the most appropriate model, taking into account not only the accuracy of the models but also the execution time required for their simulation.

Finally, the models implemented in the simulation should be tested by surgeons. They could provide validation about the realism of the mechanical behaviour of soft tissue models. Although it would be a qualitative validation, it can be a helpful feedback, in order to better understand the requirements of the medical doctors about surgery simulation. This validation could be done by usability and immersion tests.

APPENDIX A

PUBLICATIONS

This appendix includes the front page of the articles that have already been published by the author of this thesis in scientific journals and conferences.

Journals

Leizea, I., Mendizabal, A., Alvarez, H., Aguinaga, I., Sánchez, E., and Borro, D. (2015). "Tracking of deformable objects based on a visual approach and physics simulation for robot-assisted surgery". In: *IEEE Computer Graphics and Applications.*

Mendizabal, A., Aguinaga, I., and Sánchez, E. (2015). "Characterisation and modelling of brain tissue for surgical simulation". In: *Journal of the Mechanical Behavior of Biomedical Materials* 45, pages 1–10.

Conferences

Mendizabal, A., Landeira, M., Aguinaga, I., and Sánchez, E. (2012). “Soft Tissue Equivalent Phantom Materials: Experiments on Mechanical Properties of Agar/Gelatin/PPG Based Phantoms”. In: *CASEIB Congreso Anual de la Sociedad Española de Ingeniería Biomédica*. 3, pages 3–6.

Tracking of deformable objects based on a visual approach and physics simulation for robot-assisted surgery

Ibai Leizea, Ainhitze Mendizabal, Hugo Álvarez, Iker Aguinaga, Emilio Sánchez and Diego Borro *Member IEEE*

Abstract—This paper presents a visual tracking system for deformable objects used with a robot-assisted surgical system. The system is capable of capturing the deformation exerted by the robot using Computer Vision in real time, despite the occlusions produced by the robotic system itself. The information captured enables new assistance approaches to help surgeons during procedures, in particular Augmented Reality applications. The tracking algorithm is helped by a fast and accurate physically-based biomechanical model of the object, together with a visual tracking approach designed to properly simulate the model.

This method has been tested with three different objects in ex-vivo conditions, to evaluate the level of accuracy and computation requirements of the proposed system. The deformations obtained from the experiments have been compared with the theoretical results obtained by finite element analysis obtained using the Abaqus software package. The results obtained provide an accurate visual representation of the deformed solid.

Index Terms—Visual tracking, robotics, finite element method, material characterization.

◆

1 INTRODUCTION

The use of robotic devices in medicine and more specifically in the surgical field entails a remarkable improvement in the delivery of healthcare services. Nowadays, robotic devices and computer-assisted technologies are included as a means of guidance, diagnosis, verification and general assistance during the performance of a surgical intervention [1].

However, the use of robotic devices in surgery creates new challenges that must be overcome for their successful deployment. A robot acting on a tissue exerts a force and produces deformations over which the surgeon has no direct feedback. The tracking of the deformation of the organs is required for assistive technologies such as Augmented Reality, for example to support the surgeon by a visual feedback of the deformations that are taking place on the tissues, or to support the surgeon by locating the position of a malignancy to be removed from an organ. In most cases, the inclusion of sensors to track the position of the organs of the patient is not feasible. Thus, the use of alternative approaches such as Computer Vision techniques has become a real need to solve this kind of problem.

Nevertheless, the very presence of the robot produces occlusions that limit how much information can be obtained using only Computer Vision. The combination of Computer Vision with a suitable physical simulation can be used to reduce the missing information. In this case, the accuracy required for the surgical simulations remains important. In contrast to deformable models used in video games and animations, the purpose of soft tissue models in medical simulation is to model realistically the behaviour of biological tissues. Consequently, the simulation of the deformation of the tissue should be controlled using real material parameters. Thus, these parameters should be obtained from biomechanics experiments instead of intuitively adjusted parameters. However, in robotic guidance and surgery assistance systems not only accuracy is essential, but also computational performance must be taken into account, in order to provide a fast enough visual feedback to the surgeon. Therefore, in this application it is critical to obtain a compromise between accuracy and computational cost. Being able to provide surgical realism at interactive rates of simulation is one of the most challenging problem in robot surgical assistance systems [2].

This paper proposes a novel visual tracking method based on physical simulation. This procedure is capable of obtaining the deformation produced by a robotic system on patient tissues, and therefore, it obtains the basic information to provide assistance and guidance to surgeons using visual or haptic feedback. Providing surgeons with the deformation of an organ is very useful. Normally, the surgeons do not have an idea of the stress to which the tissue is subjected. The human eye can not quantify the functional or mechanical damage of the tissue. Surgeons judge the damage range based on their experience. In that way, this method provides surgeons with a visual feedback of the deformation that the tissue is suffering. Even, in zones where there are occlusions and the camera does not measure directly the tissue deformation, a FEM model is able to obtain the complete deformation by simulating the volume of an organ and also the missing surfaces. This also helps obtaining the stress of the organ. In this way, surgeon can establish a stress range in which the tissue is subjected to

---

The authors are with the Applied Mechanics department, CEIT-IK4 and TECNUN, Manuel Lardizabal 15, San Sebastian 20018, Spain.
E-mail: dborro@ceit.es.

JOURNAL OF THE MECHANICAL BEHAVIOR OF BIOMEDICAL MATERIALS 45 (2015) 1–10

ELSEVIER

Available online at www.sciencedirect.com

ScienceDirect

www.elsevier.com/locate/jmbbm

Research Paper

Characterisation and modelling of brain tissue for surgical simulation

A. Mendizabal, I. Aguinaga, E. Sánchez*

Department of Applied Mechanics, CEIT, Donostia-San Sebastián, 20018, Spain

ARTICLE INFO

Article history:
Received 27 October 2014
Received in revised form
12 January 2015
Accepted 21 January 2015
Available online 30 January 2015

ABSTRACT

Interactive surgical simulators capable of providing a realistic visual and haptic feedback to users are a promising technology for medical training and surgery planification. However, modelling the physical behaviour of human organs and tissues for surgery simulation remains a challenge. On the one hand, this is due to the difficulty to characterise the physical properties of biological soft tissues. On the other hand, the challenge still remains in the computation time requirements of real-time simulation required in interactive systems. Real-time surgical simulation and medical training must employ a sufficiently accurate and simple model of soft tissues in order to provide a realistic haptic and visual response.

This study attempts to characterise the brain tissue at similar conditions to those that take place on surgical procedures. With this aim, porcine brain tissue is characterised, as a surrogate of human brain, on a rotational rheometer at low strain rates and large strains. In order to model the brain tissue with an adequate level of accuracy and simplicity, linear elastic, hyperelastic and quasi-linear viscoelastic models are defined. These models are simulated using the ABAQUS finite element platform and compared with the obtained experimental data.

1. Introduction

Surgical simulations with a realistic visual and haptic feedback are a promising technology for medical training and surgical planning. In addition, such simulators help in optimising surgical tool design and understanding tissue injury mechanisms and damage thresholds (Misra et al., 2010). The Finite Element Method (FEM) has been widely used for surgical simulations since it incorporates real physical material parameters, and therefore, it allows modelling tissue properties more accurately than other approaches such as mass-spring models. However, there is no agreement in the literature on the most suitable material models required for surgical simulation. Model selection is often a very subjective process; different modellers choose different models to describe the same phenomenon (Miller et al., 2010). A key question in modelling tissue behaviour for simulation is the level of accuracy required. For surgical simulation of biological tissues, models must be simple enough to solve a broad range of problems, but complete enough to realistically describe the behaviour under a variety of load conditions

---

*Corresponding author.

E-mail addresses: amendizabal@ceit.es (A. Mendizabal), iaguinaga@ceit.es (I. Aguinaga), esanchez@ceit.es (E. Sánchez).

http://dx.doi.org/10.1016/j.jmbbm.2015.01.016
1751-6161/

Soft Tissue Equivalent Phantom Materials: Experiments on Mechanical Properties of Agar/Gelatin/PPG Based Phantoms

A. Mendizabal Dones[1], M.A. Landeira Freire[1], I. Aguinaga Hoyos[1], E. Sánchez Tapia[1]

[1] CEIT, TECNUN University of Navarra, San Sebastián, España, {amendizabal, mlandeira, iaguinaga, esanchez}@ceit.es

Abstract

The aim of this research study is to present some different material blends that are suitable for building a physical model that accurately mimics the dynamic mechanical properties of brain tissue. These materials can act as a replacement for actual biological tissue samples for a wide variety of experimental procedures.

The experimental testing setup has been defined for parallel plates oscillatory shear testing, considering both amplitude and frequency sweeps. Biological tissue samples of porcine brain were tested along with several phantoms, built from the aforementioned materials blends.

Results obtained from experiments show that the proposed blends adequately simulate the sought brain properties, though further composition refinement must be done.

1. Introduction

Of all body parts, the head is the most vulnerable, but there is still a huge lack of knowledge in the biomechanics of this area. Nowadays, there is a need to analyze mechanical properties of human brain in order to advance in the field of neurology, working on the diagnosis of neurodegenerative diseases and in the development of neurosurgery simulation tools.

Palpation is a basic and effective clinical examination tool that has been used for centuries. In engineering terms, palpation assesses the tendency of tissue to resist deformation, a physical property called elastic modulus. However, brain tissue or other organs are not accessible to the palpating hand. Magnetic resonance elastography (MRE) is a non-invasive technique that may be a tool for the detection of abnormal stiffness differences in soft tissues, analyzing the physical properties as elasticity of human tissues. A change in elasticity can often represent a pathological change in the tissue and may provide information for the detection of tumors and for the diagnosis of neurodegenerative diseases as Multiple Sclerosis or Alzheimer. However, it is too early to claim limits in the detection ability of MRE. [1], [2], [3].

Valid quantitative measurements of the elastic modulus of cerebral tissue are also of interest in biomechanical studies of neurosurgery simulation, vehicle safety, brain trauma or ballistic injury [3]. In addition to this, a phantom (physical model of brain tissue or other organ) may be useful to develop a surgical medical training or to calibrate MRE equipment.

Although a large collection of data is available, studies on the characterization of brain properties by different laboratories using different testing protocols yield a tremendously wide range of results, already for the linear viscoelastic properties. In this work, biological brain tissue is tested with the aim of knowing the values of mechanical properties as shear modulus. Some gels were prepared and tested, in order to develop a phantom whose mechanical properties are similar to the ones measured in the brain tissue.

This paper begins with the presentation of the theory of the mechanical behavior of viscoelastic materials. Afterwards, several tests with brain tissue are collected from the literature. In the third section, prior research studies with brain phantoms are discussed. This is followed by the materials and methods used to analyze biological samples and to carry out and test the gel samples. Finally, the obtained results of the shear test are presented, as well as a final discussion and conclusions.

2. Mechanical Testing Of Viscoelastic Materials

Oscillatory Shear Testing (OST) is the most commonly used in vitro technique to characterize dynamic mechanical properties of all kind of viscoelastic materials [4]. It is possible to perform controlled shear strain or controlled shear stress tests. In the first case, a sinusoidal strain is imposed on the viscoelastic material, resulting in a sinusoidal stress of the same frequency but phase-shifted ahead by an angle δ

$$\gamma(t) = \gamma_A \cdot \sin(\omega t) \Rightarrow \tau(t) = \tau_A \cdot \sin(\omega t + \delta) \quad \textbf{(1)}$$

Similarly, for controlled shear stress, the input is a sinusoidal stress, resulting on a sinusoidal strain applied to the material, but phase-shifted ahead by δ

$$\tau(t) = \tau_A \cdot \sin(\omega t) \Rightarrow \gamma(t) = \gamma_A \cdot \sin(\omega t + \delta) \quad \textbf{(2)}$$

The complex viscoelastic modulus, G^*, is defined (3) as the ratio between shear stress and shear strain amplitudes.

$$G^* = {}^{\tau_A}/_{\gamma_A} \quad \textbf{(3)}$$

From (3) two other material constants are defined: the storage modulus, G′, and the loss modulus, G″. The storage modulus is a measure of the deformation energy stored by the sample during the shear process and represents the elastic behavior of a test material. The loss modulus is a measure of the deformation energy used up by the sample during the shear process and represents the

APPENDIX B

SPECIFICATIONS OF ANTON-PAAR MCR 301

Table B.1 resumes the specifications of the testing device used for the characterisation of soft tissues, the rheometer Anton-Paar MCR 301.

Table B.1: Specifications of the Anton-Paar MCR 301.

Technical Data	**Unit**	**Physica MCR 301**
Min. torque rotation	μNm	0.05
Min. torque oscillation	μNm	0.01
Max. torque	mNm	200
Torque resolution	nNm	0.1
Angular deflection	μrad	0.1 to ∞
Angular resolution	μrad	0.01
Min. speed	1/min	10^{-7}
Max. speed	1/min	3000
Min. angular frequency	rad/s	10^{-5}
Max. angular frequency	rad/s	628
Normal force range	N	0.01-50
Normal force resolution	N	0.002
Temperature range	°C	-150 to 1000

BIBLIOGRAPHY

Ahn, B. and Kim, J. (2009). "Efficient soft tissue characterization under large deformations in medical simulations". In: *International Journal of Precision Engineering and Manufacturing* 10.4, pages 115–121.

Amin, A., Wiraguna, S., Bhuiyan, A., and Okui, Y. (2006). "Hyperelasticity Model for Finite Element Analysis of Natural and High Damping Rubbers in Compression and Shear". In: *Journal of engineering mechanics* January.

Arbogast, K. and Margulies, S. (1998). "Material characterization of the brainstem from oscillatory shear tests". In: *Journal of biomechanics* 31.9, pages 801–7.

Athanasiou, K. A. and Natoli, R. M. (2008). *Introduction to Continuum Biomechanics.* Volume 3. 1. Morgan & Claypool Publishers, pages 1–206.

Barnes, H., Hutton, J., and Walters, K. (1989). *An introduction to rheology.* Elsevier Science.

Basdogan, C., Ho, C.-H., and Srinivasan, M. A. (2001). "Virtual Environments for Medical Training: Graphical and Haptic Simulation of Laparoscopic Common Bile Duct Exploration". In: *ASME Transactions on Mechatronics* 6.3, pages 269–285.

Belinha, J. (2014). *Meshless Methods in Biomechanics.*

Bercoff, J., Pernot, M., Tanter, M., and Fink, M. (2004). “Monitoring Thermally-Induced Lesions with Supersonic Shear Imaging”. In: *Ultrasonic Imaging* 26.2004, pages 71–84.

Bercoff, J., Muller, M., Tanter, M., and Fink, M. (2003). “Study of viscous and elastic properties of soft tissues using supersonic shear imaging”. In: *IEEE Ultrasonics Symposium*, pages 925–928.

Bilston, L., Liu, Z., and Phan-Thien, N. (2001). “Large strain behaviour of brain tissue in shear: Some experimental data and differential constitutive model”. In: *Biorheology* 38.4, pages 335–45.

Brands, D., Bovendeerd, P., Peters, G., Wismans, J., Paas, M., and Bree, J. van (1999). “Comparison of the dynamic behavior of the brain tissue and two model materials”. In: *Proceedings of the 43rd Stapp Car Crash Conference, SAE 99SC21*, pages 57–64.

Brands, D., Peters, G., and Bovendeerd, P. (2004). “Design and numerical implementation of a 3-D non-linear viscoelastic constitutive model for brain tissue during impact”. In: *Journal of Biomechanics* 37.1, pages 127–134.

Bronshtein, T., Au-Yeung, G. C. T., Sarig, U., Nguyen, E. B.-V., and Mhaisalkar, P. S. (2013). “A Mathematical Model for Analyzing the Elasticity, Viscosity, and Failure of Soft Tissue: Comparison of Native and Decellularized Porcine Cardiac Extracellular Matrix for Tissue Engineering”. In: *Tissue Engineering* 19.8, pages 620–630.

Brown, J., Sorkin, S., Latombe, J.-C., Montgomery, K., and Stephanides, M. (2002). “Algorithmic tools for real-time microsurgery simulation”. In: *Medical image analysis* 6.3, pages 289–300.

Calvo, B., Sierra, M., Grasa, J., Muñoz, M., and Peña, E. (2014). "Determination of passive viscoelastic response of the abdominal muscle and related constitutive modeling: stress-relaxation behavior". In: *Journal of the mechanical behavior of biomedical materials* 36, pages 47–58.

Campus, K. and Engineering, F. (2005). "New Tissue Mimicking Materials for Ultrasound Phantoms". In: 00.c, pages 1664–1667.

Carter, F., Frank, T., Davies, P., McLean, D., and Cuschieri, A. (2001). "Measurements and modelling of the compliance of human and porcine organs". In: *Medical image analysis* 5, pages 231–236.

Celigüeta, J. T. (2009). *Análisis de estructuras con no linealidad geométrica.*

Chaves, E. W. (2013). *Notes on Continuum Mechanics.* Springer.

Cheng, S., Clarke, E., and Bilston, L. (2008). "Rheological properties of the tissues of the central nervous system: A review". In: *Medical engineering & physics* 30.10, pages 1318–37.

Chunping, G. (2007). "Finite element modelling of the human brain and application in neurosurgical procedures". PhD thesis. University of Singapore.

Clatz, O., Delingette, H., Talos, I.-f., Golby, A. J., Kikinis, R., Jolesz, F. A., Ayache, N., and Warfield, S. K. (2007). "Robust Non-Rigid Registration to Capture Brain Shift from Intra-Operative MRI". In: *IEEE Trans Med Imaging* 24.11, pages 1417–1427.

Comas, O., Taylor, Z. A., Allard, J., Ourselin, S., Cotin, S., and Passenger, J. (2008). "Efficient nonlinear FEM for soft tissue modelling and its GPU implementation within the open source framework SOFA". In: *Lecture Notes in Computer Science* 5104, pages 28–39.

Cotin, S., Delingette, H., and Ayache, N. (2000). "A hybrid elastic model for real-time cutting, deformations, and force feedback for surgery training and simulation". In: *The Visual Computer Journal* 16, pages 437–452.

Darvish, K. and Crandall, J. (2001). "Nonlinear viscoelastic effects in oscillatory shear deformation of brain tissue". In: *Medical engineering & physics* 23.9, pages 633–45.

Delingette, H., Cotin, S., and Ayache, N. (2004). "A Hybrid Elastic Model allowing Real-Time Cutting, Deformations and Force-Feedback for Surgery Training and Simulation". In: *The Visual Computer Journal.*

Dey, A., Basudhar, P., and ASCE, A. (2010). "Applicability of burger model in predicting the response of viscoelastic soil beds". In: Gsp 199, pages 2611–2620.

Dogan, F. and Serdar Celebi, M. (2010). "Real-time deformation simulation of non-linear viscoelastic soft tissues". In: *Simulation: Transactions of the Society of Modeling and Simulation International* 87.3, pages 179–187.

Felippa, C. and Haugen, B. (2005). "A unified formulation of small-strain corotational finite elements: I. Theory". In: *Computer Methods in Applied Mechanics and Engineering* 194.21-24, pages 2285–2335.

Fernández Fernández, P., Lamela Rey, M., and Fernández Canteli, A. (2007). "Caracterizacion viscoélastica del disco de la articulación témporomandibular de bovinos". In: *Anales de la mecánica de fractura* 1, pages 321–326.

Ferrant, M., Warfield, S. K., Nabavi, A., Jolesz, F. A., and Kikinis, R. (2001). “Registration of 3D IntraoperativeMR Images of the Brain Using a Finite Element Biomechanical Model”. In: *IEEE Trans Med Imaging* 20.12, pages 1384–97.

Franceschini, G., Bigoni, D., Regitnig, P., and Holzapfel, G. (2006). “Brain tissue deforms similarly to filled elastomers and follows consolidation theory”. In: *Journal of the Mechanics and Physics of Solids* 54.12, pages 2592–2620.

Fromageau, J., Gennisson, J.-L., Schmitt, C., Maurice, R. L., Mongrain, R., and Cloutier, G. (2007). “Estimation of polyvinyl alcohol cryogel mechanical properties with four ultrasound elastography methods and comparison with gold standard testings”. In: *IEEE transactions on ultrasonics, ferroelectrics, and frequency control*. Volume 54. 3, pages 498–509.

Fung, Y. (1981). *Biomechanics. Mechanical Properties of Living Tissues*. Second Edi. Springer.

Gao, C., H Tay, F., and Nowinski, W. (2005). “A finite element method based deformable brain atlas suited for surgery simulation”. In: *International Conference of the IEEE Engineering in Medicine and Biology Society*. Volume 4, pages 4337–40.

Gao, C., Tay, F. E. H., and Nowinski, W. L. (2006). “Modelling of the human brain with detailed anatomy for numerical simulation of surgical interventions”. In: *Journal of Physics: Conference Series* 34, pages 985–989.

Gao, Z., Lister, K., and Desai, J. P. (2010). “Constitutive modeling of liver tissue: experiment and theory”. In: *Annals of biomedical engineering* 38.2, pages 505–16.

Geris, L. (2013). *Computational Modeling in Tissue Engineering*. Springer.

Hamarneh, G., Amir-Khalili, A., Nosrati, M. S., Figueroa, I., Kawahara, J., Al-Alao, O., Peyrat, J.-M., Abi-Nahed, J., Al-Ansari, A., and Abugharbieh, R. (2014). “Towards multi-modal image-guided tumour identification in robot-assisted partial nephrectomy”. In: *Middle East Conference on Biomedical Engineering*, pages 159–162.

Haouchine, N. and Dequidt, J. (2014). “Single View Augmentation of 3D Elastic Objects”. In: *International Symposium on Mixed and Augmented Reality*. September, pages 229–236.

Haouchine, N., Dequidt, J., Peterlik, I., Kerrien, E., Berger, M.-O., and Cotin, S. (2013). “Image-guided simulation of heterogeneous tissue deformation for augmented reality during hepatic surgery”. In: *IEEE International Symposium on Mixed and Augmented Reality*. Volume 2013. Ieee, pages 199–208.

Hollenstein, M., Bajka, M., Röhrnbauer, B., Badir, S., and Mazza, E. (2012). “Measuring the In Vivo Behavior of Soft Tissue and Organs Using the Aspiration Device”. In: *Soft tissue biomechanical modeling for computer assisted surgery*, pages 201–228.

Holzapfel, G. (2000). *Nonlinear Solid Mechanics: A continuum Approach for Engineering*. Edited by Wiley.

Horgan, C. O. and Murphy, J. G. (2009). “Simple Shearing of Incompressible and Slightly Compressible Isotropic Nonlinearly Elastic Materials”. In: *Journal of Elasticity* 98.2, pages 205–221.

Horgan, C. O. and Murphy, J. G. (2010). “Simple shearing of soft biological tissues”. In: *Proceedings of the Royal Society A: Mathematical, Physical and Engineering Sciences* 467.2127, pages 760–777.

Hrapko, M. (2008). “Mechanical behaviour of brain tissue for injury prediction: characterisation and modelling”. PhD thesis.

Hrapko, M., Van Dommelen, J., Peters, G., and Wismans, J. (2006). “The mechanical behaviour of brain tissue: large strain response and constitutive modelling”. In: *Biorheology* 43.5, pages 623–36.

Hrapko, M., Van Dommelen, J., Peters, G., and Wismans, J. (2008a). “Characterisation of the mechanical behaviour of brain tissue in compression and shear”. In: *Biorheology* 45, pages 663–676.

Hrapko, M., Van Dommelen, J., Peters, G., and Wismans, J. (2008b). “The influence of test conditions on characterization of the mechanical properties of brain tissue”. In: *Journal of biomechanical engineering* 130.3, page 031003.

Irving, G., Teran, J., and Fedkiw, R. (2005). “Tetrahedral and Hexahedral Invertible Finite Elements”. In: *Elsevier Science* March 2005.

Jiang, Y., Li, G.-Y., Qian, L.-X., Hu, X.-D., Liu, D., Liang, S., and Cao, Y. (2015). “Characterization of the nonlinear elastic properties of soft tissues using the supersonic shear imaging (SSI) technique: Inverse method, ex vivo and in vivo experiments”. In: *Medical image analysis* 20.1, pages 97–111.

Jin, X., Zhu, F., Mao, H., Shen, M., and Yang, K. H. (2013). “A comprehensive experimental study on material properties of human brain tissue”. In: *Journal of biomechanics* 46.16, pages 2795–801.

Kaster, T., Sack, I., and Samani, A. (2011). “Measurement of the hyperelastic properties of ex vivo brain tissue slices”. In: *Journal of biomechanics* 44.6, pages 1158–63.

Kato, H., Kuroda, M., Yoshimura, K., Yoshida, A., Hanamoto, K., Kawasaki, S., Shibuya, K., and Kanazawa, S. (2005). "Composition of MRI Phantom Equivalent to Human Tissue". In: *Journal of Medical Physics* 32, pages 3199–208.

Kauer, M., Vuskovic, V., Dual, J., Szekely, G., and Bajka, M. (2002). "Inverse finite element characterization of soft tissues". In: *Medical Image Analysis* 6, pages 275–287.

Kawabata, K., Waki, Y., Matsumura, T., and Umemura, S. (2004). "Tissue mimicking phantom for ultrasonic elastography with finely adjustable elastic and echographic properties". In: *Ultrasonics Symposium IEEE.* Volume 2, pages 1502–1505.

Keeve, E., Girod, S., Kikinis, R., and Girod, B. (1998). "Deformable modeling of facial tissue for craniofacial surgery simulation". In: *Computer aided surgery: official journal of the International Society for Computer Aided Surgery* 3.5, pages 228–38.

Kerdok, A. (2006). "Characterizing the Nonlinear Mechanical Response of Liver to Surgical Manipulation". PhD thesis. Harvard University.

Kim, J., Muniyandi, M., Kim, H., and Srinivasan, M. A. (2004). "Haptics in Minimally Invasive Surgical Simulation". In: *IEEE Computer Society* April, pages 56–64.

Kim, J. and Srinivasan, M. A. (2005). "Characterization of viscoelastic soft tissue properties from in vivo animal experiments and inverse FE parameter estimation". In: *International Conference on Medical Image Computing and Computer-Assisted Intervention.* Volume 8. Pt 2, pages 599–606.

Kyriacou, S., Mohamed, A., Miller, K., and Neff, S. (2002). “Brain mechanics for neurosurgery: modeling issues”. In: *Biomechanics and modeling in mechanobiology* 1.2, pages 151–64.

Laksari, K., Shafieian, M., and Darvish, K. (2012). “Constitutive model for brain tissue under finite compression”. In: *Journal of biomechanics* 45.4, pages 642–6.

Landeira, M. (2014). “Development of a General Purpose for Performance of Surgical Procedures”. PhD thesis. Tecnun, University of Navarra.

Landeira, M., Sánchez, E., Tejada, S., and Díez, R. (2014). “Desarrollo e implementación de una estrategia de gestión de singularidades para un sistema robótico redundante cooperativo destinado a la asistencia en intervenciones quirúrgicas”. In: *Revista Iberoamericana de Automatica e Informatica industrial* 00, pages 1–12.

Lapeer, R., Gasson, P., and Karri, V. (2011). “A hyperelastic finite-element model of human skin for interactive real-time surgical simulation”. In: *IEEE transactions on bio-medical engineering* 58.4, pages 1013–22.

Leizea, I., Mendizabal, A., Alvarez, H., Aguinaga, I., Sánchez, E., and Borro, D. (2015). “Tracking of deformable objects based on a visual approach and physics simulation for robot-assisted surgery”. In: *IEEE Computer Graphics and Applications*.

Lim, Y.-J., Deo, D., Singh, T., Jones, D., and De, S. (2009). “In situ measurement and modeling of biomechanical response of human cadaveric soft tissues for physics-based surgical simulation”. In: *Surgical endoscopy* 23.6, pages 1298–307.

Liu, A., Tendick, F., Cleary, K., and Kaufmann, C. (2003). “A Survey of Surgical Simulation: Applications, Technology, and Education”. In: *Presence: Teleoperators and Virtual Environments* 12.6, pages 599–614.

Liu, G. and Gu, Y. (2005). *An Introduction to Meshfree Methods and Their Programming.*

Liu, Z. and Bilston, L. (2000). “On the viscoelastic character of liver tissue: experiments and modelling of the linear behaviour”. In: *Biorheology* 37.3, pages 191–201.

Liu, Z. and Bilston, L. (2002). “Large deformation shear properties of liver tissue”. In: *Biorheology* 39.6, pages 735–42.

Lopez-Pamies, O. (2010). “A new I1-based hyperelastic model for rubber elastic materials”. In: *Comptes Rendus Mécanique* 338.1, pages 3–11.

Madsen, E., Hobson, M., Shi, H., Varghese, T., and Frank, G. (2005). “Tissue-mimicking agar/gelatin materials for use in heterogeneous elastography phantoms”. In: *Physics in medicine and biology* 50.23, pages 5597–618.

Maïsetti, O., Hug, F., Bouillard, K., and Nordez, A. (2012). “Characterization of passive elastic properties of the human medial gastrocnemius muscle belly using supersonic shear imaging”. In: *Journal of biomechanics* 45.6, pages 978–84.

Mariappan, Y., Glaser, K., and Ehman, R. (2010). “Magnetic resonance elastography: a review”. In: *Clinical anatomy (New York, N.Y.)* 23.5, pages 497–511.

Martins, P., Natal Jorge, R., and Ferreira, A. (2006). “A Comparative Study of Several Material Models for Prediction of Hyperelastic Properties:

Application to Silicone-Rubber and Soft Tissues". In: *Strain* 42.3, pages 135–147.

Meier, U., López, O., Monserrat, C., Juan, M., and Alcañiz, M. (2005). "Real-time deformable models for surgery simulation: a survey". In: *Computer methods and programs in biomedicine* 77.3, pages 183–97.

Mendizabal, A., Aguinaga, I., and Sánchez, E. (2015). "Characterisation and modelling of brain tissue for surgical simulation". In: *Journal of the Mechanical Behavior of Biomedical Materials* 45, pages 1–10.

Mendizabal, A., Landeira, M., Aguinaga, I., and Sánchez, E. (2012). "Soft Tissue Equivalent Phantom Materials: Experiments on Mechanical Properties of Agar/Gelatin/PPG Based Phantoms". In: *CASEIB Congreso Anual de la Sociedad Española de Ingeniería Biomédica.* 3, pages 3–6.

Mezger, T. (2006). *The Rheology Handbook.* Hannover, Germany: Vicentz Network GmbH & Co. KG.

Miga, M., Paulsen, K., Hoopes, P., Kennedy, F., Hartov, A., and Roberts, D. (2000). "In vivo quantification of a homogeneous brain deformation model for updating preoperative images during surgery". In: *IEEE transactions on biomedical engineering.* Volume 47. 2, pages 266–73.

Miller, K. and Chinzei, K. (1997). "Constitutive modelling of brain tissue: experiment and theory". In: *Journal of biomechanics* 30.11-12, pages 1115–1121.

Miller, K. and Chinzei, K. (2002). "Mechanical properties of brain tissue in tension". In: *Journal of biomechanics* 35.4, pages 483–90.

Miller, K., Chinzei, K., Orssengo, G., and Bednarz, P. (2000). “Mechanical properties of brain tissue in-vivo: experiment and computer simulation”. In: *Journal of biomechanics* 33.11, pages 1369–76.

Miller, K., Joldes, G., Lance, D., and Wittek, A. (2007). “Total Lagrangian explicit dynamics finite element algorithm for computing soft tissue deformation”. In: *Communications in Numerical Methods in Engineering* 23.August 2006, pages 121–134.

Miller, K., Wittek, A., and Joldes, G. (2010). “Biomechanics of the brain for computer-integrated surgery”. In: *Acta of Bioengineering and Biomechanics* 12.2.

Misra, S., Ramesh, K., and Okamura, A. M. (2008). “Modeling of tool-tissue interactions for computer-based surgical simulation: a literature review”. In: *Presence-:eleoperators and Virtual Environments* 17.5, pages 1–41.

Misra, S., Ramesh, K., and Okamura, A. M. (2010). “Modelling of non-linear elastic tissues for surgical simulation”. In: *Computer methods in biomechanics and biomedical engineering* 13.6, pages 811–8.

Monserrat, C., Meier, U., Alcan, M., Chinesta, F., and Juan, M. (2001). “A new approach for the real-time simulation of tissue deformations in surgery simulation”. In: *Computer Methods and Programs in Biomedicine* 64, pages 77–85.

Moreno Botella, R. (2005). *Reología de suspensiones cerámicas.* Edited by C. S. d. I. Científicas, page 328.

Muller, M., Gennisson, J.-L., Deffieux, T., Tanter, M., and Fink, M. (2009). “Quantitative viscoelasticity mapping of human liver using supersonic shear imaging: preliminary in vivo feasibility study”. In: *Ultrasound in medicine & biology* 35.2, pages 219–29.

Nasseri, S., Bilston, L., and Phan-Thien, N. (2002). “Viscoelastic properties of pig kidney in shear, experimental results and modelling”. In: *Rheologica Acta*, pages 180–192.

Nava, A, Mazza, E, Furrer, M, Villiger, P, and Reinhart, W. H. (2008). “In vivo mechanical characterization of human liver”. In: *Medical image analysis* 12.2, pages 203–16.

Nayar, V. T., Weiland, J. D., Nelson, C. S., and Hodge, a. M. (2012). “Elastic and viscoelastic characterization of agar”. In: *Journal of the mechanical behavior of biomedical materials* 7, pages 60–8.

Nealen, A., Müller, M., Keiser, R., Boxerman, E., and Carlson, M. (2005). “Physically Based Deformable Models in Computer Graphics”. In: *Eurographics*.

Nicolle, S., Lounis, M., Willinger, R., and Palierne, J.-F. (2005). “Shear linear behavior of brain tissue over a large frequency range”. In: *Biorheology* 42.3, pages 209–23.

Nunes, L. (2011). “Mechanical characterization of hyperelastic polydimethylsiloxane by simple shear test”. In: *Materials Science and Engineering: A* 528.3, pages 1799–1804.

Ohno, S., Kato, H., Harimoto, T., Ikemoto, Y., Yoshitomi, K., Kadohisa, S., Kuroda, M., and Kanazawa, S. (2008). “Production of a Human-Tissue-Equivalent MRI Phantom: Optimization of Material Heating”. In: *Magnetic Resonance in Medicine* 7(3), pages 131–140.

Oudry, J., Bastard, C., Miette, V., Willinger, R., and Sandrin, L. (2009). “Copolymer in oil phantom materials for Elastography”. In: *Ultrasound in Medicine and Biology* 35(7), pages 1185–1197.

Park, S. W. and Schapery, R. (1999). “Methods of interconversion between linear viscoelastic material functions. Part I - a numerical method based on Prony series”. In: *International Journal of Solids and Structures* 36, pages 1653–1675.

Peterlík, I., Duriez, C., and Cotin, S. (2012). “Modeling and real-time simulation of a vascularized liver tissue”. In: *international conference on Medical Image Computing and Computer-Assisted Intervention* 1, pages 50–57.

Picinbono, G., Delingette, H., and Ayache, N. (2003). “Non-linear anisotropic elasticity for real-time surgery simulation”. In: *Graphical Models* 65.5, pages 305–321.

Pioletti, D., Rakotomanana, L., Benvenuti, J., and Leyvraz, P. (1998). “Viscoelastic constitutive law in large deformations: application to human knee ligaments and tendons”. In: *Journal of biomechanics* 31.8, pages 753–7.

Prange, M. T. and Margulies, S. S. (2002). “Regional, Directional, and Age-Dependent Properties of the Brain Undergoing Large Deformation”. In: *Journal of Biomechanical Engineering* 124.2, page 244.

Prevost, T. P., Balakrishnan, A., Suresh, S., and Socrate, S. (2011). “Biomechanics of brain tissue”. In: *Acta biomaterialia* 7.1, pages 83–95.

Rashid, B., Destrade, M., and Gilchrist, M. (1991). “A High Rate Tension Device for Characterizing Brain Tissue”. In: pages 1–10.

Rashid, B., Destrade, M., and Gilchrist, M. D. (2013). “Influence of preservation temperature on the measured mechanical properties of brain tissue”. In: *Journal of biomechanics* 46.7, pages 1276–81.

Raul, J.-S., Deck, C., Willinger, R., and Ludes, B. (2008). “Finite-element models of the human head and their applications in forensic practice”. In: *International journal of legal medicine* 122.5, pages 359–66.

Roberts, J., Merkle, A., Biermann, P., Ward, E., Carkhuff, B., Cain, R., and O’Connor, J. (2007). “Computational and experimental models of the human torso for non-penetrating ballistic impact”. In: *Journal of biomechanics* 40.1, pages 125–36.

San Vicente, G. (2011). “Designing deformable models of soft tissue for virtual surgery planning and simulation using the Mass-Spring Model”. PhD thesis.

Sedef, M., Samur, E., and Basdogan, C. (2006). “Real-Time Finite Element Simulation of Linear Viscoelastic Tissue Behavior Based on Experimental Data”. In: *IEEE Computer Society*, pages 28–38.

Shafieian, M., Bao, J., and Darvish, K. (2011). “Mechanical Properties of Brain Tissue in Strain Rates of Blast Injury”. In: *Journal of Cerebral Blood Flow and Metabolism*, pages 4–5.

Shafieian, M., Laksari, K., Darvish, K., and Crandall, J. (2012). “Development of a Constitutive Model for Brain Tissue under Multiaxial Loading”. In: *IRCOBI Conference 2012*, pages 467–473.

Skrinjar, O., Nabavi, A., and Duncan, J. (2002). “Model-driven brain shift compensation”. In: *Medical image analysis* 6.4, pages 361–73.

Snedeker, J., Niederer, P., Schmidlin, F., Farshad, M., Demetropoulos, C., Lee, J., and Yang, K. (2005). “Strain-rate dependent material properties of the porcine and human kidney capsule”. In: *Journal of biomechanics* 38.5, pages 1011–21.

Sokhanvar, S., Dargahi, J., and Packirisamy, M. (2008). “Hyperelastic modelling and parametric study of soft tissue embedded lump for MIS applications”. In: August, pages 232–241.

Sturm, L. (2012). “Surgical simulation for training: Skills transfer to the operating room”. In: *Database of Abstracts of Reviews of Effects (DARE)* 61.

Székely, G., Brechbühler, C., Hutter, R., Rhomberg, A., Ironmonger, N., and Schmid, P. (2000). “Modelling of soft tissue deformation for laparoscopic surgery simulation”. In: *Medical image analysis* 4.1, pages 57–66.

Tanter, M., Touboul, D., Gennisson, J.-L., Bercoff, J., and Fink, M. (2009). “High-Resolution Quantitative Imaging of Cornea Elasticity Using Supersonic Shear Imaging”. In: *IEEE transactions on medical imaging* 28.12, pages 1881–1893.

Velardi, F., Fraternali, F., and Angelillo, M. (2006). “Anisotropic constitutive equations and experimental tensile behavior of brain tissue”. In: *Biomechanics and modeling in mechanobiology* 5.1, pages 53–61.

Venkatesh, S., Yin, M., Talwalkar, J., and Ehman, R. (2008). “Application of Liver MR Elastography in Clinical Practice”. In: *Proceedings of the International Society for Magnetic Resonance in Medicine.* Volume 16, page 2611.

Veronda, D. and Westmann, R. (1970). “Mechanical characterization of skin-finite deformations”. In: *Journal of biomechanics* 3.I 965.

Wang, P., Becker, A., Glover, A., Jones, I., Benford, S., Vloeberghs, M., and Greenglagh, C. (2005). “Designing a Virtual Reality Simulator for Neurosurgery”. In: *Proceedings of the Seventh International Conference on Virtual Reality*, pages 35–39.

Wang, P., Becker, A., Jones, I., Glover, A., Benford, S., Greenhalgh, C., and Vloeberghs, M. (2006). “A virtual reality surgery simulation of cutting and retraction in neurosurgery with force-feedback”. In: *Computer methods and programs in biomedicine* 84.1, pages 11–8.

Warfield, S., Talos, F., Tei, A., Bharatha, A., Nabavi, A., Ferrant, M., McL. Black, P., Jolesz, F., and Kikinis, R. (2001). “Real-time registration of volumetric brain MRI by biomechanical simulation of deformation during image guided neurosurgery”. In: *Computing and Visualization in Science* 5.1, pages 3–11.

Wittek, A., Hawkins, T., and Miller, K. (2009). “On the unimportance of constitutive models in computing brain deformation for image-guided surgery”. In: *Biomechanics and modeling in mechanobiology* 8.1, pages 77–84.

Wu, J., Dong, R., Smutz, W., and Schopper, A. (2003). “Nonlinear and viscoelastic characteristics of skin under compression: experiment and analysis”. In: *Bio-Medical Materials and Engineering* 13, pages 373–385.

Wuerfel, J., Paul, F., Beierbach, B., Hamhaber, U., Klatt, D., Papazoglou, S., Zipp, F., Martus, P., Braun, J., and Sack, I. (2010). “MR-elastography reveals degradation of tissue integrity in multiple sclerosis”. In: *NeuroImage* 49.3, pages 2520–5.

Yin, M., Talwalkar, J., Glaser, K., Manduca, A., Grimm, R., Rossman, P., Fidler, J., and Ehman, R. (2007). “Assessment of Hepatic Fibrosis With Magnetic Resonance Elastography”. In: *Clinical Gastroenterology and Hepatology* 5.10, pages 1207–1213.

Yoo, L., Gupta, V., Lee, C., Kavehpore, P., and Demer, J. L. (2011). “Viscoelastic properties of bovine orbital connective tissue and fat:

constitutive models." In: *Biomechanics and modeling in mechanobiology* 10.6, pages 901–14.

Yoshizawa, A., Okamoto, J., Yamakawa, H., and Fujie, M. G. (2005). "Robot Surgery based on the Physical Properties of the Brain -Physical Brain Model for Planning and Navigation of a Surgical Robot-". In: *International Conference on Robotics and Automation*. April, pages 904–911.

Zhong, H., Wachowiak, M. P., and Peters, T. M. (2005). "A real time finite element based tissue simulation method incorporating nonlinear elastic behavior". In: *Computer Methods in Biomechanics and Biomedical Engineering* 8.3, pages 177–189.

Zhu, B. and Gu, L. (2012). "A hybrid deformable model for real-time surgical simulation". In: *Computerized medical imaging and graphics : the official journal of the Computerized Medical Imaging Society* 36.5, pages 356–65.

Zhu, B., Gu, L., and Zhou, Z. (2010). "Particle-Based Deformable Modeling with Pre-computed Surface Data in Real-Time Surgical Simulation". In: *Medical imaging and augmented reality*, pages 503–512.

Zhurov, A., Limbert, G., Aeschlimann, D., and Middleton, J. (2007). "A constitutive model for the periodontal ligament as a compressible transversely isotropic visco-hyperelastic tissue". In: *Computer methods in biomechanics and biomedical engineering* 10.3, pages 223–35.